Georgia Institute of Technology
Atlanta, Georgia 30332

ACTIVELY CONTROLLED SHAFT SEALS FOR AEROSPACE APPLICATIONS

Summary of Research (Final Report)

January 1, 1989 - December 31, 1994

NASA Research Grant NAG 3-974

Principal Investigator Richard F. Salant
College of Engineering
School of Mechanical Engineering

NASA Technical Officer: M.P. Proctor
NASA Lewis Research Center, MS SPT D-2
Space Vehicle Propulsion Branch

E25-666

TABLE OF CONTENTS

LIST OF FIGURES

LIST OF SYMBOLS

General Notation

A_{face}	area of seal face
c	elasticity coefficient (N/m^2)
e	piezoelectric coefficient (stress/electric field)
e(t)	error term for P.I.D. controller
E	elastic modulus
F_{close}	closing force
F^*_{close}	nondimensional closing force
F_{open}	opening force
F^*_{open}	nondimensional opening force
F_{spring}	spring force
G	gravitational acceleration
H	convective heat transfer coefficient
h	film thickness
k	thermal conductivity
K	seal stiffness
K*	nondimensional seal stiffness
K_P	proportional constant for P.I.D. controller
K_I	integral constant for P.I.D. controller

K_D	derivative constant for P.I.D. controller
$\dot{m}$	mass flow rate
N_b	balance ratio
O(t)	output signal from P.I.D. controller
P	pressure
P^*	nondimensional pressure
q	heat generation rate per unit area
Q	heat generation rate
Q^*	nondimensional heat generation rate
r	radial coordinate
r_b	balance radius
r^*	nondimensional radial coordinate
R	gas constant
T	temperature
t	time
v	velocity
z	axial coordinate

Greek Letters

α	coefficient of thermal expansion
β	slope of seal face

δ	coning
δ^*	nondimensional coning
ε	dielectric coefficient
θ	circumferential coordinate
κ	relaxation factor
μ	viscosity
ρ	density
τ	stress
ω	rotational speed

Subscripts

i	value at inner radius of seal interface
o	value at outer radius of seal interface
r	radial direction
z	axial direction
θ	circumferential direction

Superscripts

*	nondimensional number
r	real number
i	imaginary number

SUMMARY

This study experimentally investigates an actively controlled mechanical seal for aerospace applications. The seal of interest is a gas seal, which is considerably more compact than previous actively controlled mechanical seals that were developed for industrial use.

In a mechanical seal, the radial convergence of the seal interface has a primary effect on the film thickness. Active control of the film thickness is established by controlling the radial convergence of the seal interface with a piezoelectric actuator.

An actively controlled mechanical seal was initially designed and evaluated using a mathematical model. Based on these results, a seal was fabricated and tested under laboratory conditions. The seal was tested with both helium and air, at rotational speeds up to 3770 rad/sec, and at sealed pressures as high as 1.48×10^6 Pa. The seal was operated with both manual control and with a closed-loop control system that used either the leakage rate or face temperature as the feedback. The output of the controller was the voltage applied to the piezoelectric actuator.

The seal operated successfully for both short term tests (less than one hour) and for longer term tests (four hours) with a closed-loop control system. The leakage rates were typically 5-15 slm (standard liters per minute), and the face temperatures were generally maintained below 100 °C. When leakage rate was used as the feedback signal, the setpoint leakage rate was typically maintained within 1 slm. However, larger deviations occurred during sudden changes in sealed pressure. When face temperature was used as the feedback signal, the setpoint face temperature was generally maintained within 3 °C, with larger deviations occurring when the sealed pressure changed suddenly.

The experimental results were compared to the predictions from the mathematical model. The model was successful in predicting the trends in leakage rate that occurred as the balance ratio and sealed pressure changed, although the leakage rates were not quantitatively predicted with a high degree of accuracy. This model could be useful in providing valuable design information for future actively controlled mechanical seals.

PUBLICATIONS GENERATED UNDER GRANT

Salant, R. F., Wolff, P. and Navon, S., "Electronically controlled mechanical seal for aerospace applications - part I: design, analysis, and steady state tests," Tribology Transactions, vol. 37, pp. 189-195, 1994.

Salant, R. F. and Wolff, P. J., "Development of an Electronically Controlled Mechanical Seal for Aerospace Applications," SAE Transactions, 941207, 1994. Edited versions of this paper appeared in Aerospace Engineering, vol. 14, no. 7, pp. 7-10, 1994, and in Sealing Technology, vol. 1, no. 12, pp. 5-7, 1994.

Wolff, P. J. and Salant, R. F., "Electronically controlled mechanical seal for aerospace applications - part II: transient tests,"Tribology Transactions, vol. 38, pp. 51-56, 1995.

Salant, R. F., Wolff, P. and Navon, S., "Maintaining full film lubrication in mechanical seals by means of electronic control," Tribologia, Finnish Journal of Tribology, vol. 11, no.2, pp.122-129, 1992.

Wolff, P. and Salant, R. F., "Design and analysis of a controllable mechanical seal for aerospace applications," Proc. 4th International Symposium on Transport Phenomena and Dynamics of Rotating Machinery, vol. A, pp. 286-295, Pacific Center of Thermal- Fluid Engineering, 1992.

CHAPTER I

INTRODUCTION

Mechanical seals are commonly used in turbomachinery where rotating shaft seals are required. Figure 1-1 presents a typical mechanical seal. These seals generally consist of a rotating element (also called the rotor), a nonrotating element (also called the stator), a spring, and secondary seals. One of the elements, known as the floating element, is mounted on springs and dynamically tracks the face of the other element. In Figure 1-1, the floating element is the stator.

The operation of a mechanical seal can be understood by examining Figure 1-1. There are two leakage paths from the higher pressure region (P_o) at the outside radius of the stator to the lower pressure region (P_i) at the inside radius of the stator; the gap between the housing and the stator, and the gap between the stator and the rotor. Leakage through the first path is prevented by the secondary seal. The second leakage path is restricted by the spring and pressure forces that act on the stator to push it against the rotor. Well-designed mechanical seals leak significantly less than most other types of seals.

Mechanical seals are generally classified as either contacting or noncontacting. In a contacting seal the faces touch, resulting in high surface temperatures, high contact stresses, and high wear rates. This is in contrast to noncontacting mechanical seals, which operate with a thin lubricating film between the seal faces. This film prevents wear and ensures a longer seal life. For applications where reliability is a principal concern, noncontacting seals are preferred.

Noncontacting mechanical seals are further classified as either hydrostatic or hydrodynamic. In a hydrostatic mechanical seal, the film thickness and pressure distribution within the lubricating film are independent of the rotational speed of the rotor. This type of operation occurs for seals whose faces are flat and axisymmetric. The operation of a hydrodynamic seal, on the other hand, depends on the rotational speed of the shaft. These seals typically have non-axisymmetric geometries, such as spiral grooves or steps, machined or etched into one of the seal faces. Elevated pressures are generated within the lubricating film due to the rotation of the seal rotor.

The seal of interest in the present study is a hydrostatic mechanical seal. The film thickness in such a seal is strongly dependent on the radial convergence of the seal faces. This radial convergence is known as coning and is shown in Figure 1-1. The coning is considered positive when the faces of the seal converge in the radial direction from high to low pressure. For a seal with positive coning (required for stable seal operation), the film thickness between the seal faces increases as the coning increases.

The thickness of the lubricating film is determined by the closing and opening forces that act on the floating component of the seal. These forces are presented in Figure 1-2. The closing force pushes the faces of the stator and rotor together, and is produced by the sealed pressure acting on the backside of the floating component and by the spring force. The opening force pushes the faces of the seal apart and is produced by the pressure distribution within the thin film between the seal faces. The opening force increases as the coning, normalized with respect to the film thickness, increases. The floating component will assume an axial location such that the closing and opening forces balance. A well-designed seal operates such that these forces balance with a film thickness on the order of a few microns (3-5 μm). However, under transient and off-design conditions, this film thickness may change, resulting in either too large or too small a film thickness. If the film

becomes too large, excessive leakage will result. Conversely, if the film becomes too small, mechanical contact of the seal faces could occur, resulting in excessive wear.

The coning in a mechanical seal is typically a result of mechanical and thermal deformations. A recent approach however, employed in industrial seals, utilizes a piezoelectric material to actively control the coning [Salant et. al., 1987; Salant et. al., 1989]. Figure 1-3 presents a sketch of such an actively controlled seal. This configuration includes a piezoelectric actuator, thermocouples embedded in a face of the seal, and a microcomputer based control system. In this seal configuration the floating component is the rotor.

The above seal is configured such that when voltage is applied to the piezoelectric actuator, the latter expands axially and produces positive coning of the nonrotating face. At off-design conditions, when face contact may be imminent, voltage is applied to the actuator, which increases the coning, and prevents face contact. Conversely, when the leakage becomes too large, the applied voltage is decreased, which reduces the leakage of the seal.

The goal of the present project is to demonstrate the feasibility of utilizing an actively controlled mechanical seal in a liquid oxygen turbopump (see Figure 4-1) for an aerospace vehicle. Currently, floating ring seals are utilized for the helium buffer seal in the liquid oxygen turbopump (see Figure 4-2). The floating ring seals prevent contact between the hot gases that drive the turbine, and the liquid oxygen. These seals typically operate with a clearance on the order of 20 μm, which is 4-5 times larger than a representative film thickness in a conventional mechanical seal. The leakage in a seal is proportional to the clearance cubed; therefore a reduction in clearance by a factor of 5 reduces the leakage by a factor of 125. This reduction in leakage (and reduction in stored helium) represents considerable savings for an aerospace mission in which payload is a

principal concern. Therefore, it is desired to replace the floating ring seals with mechanical seals.

Although conventional mechanical seals operate with much lower leakage rates than floating ring seals, they are generally not as reliable. Mechanical seals could inadvertently operate in a contacting mode, resulting in face damage and high face temperatures, the latter increasing the risk of explosion. Conversely, if the film thickness becomes excessive, large leakage rates result, which could deplete the supply of the helium purge gas. A controllable mechanical seal could considerably enhance the seal's reliability, making a mechanical seal suitable for applications where reliability is a principal concern.

This thesis presents the design and experimental investigation of an actively controlled mechanical seal. Earlier analytical work [Wolff, 1991] suggested that such a seal, operating in a gaseous environment, is feasible.

As part of the present study, this seal was fabricated and tested under various conditions in a laboratory test rig. This seal includes a piezoelectric actuator, through which the coning of the seal faces is controlled by varying the voltage applied to the actuator. The seal was tested in both helium and air, at sealed pressures between 4.46 x 10^5 and 1.48x10^6 Pa (50 and 200 psig), and at rotational speeds as high as 3770 rad/sec (36,000 rpm). The various tests performed with the seal included steady state operation with manual control, and transient operation with a closed-loop control system.

The steady state tests involved applying a large initial voltage to the actuator, and operating the seal at a fixed voltage for a set amount of time. The voltage was then decreased in 500 V steps until a minimum voltage level was reached and then increased in 500 V steps until the initial voltage was again reached. The voltage was maintained at each voltage increment for the same set time. These tests clearly indicated that the film

thickness in the seal could be controlled over a considerable range, and excessive face temperatures prevented.

The next phase of the seal testing involved imposing various transient operating conditions on the seal while operating the seal with a closed-loop control system. The transients imposed on the seal included a ramp decrease followed by a ramp increase in pressure, and a step decreased followed by a step increase in pressure. The rotational speed was also varied in the same manner. Tests were performed in which either the flow rate or the face temperature were used as feedback to the controller. The output of the control system was the voltage applied to the piezoelectric actuator. The control algorithm was a commercially available P.I.D. (proportional, integral, differential) controller. Results from the transient tests indicated that the controller could maintain the feedback signal within reasonable limits while transient operating conditions were imposed on the seal.

The next sequence of transient tests involved operating the seal for an extended period of time (typically four hours). The extended test was divided into one-half hour cycles. Each cycle consisted of a startup and shutdown, a step decrease and step increase in pressure and speed, and a rapid variation of the sealed pressure and rotational speed. During these tests, the feedback for the controller was the leakage rate of the seal. The seal maintained the setpoint well during these tests. Very little wear occurred during these tests, as indicated by performing surface evaluations of the seal faces prior to, and after the seal tests.

The results of these tests demonstrate that the actively controlled mechanical seal for aerospace applications is feasible. The next phase of the development would involve modifying the design to accommodate the more severe operating conditions that are present in a liquid oxygen turbopump.

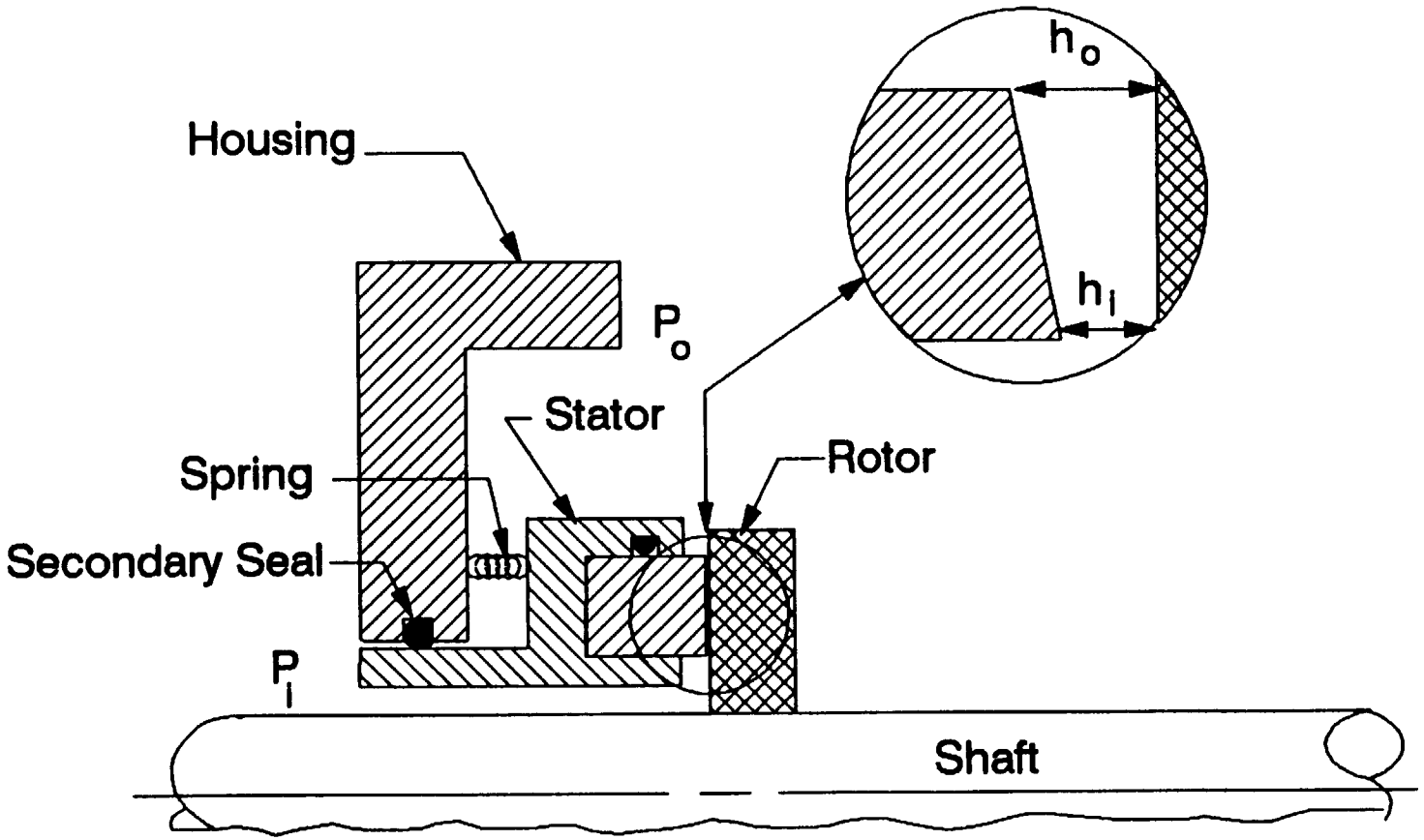

Figure 1-1. Schematic of a Mechanical Seal

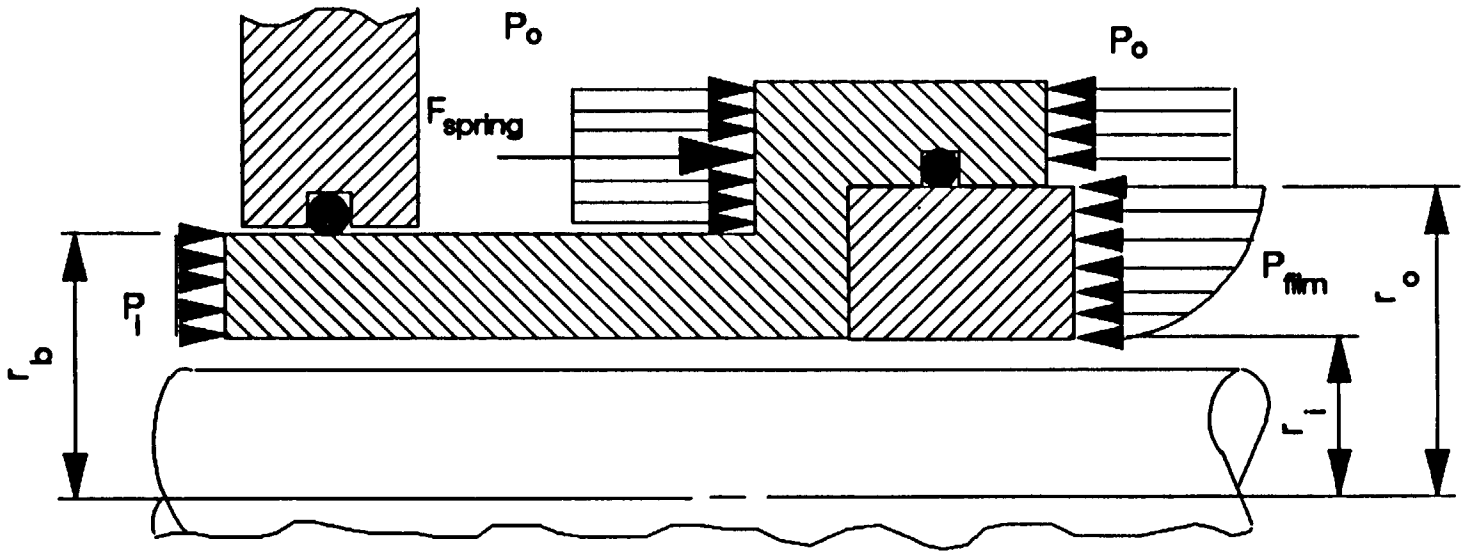

Figure 1-2. Forces Acting on Floating Element

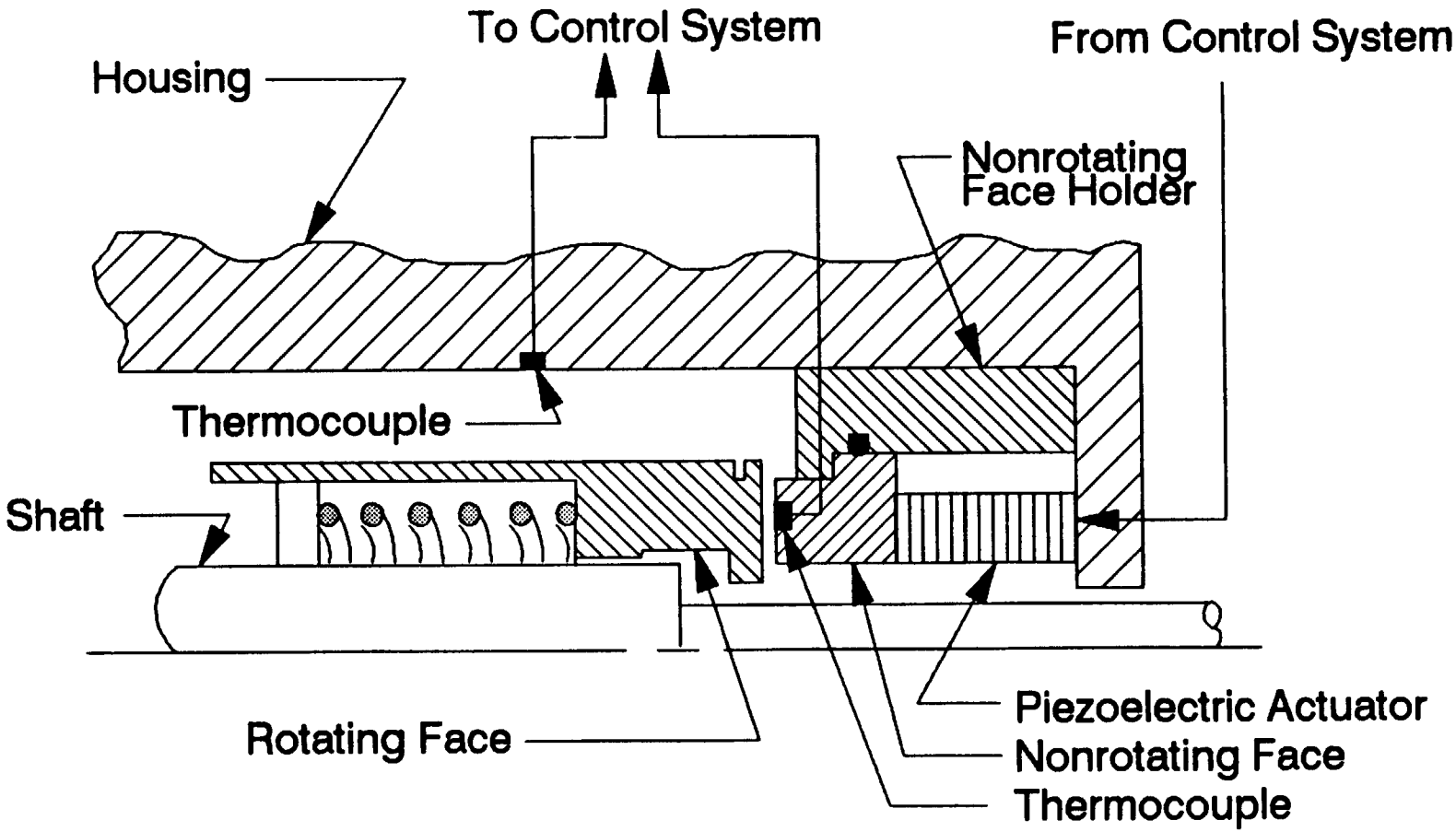

Figure 1-3. Actively Controlled Seal for Industrial Use

CHAPTER II

LITERATURE REVIEW

Mechanical Seals

The mathematical model of a mechanical seal presented in this thesis is based on the assumptions that there is a thin fluid film between the seal faces and that the load support is primarily due to the hydrostatic pressure distribution. These assumptions however, are not immediately obvious. For many years it was believed that all seals operated in a contacting mode [Mayer, 1977] and the load was carried by the mechanical contact between the seal faces. In recent years however, extensive research has verified that a thin fluid film exists between the faces of a noncontacting seal, which is solely responsible for the load support.

Existence of Fluid Film

The assumption that a thin fluid film exists between the faces of a mechanical seal has been long suspected [Nau, 1967] and recently directly validated through an experiment. Doust and Parmar [1985] successfully measured fluid film profiles between the faces of a mechanical seal to determine the effects of pressure and thermal loads on the deformation of the seal faces. In their investigation, they instrumented a mechanical seal with capacitance probes to measure film thickness. These experiments were performed for sealed pressures between 0 and 4 MPa, for various face temperatures, and for shaft speeds up to 3000 rpm. This study clearly indicated that a fluid film existed for the operating conditions examined.

Salant and Key [1984] also verified that a fluid film exists by examining the torque variations of a seal as a function of speed and load, and by measuring the wear rate of a

carbon-graphite seal face. They then compared these results with known characteristics of continuous film and boundary lubrication regimes, thereby verifying the existence of a continuous film.

Load Support

Another assumption of the present study is that for a seal with flat axisymmetric faces, the opening force is produced only by the hydrostatic pressure distribution. This assumption was verified by Salant and Key [1984], who compared the forces generated by the hydrostatic pressure distribution to the forces generated from hydrodynamic effects. The conditions inducing the hydrodynamic effects included roughness, waviness, misalignment, and eccentricity of the seal faces. They computed the opening forces from the hydrodynamic effects based on equations which were developed by previous researchers. These results showed that for axisymmetric, noncontacting face seals, the hydrodynamic effects can be ignored relative to the opening force generated by the hydrostatic pressure distribution.

Previous Seal Models

Mathematical models have been created in recent years which give meaningful predictions of the performance of mechanical seals. This is a significant achievement considering that the film thickness is on the order of microns and deformations on the order of microns affect the performance of the seal. Useful models must therefore predict these extremely small deformations. The mathematical models which concern this project most directly are those created by Metcalfe [1971, 1979, 1981], and Salant and Key [1984].

The model utilized for the analysis of the actively controlled seal is essentially based on the research of Metcalfe. Metcalfe [1971] utilized a hydrostatic model to predict pressure distributions, leakage rates, and viscous heat generation within the fluid film of a

mechanical seal. This model demonstrated that the hydrostatic pressure distribution is strongly dependent on the profile of the fluid film. He then utilized finite element techniques to compute the deformations of the seal faces from which the film profile could be determined [Metcalfe, 1979]. The deformations were produced by pressure loads, and by loads due to the interfacial friction between the two component assemblies. A series of experiments were then performed on various seal assemblies to validate these models [Metcalfe, 1981]. Leakage rates were measured, from which the deformations of the seal faces were computed. These experimentally determined deformations correlated well with those obtained from the analytical models.

The results of Metcalfe were extended and further validated by Salant and Key [1984], who included the effects of thermal deformations. Several seals were tested, and their performance was compared to the results predicted by the analytical model. It was found that the analytical model predictions correlated well with the observed behavior of the seals.

A comprehensive text written by Lebeck [1991] discusses several aspects of mechanical seals. Included is a thorough discussion of the fluid mechanics of the interfacial film, the thermal effects, and solid mechanics. Several mathematical models of varying complexity are also presented. These models differ from the aforementioned ones in that ring mechanics are used to model the seal face deformations whereas finite element techniques were used in the previously mentioned seal models. An additional difference is that the models developed by Lebeck can accommodate contacting faces whereas the aforementioned models assume that a film continuously separates the seal faces.

Actively Controlled Seals

The film thickness in a mechanical seal is determined by the opening and closing forces that act on the floating component of the seal. Previous researchers have examined various strategies to control the forces that act on the seal, and thereby control the film thickness.

As previously discussed (see Chapter I - Introduction), the opening force is strongly dependent on the coning of the seal faces. Salant et. al. [1987] investigated a controllable seal that controlled the opening force of the seal by adjusting the coning of the seal faces. The coning in this seal was produced by a stack of piezoelectric elements, which were located near the inner radius of the nonrotating seal face. A voltage applied to the piezoelectric elements caused them to expand in the axial direction and push the inside radius of the seal face in the axial direction. Since the outer radius of the seal face was restrained, a coning deformation was thereby produced, which increased as the voltage was increased. In addition to the piezoelectric elements, the control components for this seal consisted of a thermocouple embedded in the nonrotating seal face, a thermocouple in the seal cavity to monitor the temperature of the sealed fluid, a voltage supply, and a microprocessor-based control system.

The control strategy for the above seal was based on establishing a reference point where face contact occurred. A slight increase in voltage then prevented face contact while the film thickness was minimized. The reference point where contact occurred was identified in one of two ways, by either measuring a large temperature difference between the seal face and seal chamber, or by detecting oscillations in the seal face temperature. Large temperature differences would occur for face contact due to the heat generation produced by friction between the seal faces. Temperature oscillations were also an indication of zero film thickness because thermoelastic instabilities have been found to

occur when seal faces contact. Once a minimum film thickness was found, the voltage was held constant until the temperature difference between the seal face and the seal chamber changed by more than some preset limits. If this occurred, the control system once again searched for an optimum film thickness.

Heilala and Kangasniemi [1987] also designed a seal with a controllable opening force. This was achieved with a control system which consisted of a compressed air supply and supply line to the seal film, a thermocouple embedded in the face of the nonrotating component, a pneumatic valve, and a controller. The input to the control system was the temperature of the seal face, measured by the thermocouple, which gave an indication of the film thickness. As the face temperature increased, the controller opened the pneumatic valve which increased the amount of compressed air fed into the seal film. The compressed air increased the pressure within the seal film, and thereby increased the opening force, which increased the film thickness. Results from this experiment demonstrated that lower face temperatures were achieved for the controllable seal as compared to an uncontrolled seal.

Etsion [1990] investigated a controllable hydrodynamic seal which was based on a variable closing force. The control system was similar to the control system utilized by Heilala and Kangasniemi; however, the compressed air was supplied to the backside of the floating component. The input for this control system was also the face temperature of seal, which was read by a microcomputer. Based on the face temperature, a back pressure was computed by the microcontroller, and the electro-pneumatic valve was then adjusted by the microcontroller to produce the desired back pressure.

Etsion investigated the response of this seal to changes in the speed of the test rig. Both a linear and nonlinear control algorithm were utilized to compute the back pressure as a function of the face temperature of the seal. Both control algorithms enabled the

control system to track the set point temperature reasonably well, however the nonlinear control algorithm demonstrated a faster response time.

CHAPTER III

MATHEMATICAL MODEL

In a previous study, a mathematical model was developed and used to evaluate a variety of seal designs [Wolff, 1991]. For the current study, this model was modified and compared to the experimental results. The mathematical model consists of four key components, a force balance, a fluid mechanics model, a finite element structural and thermal model, and an iterative computational algorithm. The primary performance parameter that this model provides is the leakage rate of the seal as a function of the applied voltage.

Force Balance

It is first necessary to perform a force balance on the floating component of a mechanical seal to compute the film thickness and leakage rate under steady state conditions. Figure 1-2 presents the floating component of a mechanical seal and the opening and closing forces that act upon it. The opening force tends to push the faces apart and is produced by the pressure forces in the gas film that act on the seal face. The closing force tends to push the faces of the seal together, and is produced by the pressure of the sealed fluid acting on the back side of the floating component, by the lower pressure at the inside radius of the seal acting on the floating component, and by the spring force. The closing force is given by

$$F_{close} = A_{face} N_b ((P_o - P_i) + P_i) + F_{spring} \tag{1}$$

and the opening force is computed from

$$F_{open} = \int_{Aface} P dA \tag{2}$$

The balance ratio is defined by

$$N_b = \frac{(r_o^2 - r_b^2)}{(r_o^2 - r_i^2)} \tag{3}$$

The balance ratio represents a ratio of two areas: the area of the back side of the floating component over which the pressure that tends to close the seal acts, to the area on the front side of the floating component over which the film pressure that tends to open the seal acts.

The closing force depends on the balance ratio, the fluid pressures at the inside and outside of the seal, and the spring force. Once these quantities are specified, it is straightforward to compute the closing force, which then remains constant for steady state conditions. However, to compute the opening force, it is necessary to determine the pressure distribution within the gas film, which requires solution of the governing fluid mechanics equations.

Fluid Mechanics Model of the Gas Film

The pressure within the gas film generates the opening force and also causes deformations of the seal faces, which affect the coning. Therefore, it is essential to compute the pressure distribution to predict the performance of a mechanical seal. The pressure distribution is governed by the Navier-Stokes Equations, which are given below in cylindrical coordinates for the r and θ directions:

$$\rho\left(\frac{\partial v_r}{\partial t}+v_r\frac{\partial v_r}{\partial r}+\frac{v_\theta}{r}\frac{\partial v_r}{\partial \theta}-\frac{v_\theta^2}{r}+v_z\frac{\partial v_r}{\partial z}\right)=\mu\left(\frac{\partial}{\partial r}\left(\frac{1}{r}\frac{\partial (rv_r)}{\partial r}\right)+\frac{1}{r^2}\frac{\partial^2 v_r}{\partial \theta^2}+\frac{\partial^2 v_r}{\partial z^2}-\frac{2}{r^2}\frac{\partial v_\theta}{\partial \theta}\right)-\frac{\partial P}{\partial r}+\rho G_r \tag{4}$$

$$\rho\left(\frac{\partial v_\theta}{\partial t}+v_r\frac{\partial v_\theta}{\partial r}+\frac{v_\theta}{r}\frac{\partial v_\theta}{\partial \theta}+v_r\frac{v_\theta}{r}+v_z\frac{\partial v_\theta}{\partial z}\right)=\mu\left(\frac{\partial}{\partial r}\left(\frac{1}{r}\frac{\partial (rv_\theta)}{\partial r}\right)+\frac{1}{r^2}\frac{\partial^2 v_\theta}{\partial \theta^2}+\frac{\partial^2 v_\theta}{\partial z^2}+\frac{2}{r^2}\frac{\partial v_r}{\partial \theta}\right)-\frac{1}{r}\frac{\partial P}{\partial \theta}+\rho G_\theta \tag{5}$$

An analytic expression for the pressure distribution can be obtained from these equations when the following assumptions are made [Hughes et. al., 1989, Wolff, 1991]

1. The flow is at steady state.
2. The seal faces are axisymmetric.
3. Squeeze effects are neglected.
4. Velocity gradients in the radial direction are much smaller than velocity gradients in the axial direction.
5. Centrifugal effects can be neglected.
6. Body forces are negligible compared to viscous forces and pressure forces.

7. The flow is laminar.
8. The flow is isothermal.
9. The gas film behaves as an ideal gas.

Based on these assumptions, the simplified Navier-Stokes Equations are

$$\mu \frac{\partial^2 v_r}{\partial z^2} = \frac{\partial P}{\partial r} \tag{6}$$

$$\frac{\partial^2 v_\theta}{\partial z^2} = 0 \tag{7}$$

with the boundary conditions

$$v_r = 0 \text{ at } z = 0 \text{ and } z = h \tag{8}$$

$$v_\theta = 0 \text{ at } z = 0 \tag{9}$$

$$v_\theta = \omega r \text{ at } z = h \tag{10}$$

When these equations are solved the following velocity distributions result:

$$v_r = \left(\frac{1}{2\mu}\right)\frac{dP}{dr}(z^2 - hz) \tag{11}$$

$$v_\theta = \left(\frac{w\, r\, z}{h}\right) \tag{12}$$

The mass flow rate, or leakage of the seal, may be obtained by integrating v_r over the film thickness in the axial direction:

$$\dot{m} = 2\pi\rho r \int_0^h v_r dz \tag{13}$$

Substituting Equation 11 into Equation 13, and integrating results in

$$\frac{dP}{dr} = \frac{-6\dot{m}\mu}{\pi\rho r h^3} \tag{14}$$

Assuming a linear profile for h

$$h = h_i + \beta(r - r_i) \tag{15}$$

and ideal gas behavior, results in the differential equation:

$$PdP = \frac{-6\dot{m}\mu RTdr}{\pi r(h_i + \beta(r - r_i))^3} \tag{16}$$

Integrating the left hand side of Equation 16 from the inside to the outside pressure, and integrating the right hand side from the inside to the outside radius leads to the following equation for the mass flow rate:

$$\dot{m} = [-\pi(P_o^2 - P_i^2)(h_o - \beta r_o)^3] / 12RT[\ln(\frac{r_o}{r_i}) - \ln(\frac{h_o}{h_i}) + (h_o - \beta r_o)(\frac{1}{h_o} - \frac{1}{h_i}) + \frac{(h_o - \beta r_o)^2}{2}(\frac{1}{h_o^2} \frac{1}{h_i^2})] \quad (17)$$

The pressure at any location within the gas film can now be found by substituting Equation 17 into Equation 16 and integrating the left hand side of Equation 16 from the pressure at the inside to the pressure at the desired radial location, and integrating the right hand side from the inside radius to the radius of the desired location:

$$\int_{P_i}^{P(r)} PdP = \int_{r_i}^{r} \frac{-6\dot{m}\mu RTdr}{\pi r(h_i + \beta(r - r_i))^3} \quad (18)$$

When this integration is performed, the following equation for the pressure results:

$$P = \{P_i^2 + (P_o^2 - P_i^2)[\ln(\frac{r}{r_i}) - \ln(\frac{h}{h_i}) + (h_o - \beta r_o)(\frac{1}{h} - \frac{1}{h_i}) + \frac{(h_o - \beta r_o)^2}{2}(\frac{1}{h^2} - \frac{1}{h_i^2})] / [\ln(\frac{r_o}{r_i}) - \ln(\frac{h_o}{h_i}) + (h_o - \beta r_o)(\frac{1}{h_o} - \frac{1}{h_i}) + \frac{(h_o - \beta r_o)^2}{2}(\frac{1}{h_o^2} - \frac{1}{h_i^2})]\}^{\frac{1}{2}} \quad (19)$$

This equation can be nondimensionalized in the following form:

$$P^* = \{P_i^{*2} + (1 - P_i^{*2})[\ln(r^*) - \ln(1 + \frac{\delta^*(r^* - 1)}{(r_o^* - 1)}) + (1 - \frac{\delta^*}{(r_o^* - 1)})$$
$$(\frac{(r_o^* - 1)}{(r_o^* - 1) + \delta^*(r^* - 1)} - 1) + \frac{1}{2}(1 - \frac{\delta^*}{(r_o^* - 1)})^2(\frac{(r_o^* - 1)^2}{[(r_o^* - 1) + \delta^*(r^* - 1)]^2} - 1)]/$$
$$[\ln(r_o^*) - \ln(1 + \delta^*) + (1 - \frac{\delta^*}{(r_o^* - 1)})(\frac{1}{1 + \delta^*} - 1) + \frac{1}{2}(1 - \frac{\delta^*}{(r_o^* - 1)})^2(\frac{1}{(1 + \delta^*)^2} - 1)]]^{\frac{1}{2}} \quad (20)$$

where

$$r^* = \frac{r}{r_i} \quad and \; r_o^* = \frac{r_o}{r_i} \quad (21)$$

$$P^* = \frac{P}{P_o} \quad and \; P_i^* = \frac{P_i}{P_o} \quad (22)$$

$$\delta^* = \frac{\delta}{h_i} \quad (23)$$

$$\delta = h_o - h_i \quad (24)$$

Figure 3-1 presents a graph of the nondimensional pressure distributions computed from Equation 20 for various values of δ^*, and for $r_o^* = 1.450$ (the value used for the steady state air tests). This figure and Equation 20 show that the nondimensional pressure distribution is uniquely determined by δ^*, r_o^*, and P_i^*.

Opening and Closing Forces

Once the pressure distribution has been computed from the fluid mechanics model, the opening force can be computed from Equation 2. Substituting Equations 21 and 22 into this equation results in

$$F_{open} = 2\pi P_o r_i^2 \int_1^{r_o^*} P^* r^* dr^* \tag{25}$$

Now define the nondimensional opening force with the following equation:

$$F_{open}^* = \frac{F_{open}}{P_o \pi (r_o^2 - r_i^2)} \tag{26}$$

Substituting Equation 26 into 25 results in the following equation for the nondimensional force:

$$F_{open}^* = \frac{2}{(r_o^{*2} - 1)} \int_1^{r_o^*} P^* r^* dr^* \tag{27}$$

The nondimensional opening force is uniquely determined by the three parameters δ^*, r_o^*, and P_i^*.

Neglecting the spring force and the force produced by the low pressure at the inside radius of the seal, the closing force is equal to

$$F_{close} = P_o \pi (r_o^2 - r_b^2) \tag{28}$$

Defining a nondimensional closing force, similar to the definition of a nondimensional opening force, and using Equation 28,

$$F^*_{close} = \frac{P_o \pi (r_o^2 - r_b^2)}{P_o \pi (r_o^2 - r_i^2)} = \frac{(r_o^2 - r_b^2)}{(r_o^2 - r_i^2)} \tag{29}$$

Therefore, this nondimensional closing force is equal to the balance ratio.

Seal Stiffness

The seal stiffness is an important parameter in determining the stability of the seal. The stiffness of the seal must be positive for the seal to be stable. This quantity is defined by

$$K = -\frac{dF_{open}}{dh_i} \tag{30}$$

This equation can be nondimensionalized by substituting Equations 26 and 23 into Equation 30, which results in

$$K = \frac{P_o \pi (r_o^2 - r_i^2) \delta^{*2}}{\delta} \frac{dF^*_{open}}{d\delta^*} \tag{31}$$

Now let the nondimensional stiffness be defined by

$$K^* = \frac{\delta}{P_o r_i^2} K \text{ such that } K^* = \pi (r_o^{*2} - 1) \delta^{*2} \frac{dF^*_{open}}{d\delta^*} \tag{32}$$

The nondimensional stiffness is thus uniquely determined by three parameters, P_i^*, r_o^*, and δ^*.

Seal Controllability

An additional requirement for a controllable seal is that the thickness of the gas film should be responsive to changes in voltage applied to the seal. The controllability of the seal can be defined as the rate of change of film thickness with respect to voltage:

$$\frac{dh_i}{dV} = \frac{dh_i}{d\delta}\frac{d\delta}{dV} \tag{33}$$

The film thickness can be determined from Equation 23 as a function of δ and δ^*. Once the closing force is specified, δ^* is a constant (assuming equilibrium), which leads to

$$\frac{dh_i}{d\delta} = \frac{d(\frac{\delta}{\delta^*})}{d\delta} = \frac{1}{\delta^*} \tag{34}$$

Substituting Equation 34 into 33

$$\frac{dh_i}{dV} = \frac{1}{\delta^*}\frac{d\delta}{dV} \tag{35}$$

The change in film thickness versus the change in voltage consists of two parts: $d\delta/dV$, which is a function of the piezoelectric material and the configuration of the deformable face assembly, and the nondimensional parameter $1/\delta^*$. To maximize the change in film

thickness of the seal versus the change in voltage, the change in coning versus the change in voltage must be maximized and δ^* must be minimized.

Viscous Heat Generation

For computation of the thermal deformations of the seal, it is necessary to determine the viscous heat generation rate that occurs within the gas film. The heat generation rate per unit face area within the gas film is given by

$$q = \tau_{r\theta} v_\theta = \mu \frac{dv_\theta}{dz} v_\theta \tag{36}$$

Since the radial velocity of the gas is much smaller than the angular velocity, it is neglected. Substituting Equation 12 into Equation 36, and solving for the viscous heat generation rate per unit face area at the rotating face (z=h), leads to

$$q = \frac{\mu \omega^2 r^2}{h} \tag{37}$$

Based on a linear profile for h, the rate at which heat is generated over the seal faces can be determined by integrating Equation 37:

$$Q = 2\pi\mu\omega^2 \int_{r_i}^{r_o} \frac{r^3}{h_i + \beta(r - r_i)} dr \tag{38}$$

Substituting Equations 21 and 23 into Equation 38, results in the following nondimensional equation:

$$Q^* = \delta^*(r_o^* - 1)\int_1^{r_o^*} \frac{r^{*3}}{r_o^* - \delta^* - 1 + \delta^* r^*} dr^* \quad \text{where} \quad Q^* = \frac{Q\delta}{2\pi\mu\omega^2 r_i^4} \tag{39}$$

Performing the integration

$$Q^* = (r_o^* - 1)[\frac{(r_o^{*3} - 1)}{3} - \frac{1}{2}\frac{(r_o^* - \delta^* - 1)}{\delta^*}(r_o^{*2} - 1) + \frac{(r_o^* - \delta^* - 1)^2}{\delta^{*2}}(r_o^* - 1) - \frac{(r_o^* - \delta^* - 1)^3}{\delta^{*3}}(\ln(\frac{(r_o^* - \delta^* - 1)}{\delta^*} + r_o^*) - \ln(\frac{(r_o^* - \delta^* - 1)}{\delta^*} + 1))] \tag{40}$$

This equation indicates that the nondimensional viscous heat generation is a function of two parameters, r_O*and δ^*.

Seal Design Curves

Three critical parameters that determine the performance of the actively controlled seal are the stiffness, controllability, and the viscous heat generation. Equations 32, 35, and 40 express these parameters as a function of three variables, P_i^*, r_O^*, and δ^*. For a given seal design, P_i^* is usually a design constraint; two design variables then remain. These design variables also specify the opening force. Accordingly, specifying r_O^* and the opening force also determines the seal performance parameters. For equilibrium conditions, the opening and closing forces are equal; therefore specifying the opening force, also specifies the closing force. The initial role of the seal designer is then to specify the closing force and seal geometry (r_O^*) to maximize the seal stiffness and controllability, while minimizing the viscous heat generation. The following design curves present the relationship between the design variables (F^*_{close} and r_O^*) and the seal performance parameters.

Figure 3-2 presents $1/\delta^*$ (to which the controllability is proportional) and K^* as functions of F^*_{close} for various values of r_o^*. These curves are for P_i^* equal to 0.068, which represents a sealed pressure of 1.48×10^6 Pa at the high pressure side and ambient pressure at the low pressure side. These curves demonstrate that maximizing the controllability and stiffness impose conflicting demands on the choice of F^*_{close}. The controllability increases as F^*_{close} decreases while the stiffness increases as F^*_{close} increases. The controllability also increases as r_o^* increases while the stiffness may either increase or decrease as r_o^* increases, depending on the value of F^*_{close}.

Figure 3-3 presents $1/\delta^*$ and Q^* as functions of F^*_{close} for various values of r_o^* where P_i^* is equal to 0.068. These curves demonstrate that maximizing the controllability while minimizing the viscous heat generation impose consistent demands on the choice of F^*_{close}. These quantities respectively increase and decrease as F^*_{close} decreases. The nondimensional viscous heat generation may either increase or decrease as r_o^* increases, depending on the value of F^*_{close}.

Figures 3-2 and 3-3 provide a rational basis from which to choose an optimum F^*_{close} and r_o^* to maximize the controllability and stiffness of the seal, while minimizing the viscous heat generation. Once these parameters are chosen, the next step in determining the seal geometry is to select the inside radius of the face of the floating component. The outside radius of the seal, and the dimensional closing force, can then be computed from Equations 21 and 29, respectively, for given sealed pressures. Once the dimensional closing force is known, the spring force must be chosen. The balance ratio can then be determined from Equation 1. Equation 3 provides a means for determining the balance radius, from the balance ratio. The basic seal geometry is now known.

Once the basic geometry of the seal is determined, the next step in the seal analysis (or design) is to determine the coning deformations of the seal faces produced by the

voltage, pressure, and thermal loads. These deformations have a direct effect on the film thickness, the leakage rate, the dimensional seal stiffness, and the dimensional viscous heat generation. The coning deformations can be computed with the finite element method.

Finite Element Model

The finite element method was used to compute the coning deformations of the stator and the rotor produced by the voltage, pressure, and thermal loads imposed on the seal. This method is based on discretizing the solution domain into elements and approximating the differential equations over each element utilizing variational principles or weighted residual methods. A detailed description of the finite element method can be found in many texts [e.g., Bath, 1982; Cook, 1981].

Structural Model

The structural components of the actively controlled mechanical seal include a piezoelectric element with a carbon face, a holder in which the piezoelectric element operates, and a rotating face. Each of these components affects the deformations of the seal faces and therefore influences δ. These deformations were computed with ANSYS, a commercially available finite element program.

Figures 3-4 and 3-5 present the finite element models of the floating component and rotating face of the seal. The model of the floating component consists of a piezoelectric element with a carbon face and a holder. The O-rings, O-ring grooves, holes for the thermocouple leads, and the epoxy that bonds the carbon face to the piezoelectric element are not included in the finite element model of the floating component.. Both models are axisymmetric with a dimension of 3.5 degrees in the circumferential direction. This angular dimension maintains reasonable aspect ratios.

The piezoelectric element is modeled by the STIF5 element of the ANSYS library [DeSalvo and Gorman, 1989]. This is a 3-dimensional, 8-noded brick element with translational (x,y,z), voltage, temperature, and magnetic degrees of freedom at each node for a total of 6 degrees of freedom per node. The formulation of the STIF5 element is based on a variational principle [Alik and Hughes, 1970]. The carbon face, holder, and rotor are modeled with the STIF45 element of the ANSYS Library [Desalvo and Gorman, 1989]. This element is a 3-dimensional, 8-noded brick element. Each node has x, y, and z translational degrees of freedom for a total of 3 degrees of freedom per node. PZT-5H is the material for the piezoelectric actuator and the holder material is boron nitride. The face materials are carbon (for the stator) mated with tungsten carbide. Material properties for these elements are presented in Appendix B.

Both models are axisymmetric. The boundary conditions that enforce axisymmetry include suppressing all circumferential degrees of freedom and constraining all nodes with identical r and z coordinates to have identical displacements.

Additional boundary conditions for the floating component are imposed at the boundary between the deformable face assembly and the holder, and at the boundary between the holder and the turbopump housing. The deformable face assembly is seated in the holder with an O-ring that allows relative motion between the deformable face assembly and the holder. This boundary condition is modeled with the STIF52 element of the ANSYS Library. This is a gap element which behaves as a spring with infinite stiffness as it is compressed, but provides no stiffness in tension.

The boundary condition between the turbopump and the holder is modeled by suppressing the axial motion of the holder at the point where the O-ring contacts the holder. This constraint does not exert a stress on the finite element model because the

pressure and spring forces that act on the floating component are balanced in the axial direction.

The boundary conditions imposed on the rotor include the two following constraints: all degrees of freedom at the inside radius of the rotor are suppressed, and the axial degrees of freedom located in the r-θ plane at the midplane of the rotor are suppressed. The first boundary condition is based on the assumption that the rotor is rigidly attached to the shaft of the turbopump and the shaft is assumed to have no deformation. The second boundary condition is equivalent to assuming that the pressure and thermal loads are identical on both sides of the rotor. This will generally not be true, however the error in this assumption is much smaller than those due to other assumptions made in the model (e.g. the thermal boundary conditions).

Heat Transfer Model

Thermal strains can have a significant effect on the deformations of a seal and thereby influence the coning. Therefore, a model that computes the temperatures within the structural components is necessary to predict the performance of a seal. The finite element method was used to model this temperature distribution. A description of the finite element method applied to heat transfer problems is presented in several references [e.g., Bath, 1982; Cook, 1981].

The finite element meshes used in the heat transfer analysis are identical to those used for the structural analysis which are presented in Figures 3-4 and 3-5. The STIF70 element of the ANSYS Library was used [DeSalvo and Gorman, 1989]. This element is a 3-dimensional, 8-noded brick element with temperature as the only degree of freedom per node.

The finite element models used in the heat transfer analysis are axisymmetric. This condition is enforced by eliminating temperature gradients in the angular direction. The

rotor is also symmetric with respect to its midplane (r-θ plane) as shown in Figure 3-6. This symmetry condition is enforced by constraining this plane to be adiabatic.

Conduction within the seal components, convection at the inside and outside radii of the components, and heat generation in the gas film are included in the model. Precise prediction of the required convective boundary conditions would require a detailed description of the flow field within the sealed cavity and computation of the temperatures of all the components in contact with the seal. This would require an extremely large computational effort, which was considered beyond the scope of this mathematical model. Therefore, considerable simplifications were made in the heat transfer analysis, as described below.

Figure 3-6 presents the thermal boundary conditions for the heat transfer analysis. The convective boundaries include the outside and inside radii of the floating component, and the outside radius of the rotor. The conduction boundary conditions include the inside radius of the rotor where it contacts the shaft, and the location where the O-ring, which is located between the holder and the turbopump housing, contacts the holder. There is also a heat flux into the seal faces due to the viscous generation within the gas film.

The convective coefficient at the outside radius of the floating component is assumed to be zero (perfectly insulated). This assumption simplifies the thermal model and is probably a good assumption considering that no axial flow path exists at the outside radius of the seal, and the surrounding fluid is a gas with low thermal conductivity.

The convective coefficient at the inside radius of the seal and the bulk temperature of the fluid at the outside and inside radii were adjusted such that the face temperatures computed by the mathematical model matched the measured face temperatures to within a few degrees C. The experimental results provide two key parameters to estimate the heat transfer properties at the inside radius of the stator: the face temperature, and the variation

of the face temperature as the voltage (and film thickness) of the seal changed. In the mathematical model, the face temperature increases as the convective coefficient is decreased, and as the bulk temperature of the fluid is increased. The variation in face temperature with voltage increases as the convective coefficient is decreased. These trends provide a means to adjust the mathematical model such that the face temperatures match the face temperatures from the experimental results.

An alternate means of setting the thermal boundary conditions would have been to set the bulk temperature of the fluid equal to the cavity temperature, which was measured during the seal tests. However, this eliminates one of the adjustable parameters and results in a larger discrepancy between measured and computed face temperatures (see Chapter VIII - Comparison of Numerical Model with Experimental Results).

Adjusting the heat transfer coefficients involves an iterative procedure. The first step involves adjusting the bulk temperature such that the average face temperature matches the experimental face temperature at a certain voltage level. The second step involves adjusting the convective coefficient such that the computed change in face temperature matches the experimental change in face temperature as the voltage is varied. Steps one and two are then repeated until the face temperatures match reasonably well at each voltage level. Typically the face temperatures agreed to within 5 °C.

The convective coefficient at the outside radius of the rotor is based on a study in which convection coefficients were measured for a similar geometry [Gazley, 1958]. Based on this study a convective coefficient 537 W/(m^2 K) is used at the outside radius of the rotor [Wolff, 1991]. The bulk temperature at the outside radius of the rotor is set equal to the bulk temperature of the fluid at the inside radius of the holder.

Conduction boundary conditions occur at the inside radius of the rotor where it contacts the shaft, and at the contact point between the holder and the housing. The rotor

is assumed to be in close thermal contact with the shaft and is therefore fixed at the shaft temperature, assumed to be the bulk temperature of the fluid at the inside radius of the holder. The contact point between the O-ring and the holder is assumed to be adiabatic. This contact point is relatively far from the seal face, so its effect on seal face temperatures is ignored.

For each element of the seal faces adjacent to the gas film, there is a heat flux into the element due to the viscous generation within the film. The model used to compute these heat transfer effects is based on several simplifying assumptions. First, all viscous heat generation within the gas film is due to the angular velocity of the rotor. Equation 40 is then used to compute the heat generation rate. Second, all heat generated within the gas film flows into the seal faces, therefore no heat is convected out with the seal leakage. This is generally valid for face seals because the gas film is very thin and in contact with the seal faces which have relatively high thermal conductivities. Third, the heat is apportioned between the seal faces in direct proportion to their relative thermal conductivities. In reality, the proportion of heat which flows into each seal face is affected by its geometry, thermal conductivity, and thermal boundary conditions. However, the model was considerably simplified by apportioning the heat based on the relative thermal conductivities of the seal faces and the errors resulting from this assumption are less significant than the errors introduced by other approximations made in the model. The heat flow per node for the elements of the seal faces is then computed by dividing the heat flow for each element equally between the nodes.

Computation of Seal Performance

Once the fluid mechanics model and finite element models are developed, it is then possible to compute the film thickness and leakage rate of the seal. The parameters that

the finite element model require include the seal geometry, the material properties, and the boundary conditions. Figure 3-7 presents the iterative procedure that is used to determine these performance parameters.

The first step is to compute the temperature distribution within the seal components, which results from the bulk temperature of the fluid and the convective boundary conditions. This is done with the finite element program ANSYS. This produces an initial temperature distribution that is used in the third step to give an initial estimate of the thermal deformations. No viscous heat generation is included for this step.

The second step is to determine δ^* (δ/h_j). First, the closing force is computed from Equation 1. Next, a value for δ^* is assumed and the pressure profile and opening force are computed. The opening and closing forces are compared and δ^* is modified using the modified regula falsi method. This procedure is repeated until the difference between the closing force and opening force is less than 0.001 N. The temperature distribution which was computed from the previous step is also read, and these temperatures are written to an ANSYS batch file.

For the third step, the deformations of the seal faces are computed with ANSYS. These deformations are due to voltage, pressure, and thermal loads from the temperature distribution computed in step 1. At this stage, the thermal load does not include viscous heat generation.

Once the deformations of the seal faces are known, the film thickness is computed in the fourth step. The faces are assumed to have a linear profile and δ is computed from Equation 24. From the coning, the film thickness at the inside radius of the seal faces is determined from Equation 23, which determines the viscous heat generation rate produced within the film. The viscous heat generation rate is written to an ANSYS batch file for use in the thermal analysis of the next step.

The fifth step consists of recomputing the temperature profiles within the seal components with ANSYS. Viscous heat generation as well as the thermal boundary conditions are then accounted for.

For the sixth step, the temperature profiles computed in the previous step are read from a data file, and an ANSYS batch file is written to compute the deformations of the seal faces.

New deformations of the seal faces are computed in the seventh step with ANSYS. These deformations also include voltage and pressure loads.

The eighth step consists of computing a new film thickness based on the coning that is produced by the deformations determined from the previous step, and computing a new viscous heat generation rate based on the modified film thickness. This new film thickness is compared with the old film thickness, and the new temperature distribution is compared with the old temperature distribution. If the film thicknesses differs by less than .001 μm, and the temperature distributions differs by less then 1 °C, then the solution for this voltage level is assumed to have converged. If this convergence criterion is not met, the computational procedure resumes at step 5.

For low voltage levels that produce a very thin gas film, it is necessary to relax the coning deformation in step 8 to achieve convergence:

$$\delta = \delta_{old}(1-\kappa) + \delta_{new}\kappa \tag{41}$$

where κ is chosen to be between 0 and 1 (typically 0.6). Because the coning is relaxed, large changes in film thickness are prevented, which in turn prevents large increases in the viscous heat generation rate. This helps the solution to converge when the viscous heat generation becomes large as a result of small film thicknesses. If the film thickness

becomes too thin (less than .001 μm) the faces are assumed to have contacted and the computation is stopped.

In the ninth step, a new voltage load is written to an ANSYS batch file and the computational procedure then resumes at the fifth step. If the results from all the voltage levels have been computed, the computations are finished. Seven voltage loads are applied for each computational run: 3000, 2500, 2000, 1500, 1000, 500, and 0 volts. Best performance for this computational procedure is achieved when the voltage loads are applied in decreasing order. As each solution is obtained, it is used as an initial guess for the computation of the next voltage load.

The results obtained from the mathematical model include the film thickness at the inside radius of the seal faces, the coning, the leakage, the temperature profiles of each seal component, and the pressure profile within the gas film. These results are obtained for each specified voltage level.

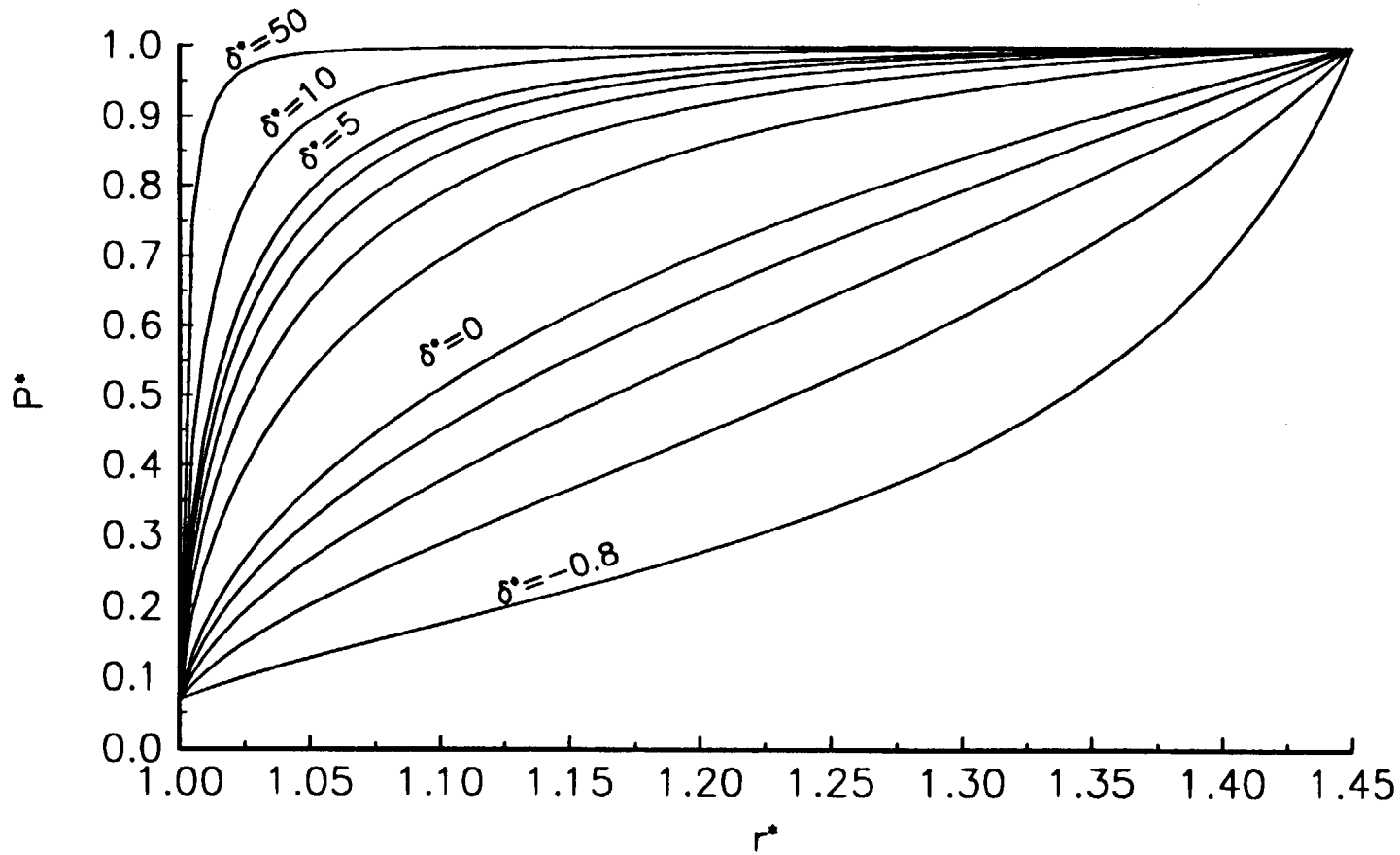

Figure 3-1. Nonndimensional Pressure Distribution

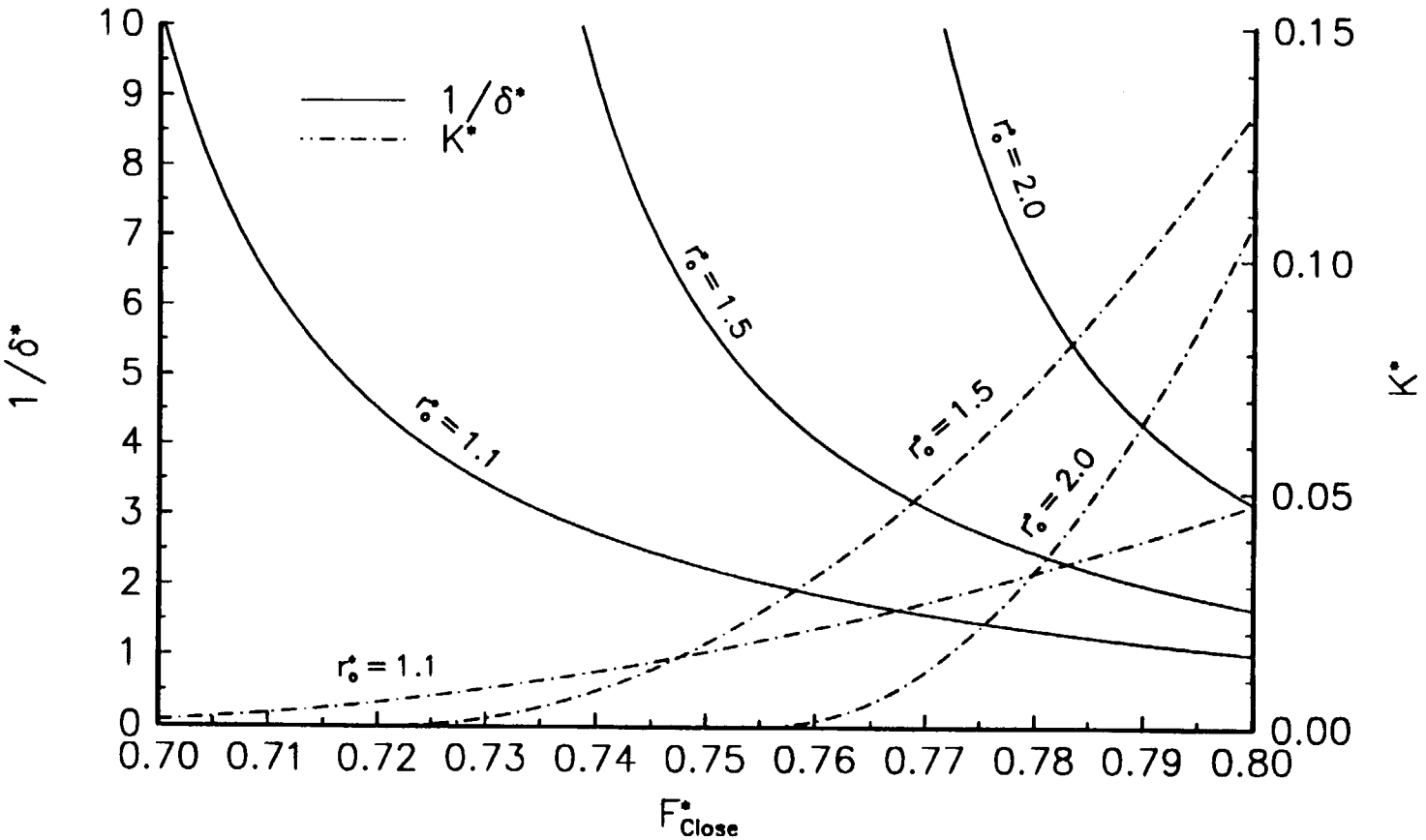

Figure 3-2. Nondimensional Seal Design Curves - 1/δ* and Siffness versus Closing Force

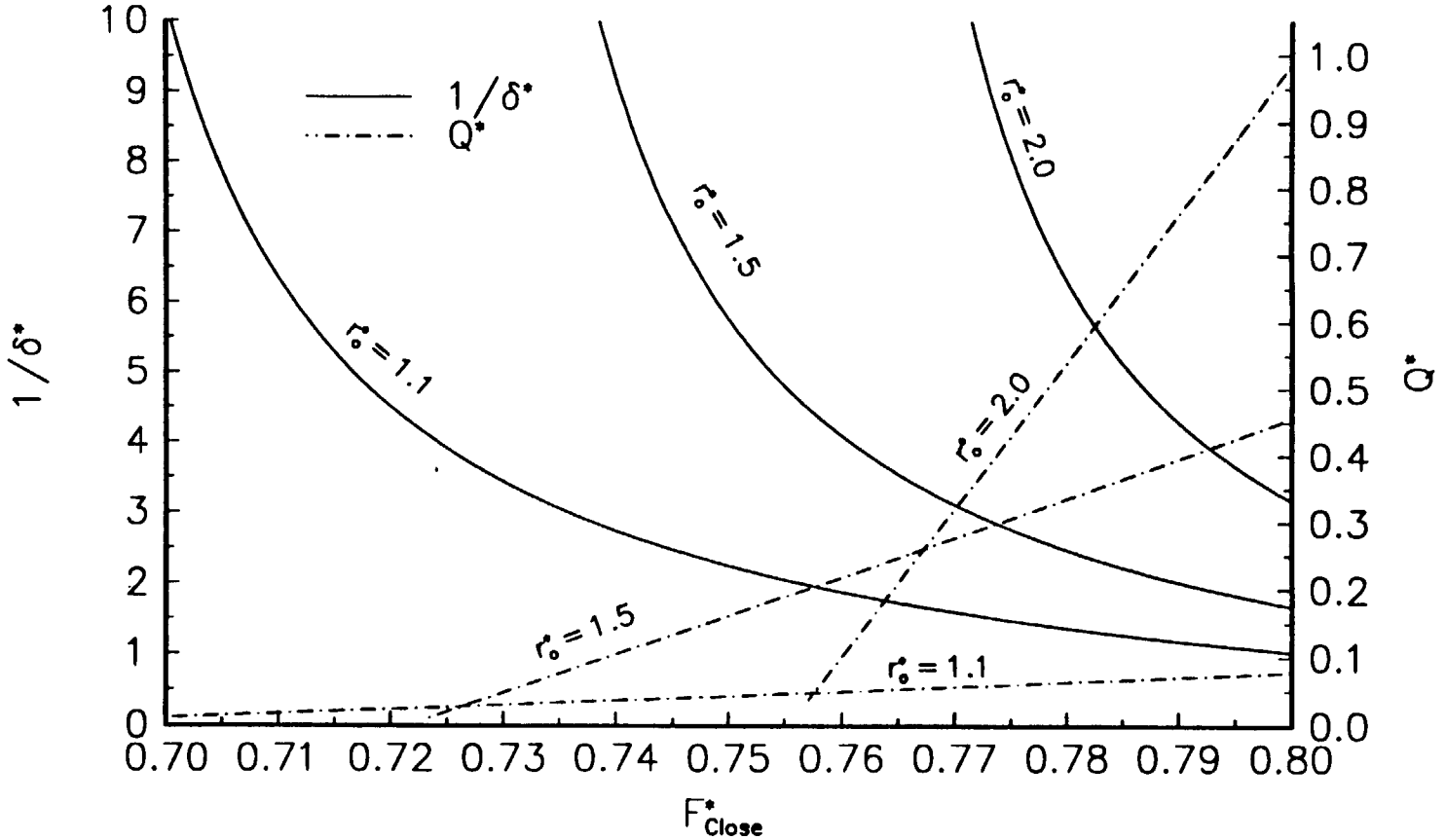

Figure 3-3. Nondimensional Seal Design Curves - 1/δ* and Viscous Heat Generation versus Closing Force

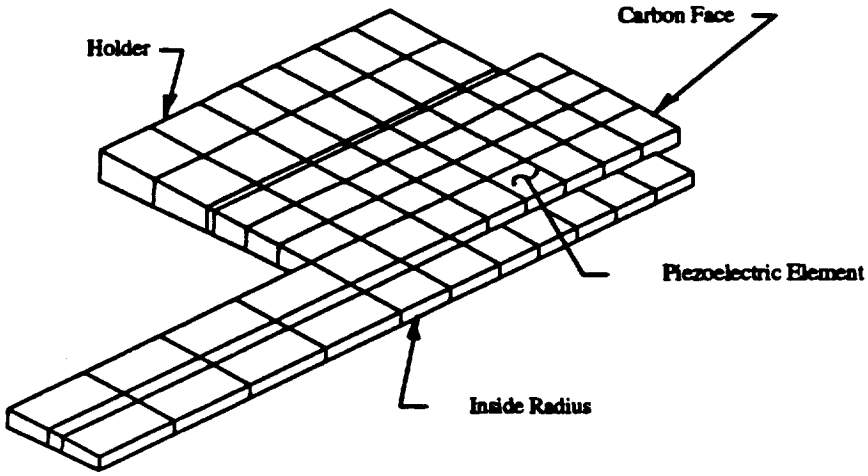

Figure 3-4. Finite Element Model of Stator

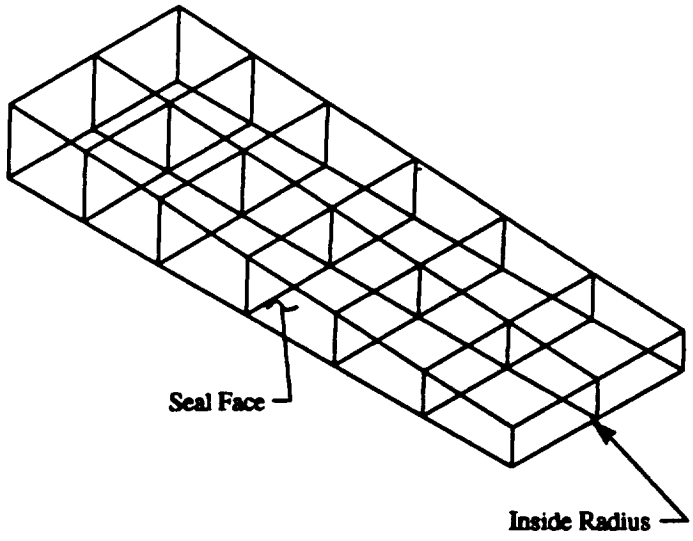

Figure 3-5. Finite Element Model of Rotor

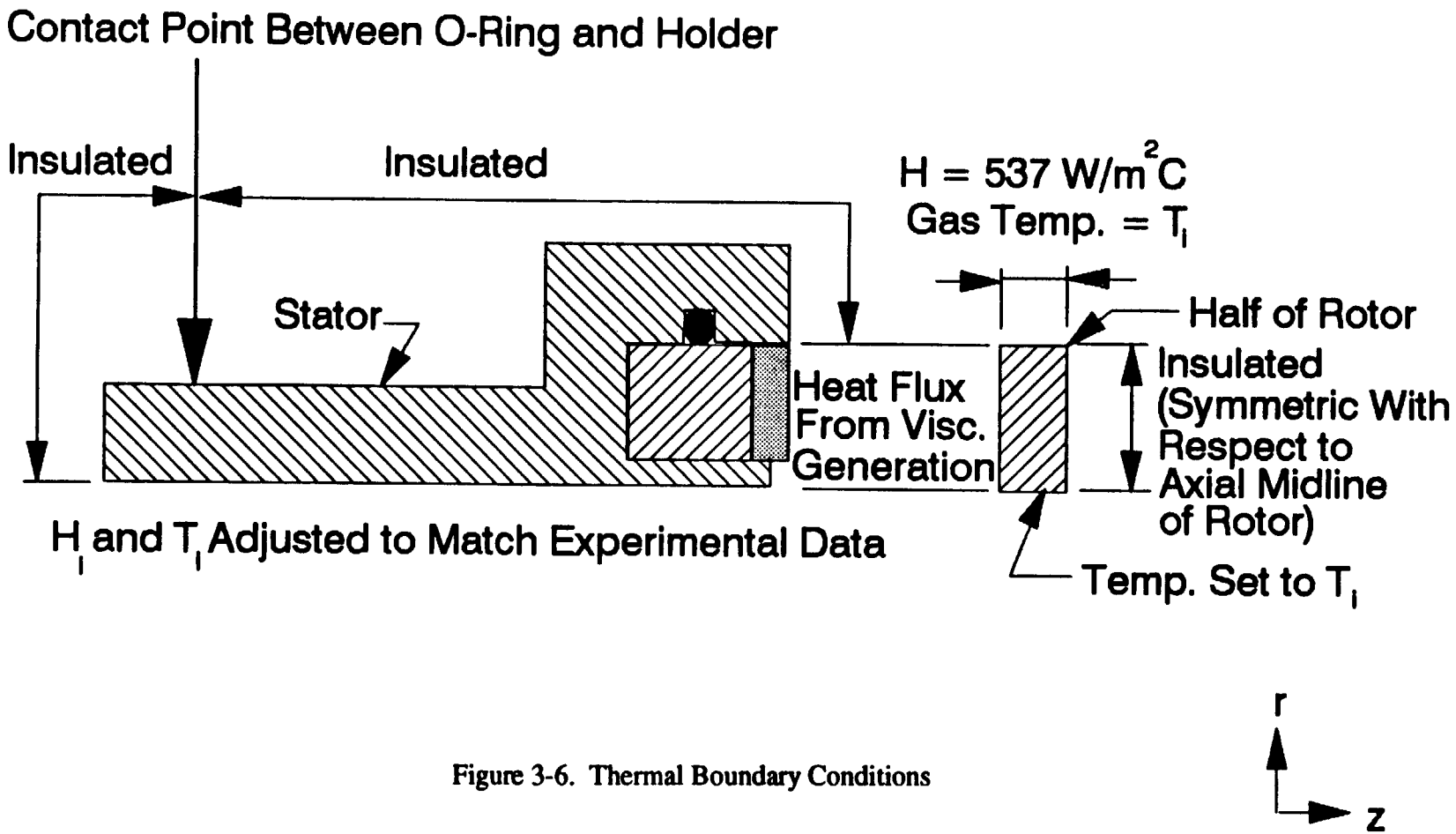

Figure 3-6. Thermal Boundary Conditions

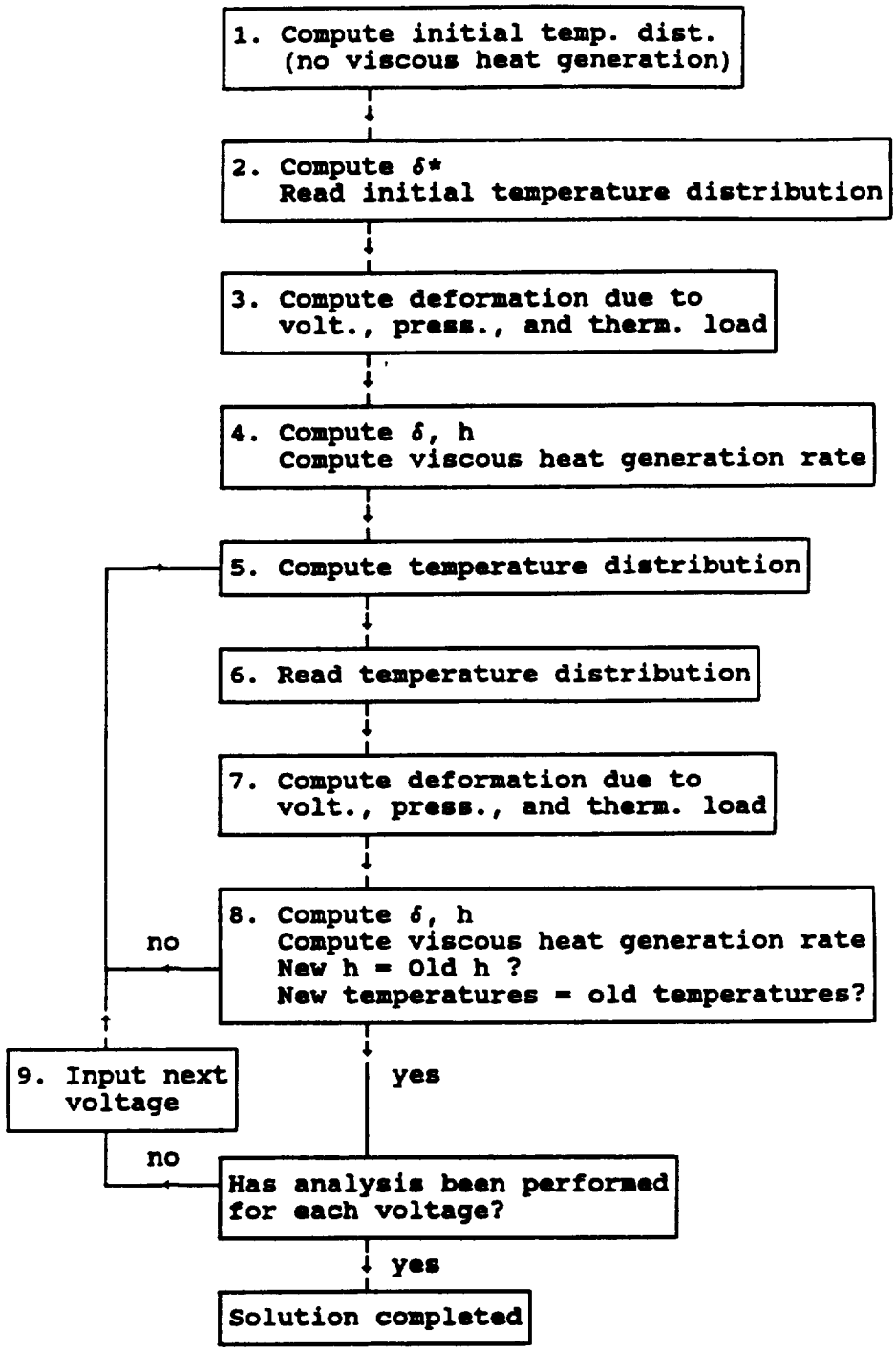

Figure 3-7. Computational Procedure

CHAPTER IV

SEAL DESIGN

The intent of this study is to design a mechanical seal to replace the floating ring seals in the helium purge assembly of a liquid oxygen turbopump. Figure 4-1 presents a diagram of a typical turbopump. Hot turbine gases enter on one side and drive the turbine of the turbopump. This causes the pump impeller on the opposing side of the turbopump to rotate, thereby pumping the liquid oxygen. If the hot gases come in contact with the liquid oxygen, components of the turbine could ignite and a catastrophic explosion would result. Contact between the liquid oxygen and hot gases is prevented with a series of seals that includes the helium purge assembly, presented in Figure 4-2. Pressurized helium is introduced near the midpoint of the turbopump, and flows axially outward, away from the helium purge assembly, toward both the turbine rotor and the pump impeller. This prevents contact between the hot gases and liquid oxygen.

Current liquid oxygen turbopump designs utilize double floating ring seals in the helium purge assembly, as shown in Figure 4-2. Actively controlled mechanical seals present a promising alternative to floating seals because they could significantly reduce the helium leakage without sacrificing reliability. A double seal configuration was chosen to replace the floating ring seals. A schematic of the seal is presented in Figure 4-3, and a photograph of the seal components is presented in Figure 4-4. The components for this configuration include two nonrotating floating components (stators) and one rotating face (rotor). Each stator consists of a holder, a deformable face assembly, springs, and two secondary seals.

The size and operating conditions of a liquid oxygen turbopump impose severe constraints on the design of a mechanical seal. The dimensions of the seal envelope are presented in Figure 4-5, and are 38.1 mm (1.50 in) in the axial direction and 12.7 mm (0.50 in) from the outside radius of the shaft to the outside radius of the envelope. These dimensions are considerably smaller than those of previous actively controlled seals. The high pressure and low pressure side of the seal are at 1.38×10^6 (185 psig) and 1.1×10^5 Pa (1 psig), respectively. The temperatures that affect the performance of the seal include the temperature of the hot gas and helium drain (196 °C), the temperature of the liquid oxygen and helium drain (-150 °C), and the temperature of helium entering the purge assembly (21 °C). These temperatures impose significant thermal gradients across the relatively small seal envelope. An additional design consideration is that the shaft of the turbopump operates at 7,330 rad/sec (70,000 rpm).

The intent of this study is to perform an initial demonstration of the feasibility of an actively controlled seal for aerospace applications. Therefore, the seal was not tested at the actual operating conditions, but in a less severe environment. The tests described in this study were at ambient temperature and at a maximum rotational speed of 3770 rad/sec (36,000 rpm). These less severe conditions simplified the test rig and testing procedures, but still served as a valid demonstration case.

The seal design presented below was accomplished through an iterative procedure of design, fabrication, testing and then redesign. The initial phases of the design process are presented elsewhere [Wolff, 1991]. During the experimental phase presented here, the seal design was modified, and the final design is presented below. Also included is a discussion of the primary design considerations that led to the final seal configuration.

Design of the Seal Stator

The seal stator consists of a deformable face assembly, a holder, O-rings, and six coil springs. The deformable face assembly consists of a piezoelectric element, a carbon face, electrodes, wires to the electrodes, and a thermocouple embedded in the carbon face.

Design of Deformable Face Assembly

The deformable face assembly is the principal component of the actively controlled mechanical seal. With this component, the coning deformation of the carbon face can be adjusted, thereby changing the film thickness and leakage rate of the seal. The design considerations for this component include meeting the size constraints to fit in the seal envelope, producing a large range of coning deformation, and having the correct face area to create a favorable balance ratio. The detailed design drawings of the deformable face assembly are presented in Figure A-2

Coning deformation (see Figure 1-1) can be produced with several different configurations of piezoelectric materials. The type of deformation produced in a piezoelectric material depends on the direction of the applied electric field relative to the direction of the poling axis. The piezoelectric effect is produced in various materials by a polarizing treatment (during the manufacturing process) in which a d.c. electric field is applied to the material while the material is at a high temperature. The direction of the d.c. field defines the poling axis for the material. When an electric field is applied to the finished material in the same direction as the poling axis, the material expands in that direction. Conversely, the material contracts if an electric field is applied in a direction opposite to the poling axis. Shear deformation is produced by applying an electric field perpendicular to the poling axis. Based on finite element analyses of various configurations performed in a previous study [Wolff, 1991], it was found that the shear

mode of deformation produced the largest amount of coning. This mode of deformation is therefore utilized in the present study.

Figure 4-6 presents a configuration in which a coning deformation of the carbon face is produced by a shear deformation of the piezoelectric element. This figure presents half of a cross sectional view of the deformable face assembly. The shear mode of deformation is induced by applying an electric field in the axial direction while the poling axis is in the radial direction. Two electrodes are required to create the electric field, one on each axial face of the seal. The carbon face, which is bonded to one face of the piezoelectric element with conductive epoxy, serves as the ground electrode. Copper foil is bonded to the other axial face with conductive epoxy, and serves as the high voltage electrode. The deformable face assemblies are configured such that a positive voltage produces a positive coning.

The type of piezoelectric material directly affects the magnitude of the coning deformation produced by a given voltage. There are a large number of commercially available piezoelectric materials, which are tailored to suit various applications. The governing criterion for this design is to obtain the maximum amount of deformation for a given voltage. The strains induced as a function of the electric field can be determined by examining the [d] matrix of the piezoelectric material [Wolff, 1991]. The coefficients of the [d] matrix that govern the shear and axial mode of deformation are the d_{15} and d_{33} coefficients, respectively. PZT-5H is used in this study because it has relatively large d_{15} and d_{33} coefficients, and is readily available. The piezoelectric material used in this study was obtained from American Piezo Inc., Mackeyville, Pennsylvania.

Figure A-3 presents the detailed design drawings for the carbon face that is bonded to the piezoelectric element. The type of carbon used is P-658RC (from the Pure Carbon Company, St. Marys, Pennsylvania), which is a resin impregnated carbon. It is necessary

to specify the proper radial dimensions to produce a favorable balance ratio, and to make the face thin enough such that it is readily deformed by the piezoelectric element. Four slots are machined in the backside of the carbon face for two anti-rotation pins, a thermocouple, and a pass through for the high voltage wire.

The balance ratio plays a key role in determining the controllability and stiffness of the seal (see Chapter III - Mathematical Model). Figures 4-7 and 4-8 present plots of $1/\delta^*$ (to which controllability is proportional) and stiffness versus closing force for the seal configurations of the helium and air steady state tests, respectively, and the closing force that was chosen for each test.

Two different balance ratios were used during these seal tests, 0.748, and 0.766. For the helium steady state tests and some initial steady state tests in air, the balance ratio was 0.748. During some of these tests, dynamic instabilities were observed at higher rotational speeds. In an effort to eliminate these instabilities, the balance ratio of the seal was increased to 0.766, which produced a larger axial stiffness, and a lower controllability (see Chapter VII - Comparison of Numerical Model with Experimental Results). After increasing the balance ratio, problems with dynamic instabilities were still encountered and were probably due to excessive misalignment between the seal faces. The dimensions presented in A-3 are for the balance ratio of 0.766. For the seal faces with a balance ratio of 0.748 the radial dimensions are 23.62 mm (0.930 in) for the inside diameter, and 34.93 mm (1.375 in) for the outside diameter.

The thermocouples embedded in the carbon face to monitor face temperature are type J, iron-constantin thermocouples having wire diameters of 0.25 mm (0.010 in). The anti rotation pins are made from music wire having a diameter of 1.02 mm (0.040 in).

Design of Holder

The final detailed design drawing of the holder is presented in Figure A-4. It is necessary for the holder to define the correct geometry such that a favorable balance ratio is produced (see Design of Deformable Face Assembly, above) and to provide an enclosure for the piezoelectric element such that secondary gas leakage and high voltage breakdown are prevented.

The material chosen for the holder is boron nitride, produced by the Carborundum Company, Niagara Falls, New York. Boron nitride is a machinable ceramic, which has high thermal conductivity (see table of material properties), but is electrically insulating. Such a combination of properties is favorable for the actively controlled seal. The high thermal conductivity allows heat to be conducted away from the seal faces, thereby preventing excessive face temperatures. The electrical insulating properties enable the high voltage electrode of the deformable face assembly to sustain the voltages applied to it.

The deformable face assembly is seated in the holder with an O-ring around the outer circumference. This method of assembly prevents secondary leakage while facilitating ease of fabrication. In addition, this design presents the fewest constraints on the boundary of the deformable face assembly, which maximizes the coning deformation for a given voltage.

The holder provides a seat for the deformable face assembly, and also insulates the piezoelectric element from the helium, which has a particularly low dielectric strength [Paul and Burrowbridge, 1969]. Initially, the holder did not completely enclose the piezoelectric element and voltage breakdown occurred between the inside radius of the piezoelectric element and the shaft of the test rig. Therefore, the holders were modified to completely enclose the piezoelectric element (see Figure A-4). This configuration had

limited success in preventing high voltage breakdown in helium. Therefore, the seal was tested in air in which no voltage breakdown problems occurred (see Chapter V- Experimental Equipment and Test Procedures).

Selection of O-Rings

There are two O-rings used in each stator to prevent secondary leakage, one located between the test rig housing and holder, and one located between the holder and outer circumference of the deformable face assembly. The principal criteria that determine the O-ring design and selection is the need to prevent secondary leakage while not excessively restricting axial motion of the seal components. Therefore, light O-ring squeezes are utilized, especially for the O-ring between the holder and housing. Both O-rings are made from Buna-N with a durometer hardness of 70, which is widely available and well suited for the laboratory test conditions.

The O-ring between the holder and the test rig housing is an AS568A-121 O-ring having an inside diameter of 26.64 mm (1.049 in) with a thickness of 2.62 mm (0.103 in). The outside diameter of the O-ring groove in the housing is 31.62 mm (1.245 in) and the holder diameter on which the O-ring is seated is 26.92 mm (1.060 in). These dimensions produce an O-ring squeeze of 10.3 percent.

The O-ring between the holder and deformable face assembly is an AS568A-028 O-ring having an inside diameter of 34.65 mm (1.364 in) with a thickness of 1.78 mm (0.070 in). The outside diameter of the O-ring groove in the deformable face assembly is 37.97 mm (1.494 in) and the outside diameter of the deformable face assembly on which the O-ring is seated is 34.93 mm (1.375 in). These dimensions produce an O-ring squeeze of 14.6 percent.

Selection of Springs

A light spring load is required to produce a favorable closing force to maximize the controllability of the seal. Therefore, coil springs are utilized to provide the spring load; they have an axial length of 15.75 mm (0.620 in) and a diameter of 2.24 mm (0.088 in) (Associated Spring Raymond, Corry, Pennsylvania, Part No. C0088-010-062 M). These springs are made from music wire 0.25 mm (0.010 in) in diameter and have a spring constant of 0.333 N/mm (1.9 lb/in).

Six coil springs are utilized for each stator. They are compressed 5.72 mm (0.225 in) while in place in the test rig which produces a spring force of 1.9 N (0.4 lb) for each spring. Therefore, the combined spring load for the six springs is 11.4 N (2.6 lb).

Design of the Seal Rotor

The detailed design of the rotor is presented in Figure A-6. The primary considerations for the selection of the rotor is that it has good wear characteristics, and that it can withstand the centrifugal stresses that are imposed on it. Tungsten carbide was chosen as the material for the rotor, which has good wear characteristics when mated with a carbon face..

The primary strength consideration for the rotor is to ensure that it can withstand the centrifugal stresses that are produced by high rotational speeds. To compute these stresses, a finite element analysis was performed of the seal rotor at a rotational speed of 7,330 rad/sec (70,000 rpm), which is the operating speed of the liquid oxygen turbopump. The maximum principal stress, which occurred at the inside radius of the rotor, was 70.8 MPa (10.3 kpsi). A strength theory generally used for brittle materials (such as tungsten carbide) is to compare the ultimate tensile strength of the material with the maximum principal stress [Budynas, 1977]. For tungsten carbide, the bending strength (which is an

indirect measure of the tensile strength) is 1700 MPa (246.6 kpsi) [Cleaver, 1988] which is much larger than the principal stress previously computed. Therefore, a tungsten carbide rotor is strong enough to withstand the centrifugal stresses produced by a shaft speed of 7330 rad/sec, and is also suitable for the lower operating speeds of these seal tests.

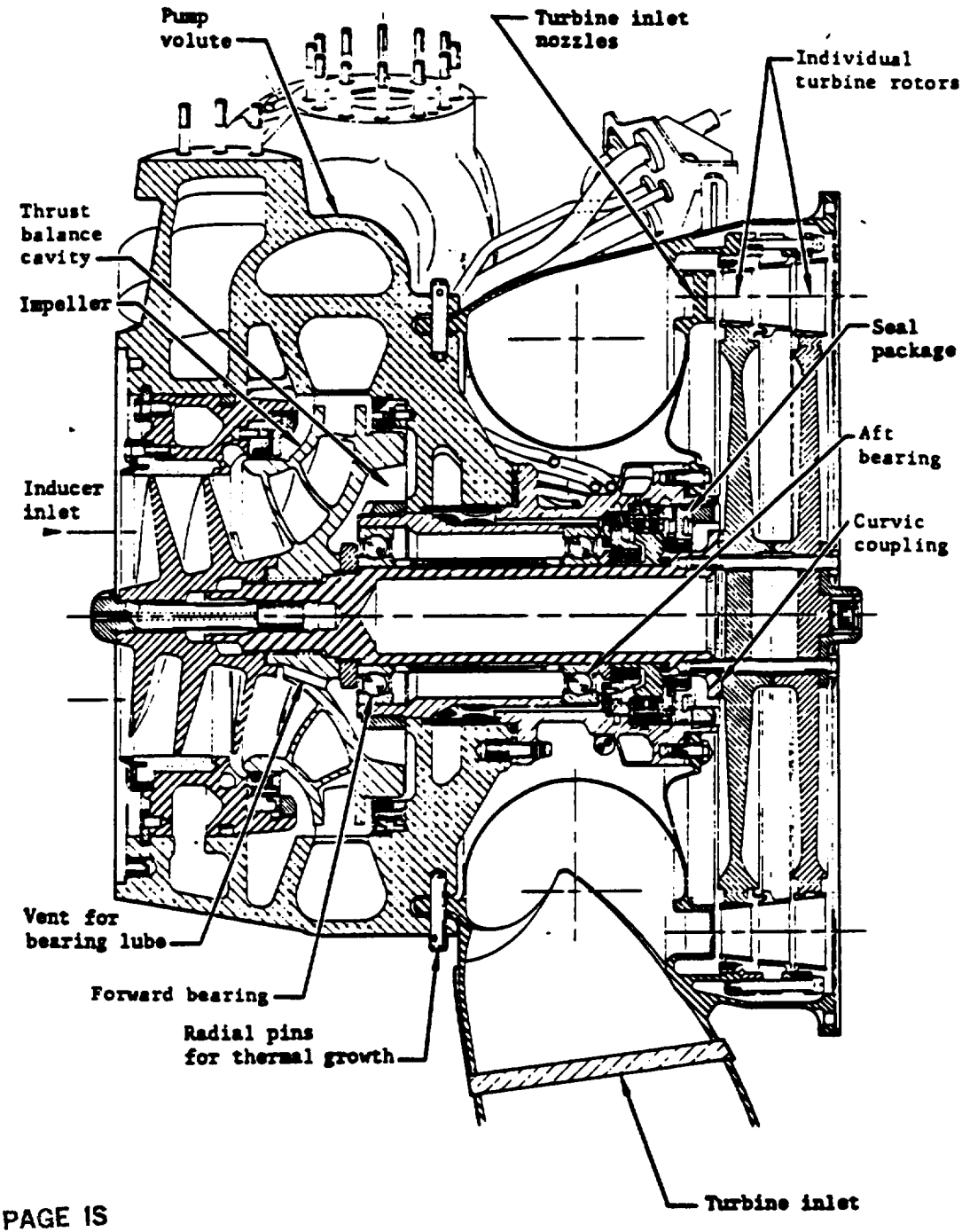

Figure 4-1. Schematic of a Typical Turbopump
From Sobin and Bissel [1974]

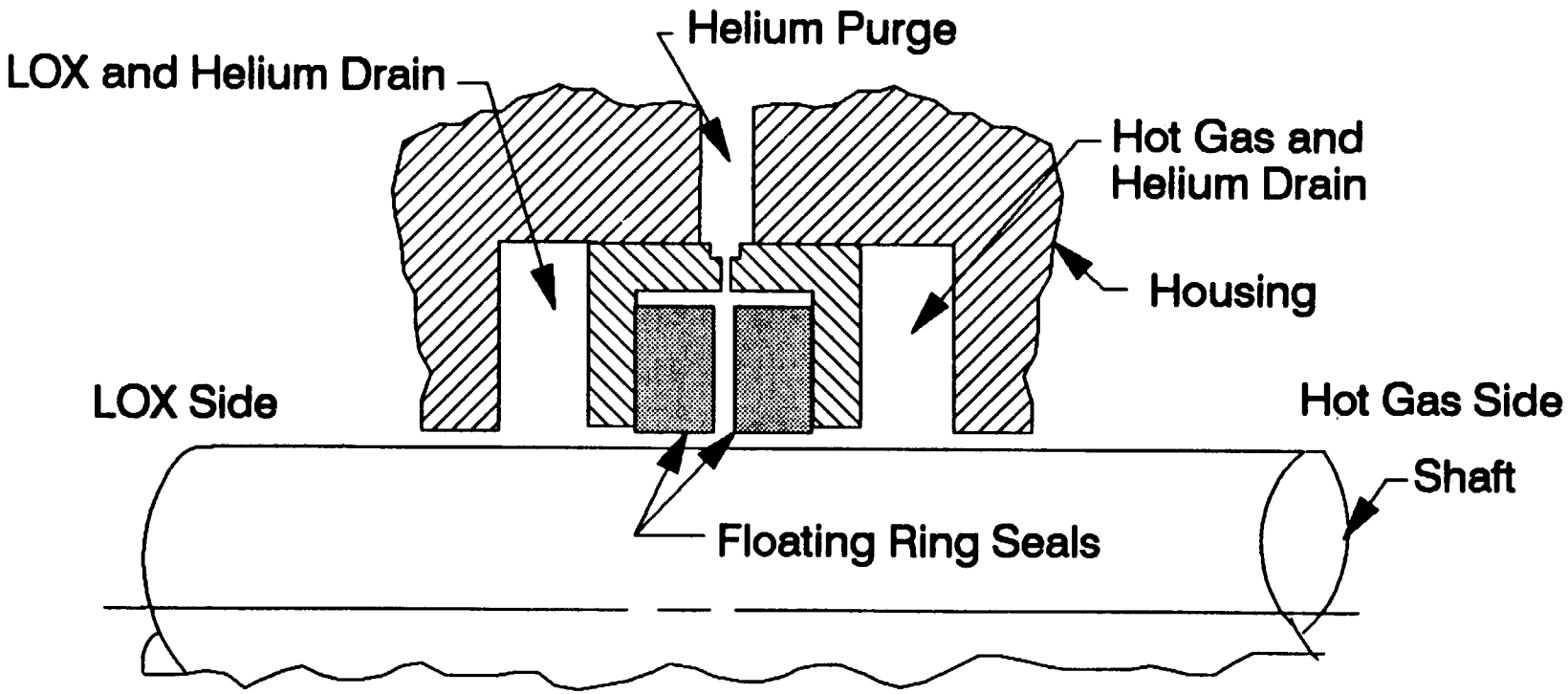

Figure 4-2. Helium Purge Assembly

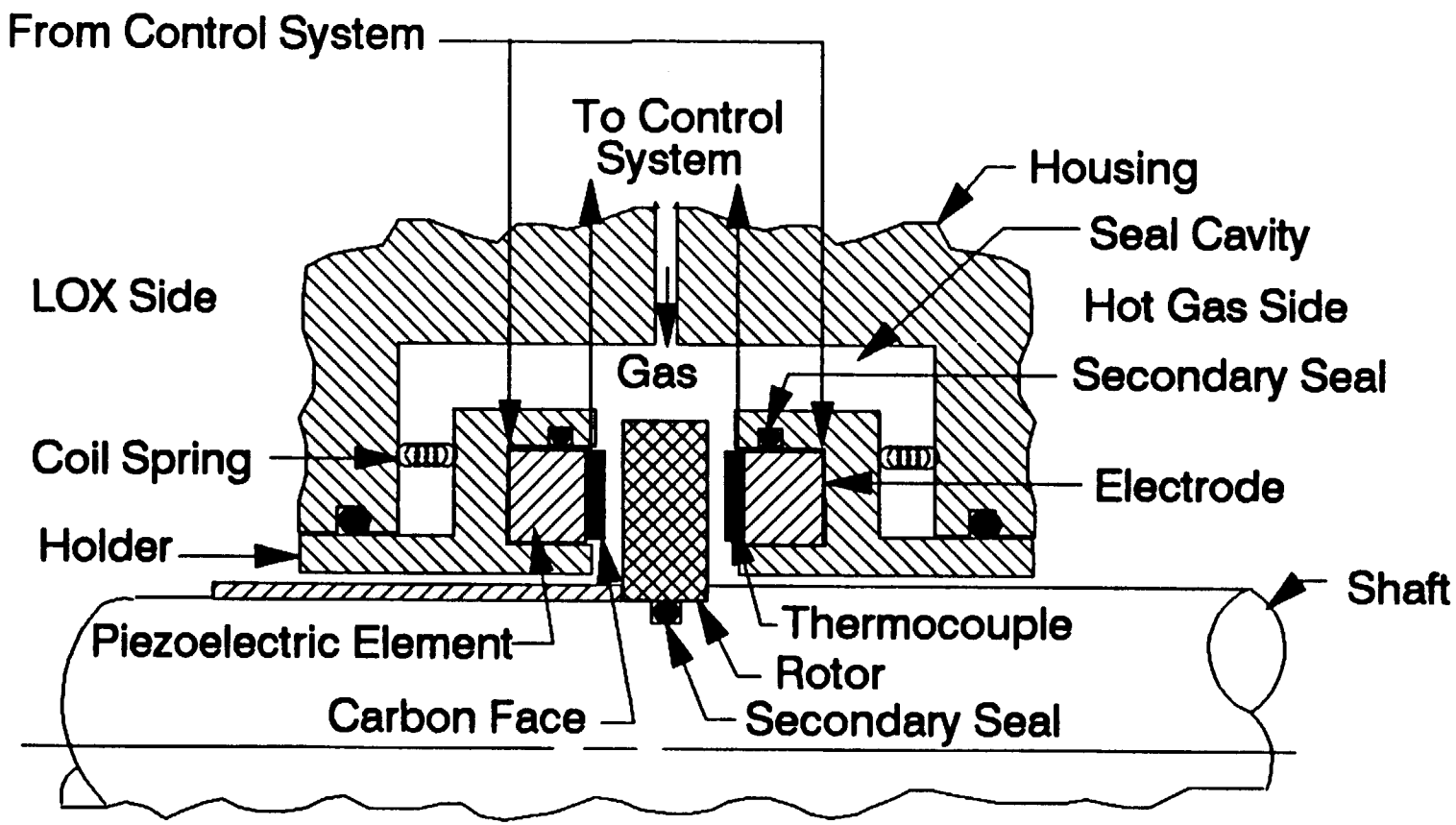

Figure 4-3. Schematic of Actively Controlled Mechanical Seal

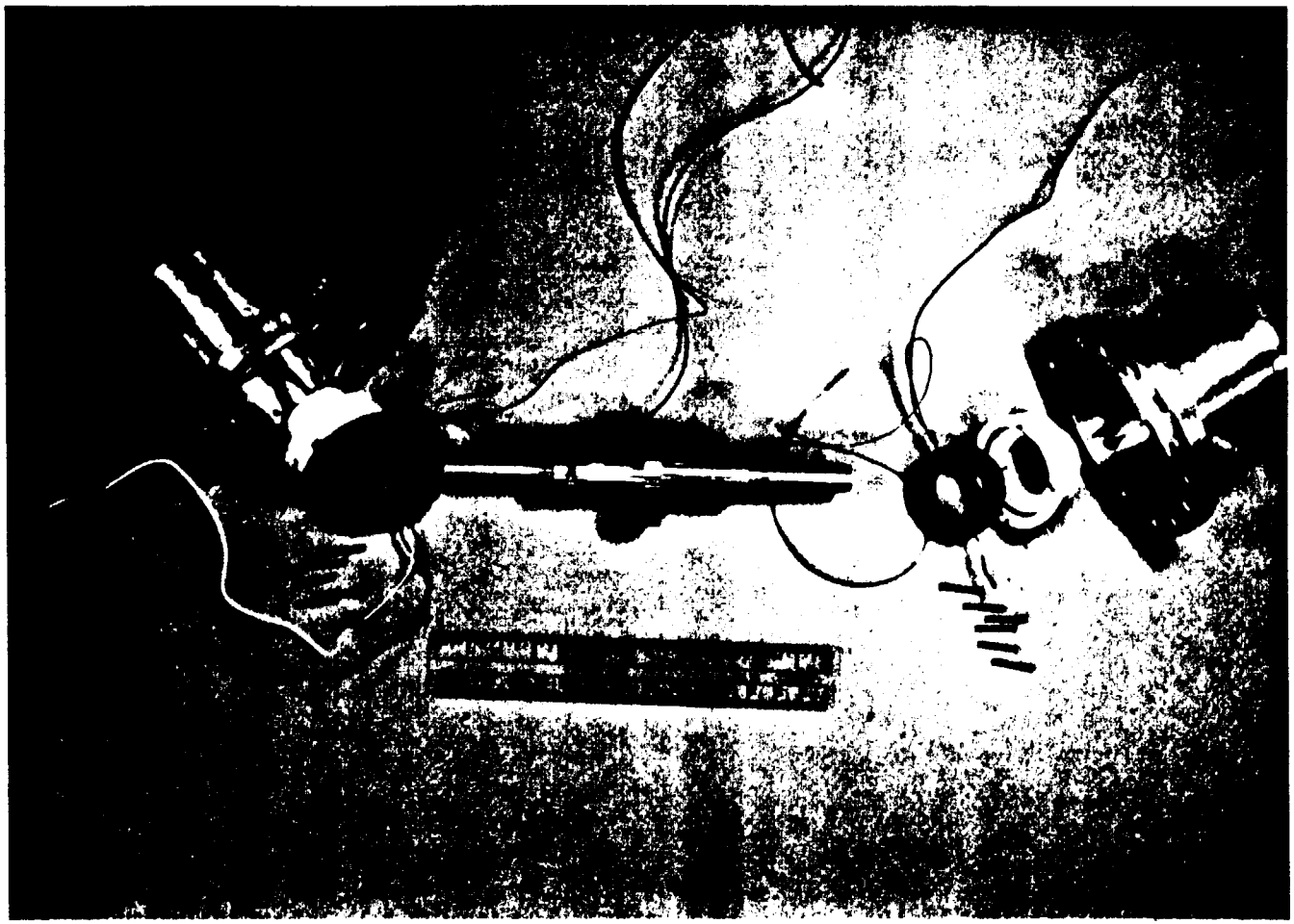

Figure 4-4. Photograph of Seal Components

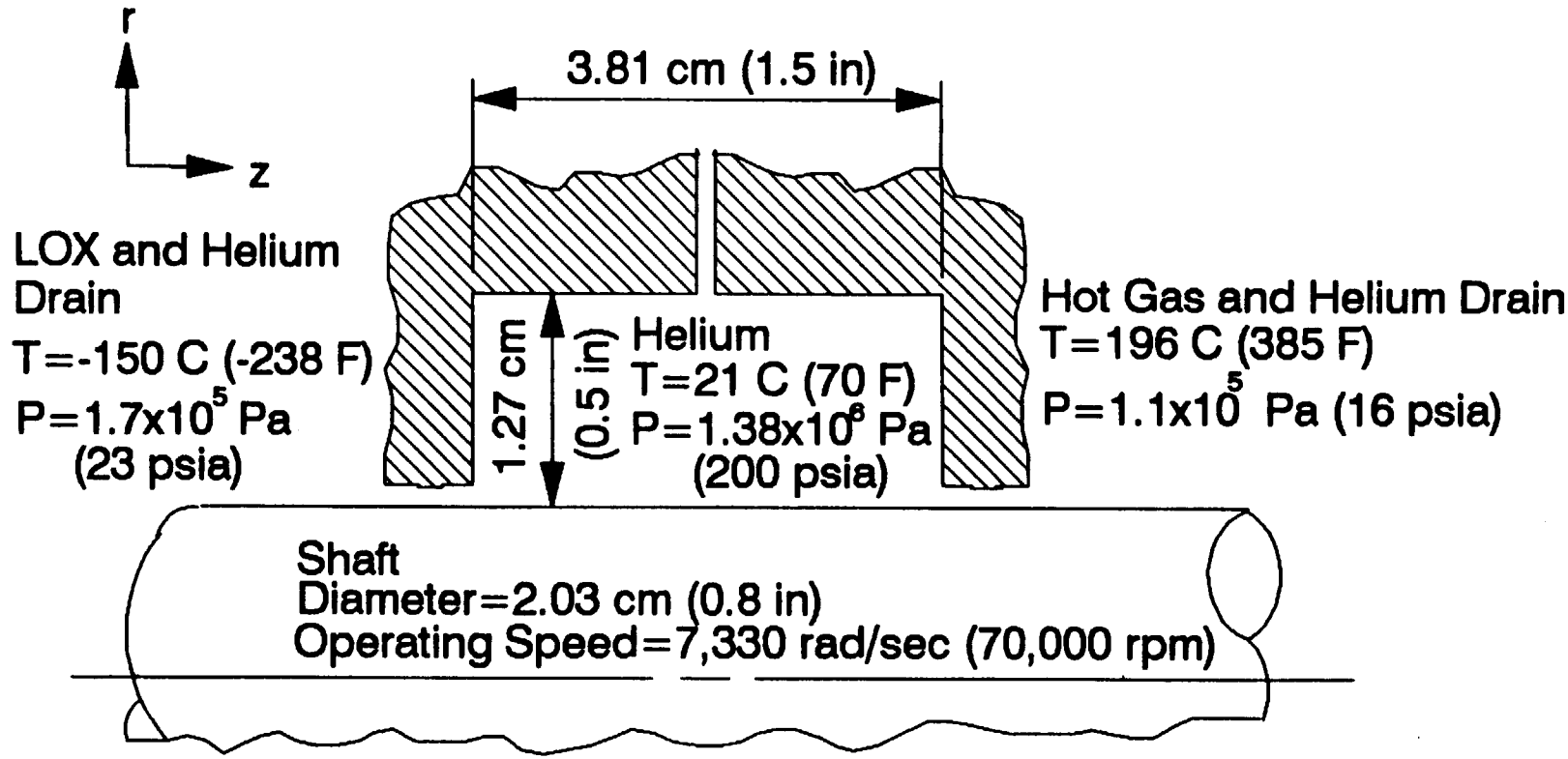

Figure 4-5. Sealing Envelope

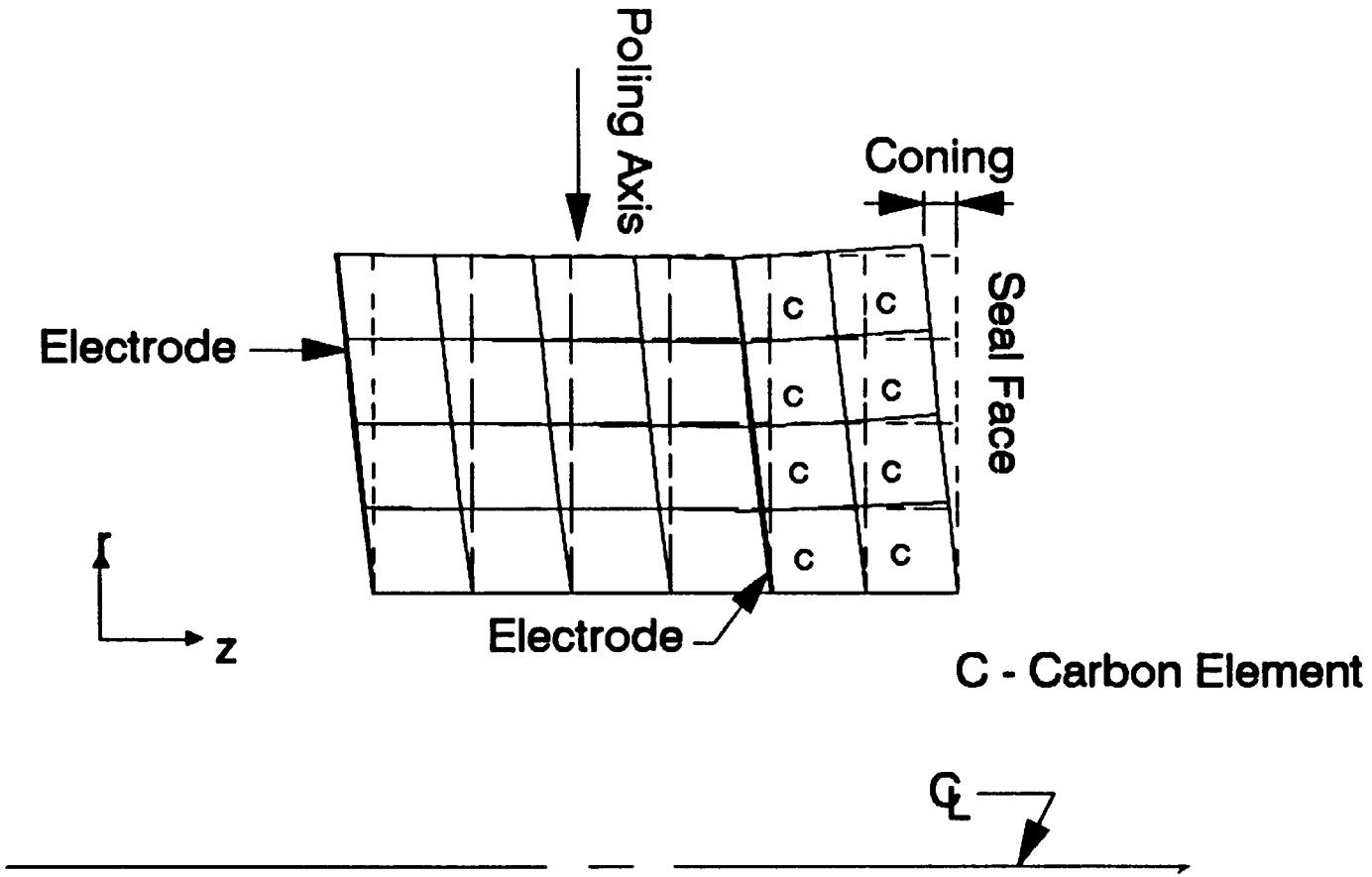

Figure 4-6. Shear Mode of Deformation

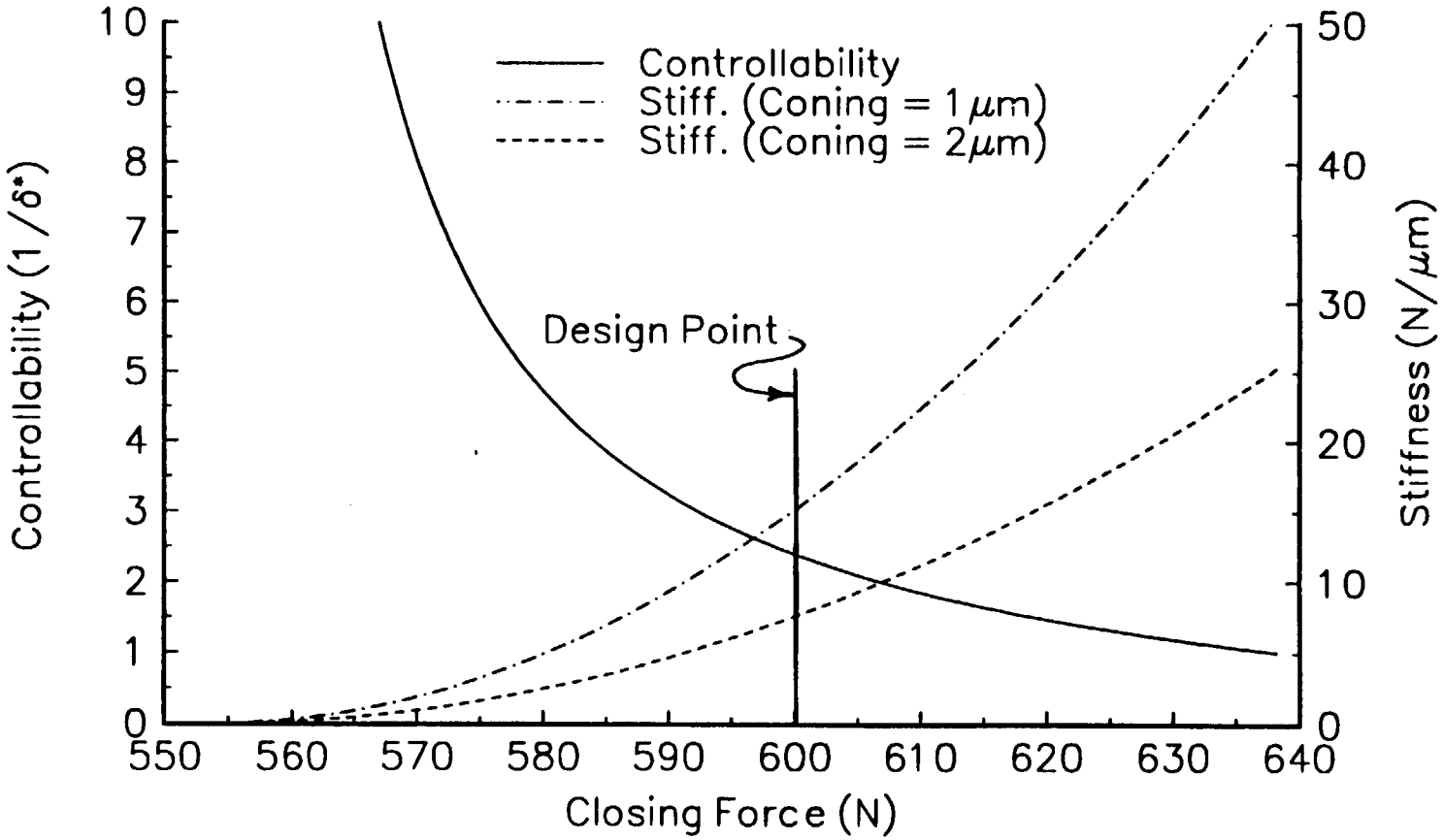

Figure 4-7. Dimensional Seal Design Curves for Helium Tests

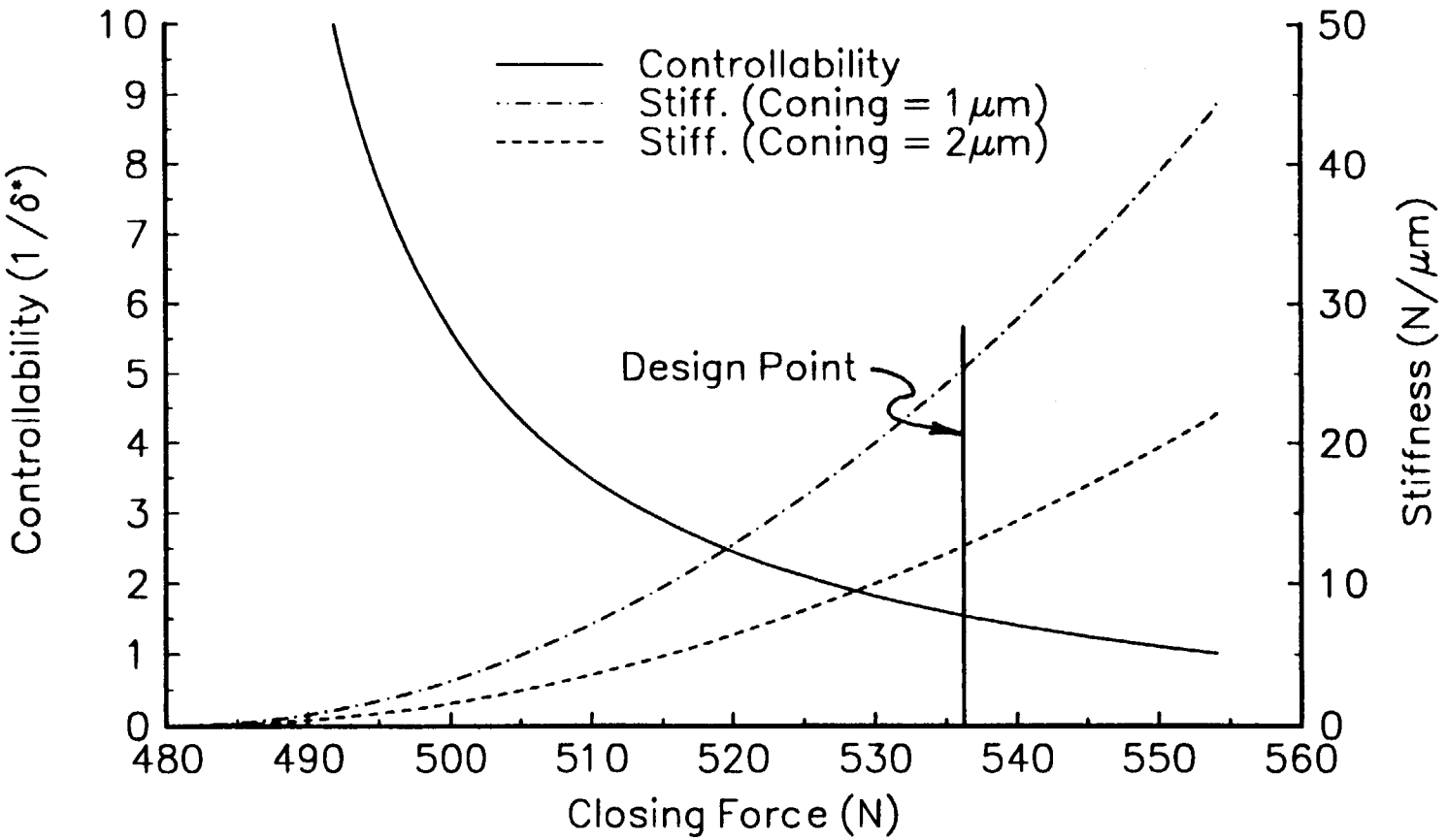

Figure 4-8. Dimensional Seal Design Curves for Air Tests

CHAPTER V

EXPERIMENTAL EQUIPMENT AND TEST PROCEDURES

The main objective for the seal tests was to demonstrate that an actively controlled mechanical seal is feasible for aerospace applications. A test rig was developed to partially simulate the operating environment in an actual liquid oxygen turbopump. This involved fabricating a seal housing with a sealing envelope similar to what is typically found in a liquid oxygen turbopump and to design the test rig such that it could be operated at relatively high rotational speeds. The severe temperatures actually found in a liquid oxygen turbopump were not simulated with this experimental setup.

Factors of primary importance that determine the performance of the seal are the leakage rate of the seal and the temperatures of the seal components, in relation to the voltage applied to the deformable face assembly. These were measured, as well as the parameters that determine the operating conditions of the turbopump: the sealed pressure and rotational speed of the shaft.

The tests that were performed included bench tests of the deformable face assembly, steady state tests, short term transient tests, and longer term transient tests. Since the seal control is based on controlling the coning with the deformable face assembly, bench tests were necessary to determine how well the coning could be varied with the deformable face assembly.

The steady state tests provided an initial demonstration that the leakage rate of the seal could be adjusted with the actively controlled seal while maintaining reasonable face

temperatures. In addition, the steady state test results can be compared to the predictions of the mathematical model that was previously developed [Wolff, 1991].

The transient tests were performed to demonstrate that the seal could be effectively operated with a closed-loop control system. This involved several steps, the first of which was evaluating whether the leakage rate of the seal or temperature was the more appropriate feedback signal. Another step was to determine the performance of the seal while it was subjected to various operating transients. The final transient testing involved operating the seal for an extended period of time to determine the longer term operating characteristics of the seal.

A schematic of the test setup is presented in Figure 5-1 and photographs of the setup are presented in Figures 5-2 and 5-3. Figure 5-2 presents the seal tester and the motor while Figure 5-3 presents the test setup. The test apparatus consisted of the actively controlled mechanical seal, the seal tester, the belt drive system, the motor and motor controller, the gas (helium or air) supply system, and the instrumentation. The latter consisted of a high voltage power supply, a flowmeter, a pressure gage, thermocouples and thermocouple readers, and a tachometer. Other instrumentation that is not shown in Figure 5-1 included an optical flat, a monochromatic light source, and a surface profilometer. The latter instrumentation was used to measure the coning of the deformable face assembly.

Experimental Equipment

Appendix A presents detailed design drawings of the seal tester utilized in these experiments. The housing of the seal tester was fabricated from aluminum while the shaft was made from O1 tool steel. Two ball bearings were utilized to support the shaft. These were deep groove, sealed ball bearings available from Barden Precision Bearings,

Danbury, Connecticut, part numbers 100FFTX1 and 101FFTX1. The limiting speed rating for these bearings is 6070 rad/sec (58,000 rpm).

For each of the two floating components, there were two pass throughs for the thermocouple wires, and for the wires attached to the electrodes on the piezoelectric transducers. These wire pass throughs were sealed with Swagelok union fittings, part number B-1000-6.

The motor that was utilized to drive the test rig was a one horsepower, variable speed universal motor. This motor is rated at a maximum speed of 1050 rad/sec (10,000 rpm) and is available from W. W. Grainger, Inc., Lincolnshire, Illinois, item number 2M191. The motor was controlled with a pulse width modulated motor controller that utilized the tachometer signal as the feedback (see Figure C-1).

The belt drive system consisted of two pulleys, an idler pulley, and a V-belt. The diameter ratio of the pulleys was 5 to 1 which provided a maximum speed capability for the test rig of 5240 rad/sec (50,000 rpm). An idler pulley was placed at the non tension side of the pulley to increase the contact angle between the belt and the pulleys.

The gas (either helium or air) was supplied to the test rig from a cylinder through 1/4 inch diameter copper tubing. The copper tubing was connected to the housing with a Swagelok male connector, part number B-403-1.

Instrumentation

A Trek (Medina, New York) model 610C high voltage power supply was used to drive the piezoelectric actuators. This instrument can be utilized as either a high voltage supply or amplifier with an output voltage range of -10 kV to +10 kV. The voltage applied to the piezoelectric transducer did not exceed ±3 kV, to prevent damaging the piezoelectrics. When used as an amplifier, the gain was set to 1000 V/V. The noise

specification for this instrument is 0.7 V RMS with a slew rate (a measure of the response time of the instrument) of 20 V/μs.

A flowmeter was located in the gas supply line to measure the leakage rate of the seal. The seal of this study is a double seal; therefore the flowmeter measures the leakage from two seals. Two different flowmeters were utilized, a rotameter, and an electronic mass flowmeter. A model FL-112 rotameter from Omega Engineering, Inc. was used for the steady state helium tests. This flowmeter has a range of 0-45 slm (0 - 1.59 scfm) for helium when a stainless steel ball is used, with an accuracy of ±2 percent of the reading and a repeatability of ± 1/2 percent of the reading. For the steady state air tests and the transient tests, an electronic mass flowmeter was used, model number FMA-874-V from Omega Engineering, Inc., Stamford, Connecticut. This flowmeter has a range of 0-100 slm (0 - 3.53 scfm) of air with an accuracy of ±2 percent of the full scale reading and a repeatability of ±0.2 percent of full scale. The response time of this flowmeter is 1.2 sec.

A pressure transducer was also installed in the gas flowline to measure the cavity pressure. For the steady state tests, the pressure was measured with a bourdon tube dial gage with a range of 1.01×10^5 - 2.86×10^6 Pa (0-400 psig), and an accuracy of ±2 percent of the reading. For the transient tests, the pressure was measured with an electronic pressure transducer, model number PX633-300G5V from Omega Engineering, Inc. This transducer can measure pressures up to 2.17×10^6 Pa (300 psig), with an accuracy of ±0.5 percent of the full scale reading. The response time of this transducer is 5 msec.

Three thermocouples were installed to measure the temperature of each seal face, and to measure the cavity temperature. These were type J, iron-constantan thermocouples with a wire diameter of 0.25 mm (0.010 in). Three DP116-JF1 thermocouple readers from Omega Engineering, Inc. were used for the thermocouple signal conditioners. These

have an accuracy of ±1.5 °C and provide an output signal of 1 mV/°C. This signal was conditioned with an OM5-IMV-100A voltage amplifier from Omega Engineering, Inc., which amplifies a signal of ±100 mV to ± 5 V with an accuracy of 0.05 percent. This voltage signal was then modified with a voltage divider such that the final calibration value for the thermocouple signals was 27.5 °C/V.

A small d.c. motor was used for the tachometer. The motor was an Archer, 1.5-4.5 V d.c. motor (available from Radio Shack) that was attached to the motor pulley with a shaft coupler. A 4.7 μF capacitor was placed in parallel on the output signal to filter out the a.c. component in the tachometer signal. The d.c. motor was calibrated with an optical tachometer, produced by Compact Instruments Limited of Hertfordshire, England. This optical tachometer has an accuracy of ± 1 rad/sec (±10 rpm).

The instrumentation was interfaced with a DAS-16, Keithley Metrabyte (Taunton, Massachusetts) data acquisition card that utilizes a 12 bit analog to digital converter. The card was configured to accept a -5 to +5 V input signal, with double ended input. This card was installed in a CompuAdd model A000, 386 personal computer. Labtech Notebook, Version 6 (Laboratory Technologies, Inc., Wilmington, Massachusetts) was utilized for the data acquisition software.

In the bench tests, the coning deformation was measured with a 2-inch diameter optical flat and a green monochromatic light source with a wavelength of 0.5461 μm (22 μin), obtained from Edmund Scientific, Barrington, New Jersey. With this light source, there is a surface height variation of 0.27 μm (11 μin) (relative to the optical flat) between adjacent fringes.

The surface profiles were measured with a surface profilometer produced by Hommelwerke, Model T20A (United States distributor is Valmet, Inc., New Britain, Connecticut). A stylus was used with a 5 μm (197 μin) tip radius.

Test Procedures

The first step to determine the coning deformation of a seal face was to polish the carbon such that it had a reflective finish. An optical flat was then placed on the carbon face (while it was removed from the housing) and illuminated with a monochromatic light source. This produced a fringe pattern. A voltage was then applied to the deformable face assembly, which resulted in a coning deformation. The coning deformation caused the fringe pattern to form into concentric rings. The coning deformation could then be measured by counting the number of concentric rings; the coning deformation from one fringe to the next was 0.27 μm (11 μin).

The surface profiles were measured with the surface profilometer over a travel length of 4.8 mm (0.19 in) at a travel speed of 0.5 mm/sec (0.02 in/sec). The analog voltage output of the surface profile was then downloaded to a data acquisition card that sampled the output at 400 Hz. This resulted in a trace that consisted of approximately 4000 points. The digitized traces were then leveled numerically.

The steady state tests were performed by manually adjusting the voltage applied to the deformable face assembly. The voltage was initially set to the maximum value, then decreased in 500 V steps to the minimum value, and then increased in 500 V steps back to the maximum value. Two sets of steady state tests were performed (with helium and air), that involved different test conditions and procedures.

The helium tests were the first successful set of tests that were performed. A rotameter was utilized to measure the leakage rate, and all data were recorded manually at one minute intervals. The data recorded included the leakage rate, the face temperature of each carbon face, the voltage applied to the deformable face assembly, the cavity temperature, the sealed pressure, and the rotational speed. The maximum voltage for

these tests was limited to 2000 V. Higher voltage levels produced leakage rates higher than the maximum flowrate the rotameter could measure. Each voltage level was held for four minutes. The balance ratio for these tests was 0.748.

A problem with electrical breakdown was encountered during the steady state helium tests. Initially the seal design provided no enclosure for the deformable face assembly at the inside radius. This design was based on the observation that no electrical breakdown occurred when high voltage levels were applied to the piezoelectric element in air. However, helium has a much lower dielectric strength than air, which resulted in electrical breakdown when the seal was operated in a helium atmosphere. Various attempts were made to insulate the piezoelectric element that included, using insulating grease, fabricating and installing bushings to cover the inside radius, and refabricating the holder and sealing the inside radius from the helium with O-rings. Each of these attempts was marginally successful, however voltage breakdown eventually reoccurred and a great deal of time was lost in attempting to electrically insulate the deformable face assembly. Therefore, the testing was continued with pressurized air, which was deemed acceptable to demonstrate the feasibility of an actively controlled gas seal.

Once air was utilized as the sealed gas, no further electrical breakdown problems occurred. However, at the higher rotational speeds dynamic instabilities occurred. This produced erratic leakage rates in concert with suddenly increased face temperatures, while the voltage was held constant. To address this problem, the balance ratio of the seal faces was increased from 0.748 to 0.766. This was a relatively straightforward modification to increase the axial stiffness with the higher balance ratio. However, dynamic instabilities at higher speeds were still encountered. This ultimately limited the maximum rotational speed of the test rig to 3770 rad/sec (36,000 rpm), whereas it was originally planned to operate the test rig at speeds up to 4190 rad/sec (40,000 rpm).

After the balance ratio was increased to 0.766, the steady state air tests were performed. An electronic flowmeter was installed, and each instrument (except for the pressure dial gage), was interfaced with a data acquisition card installed in a micro-computer. This enabled a much higher sampling rate of one Hz.

The electronic flowmeter could measure higher leakage rates than the rotameter. Therefore, the voltage range for the steady state air tests was from 3000 to 0 V. The voltage loading sequence was similar to the steady state helium tests, and the voltage was held constant at each point for one minute. The data recorded for these tests included the leakage rate, the voltage applied to the deformable face assembly, the face temperature of each carbon face, the cavity temperature, the sealed pressure, and the rotational speed.

The steady state tests demonstrated that the leakage rate could be controlled with the control system. The next step was to integrate the controllable seal in a closed-loop control system, and subject the seal to various operating transients while it was operated with an automatic controller. A commercially available proportional, integral, derivative (P.I.D.) controller available in LabTech Notebook was utilized for these tests The P.I.D. controller is defined by [Phillips and Harbor, 1988]

$$O(t) = K_P e(t) + K_I \int_0^t e(\tau)d\tau + K_D \frac{de(t)}{dt} \tag{42}$$

where

O(t) = output signal
e(t) = error (setpoint - feedback signal)
K_P = proportional constant
K_I = integral constant
K_D = derivative constant

The controller was tuned on a trial and error basis and the coefficients for the various tests are presented in a subsequent chapter (see Chapter VI - Results). Either the leakage rate or the face temperature of the seal provided the feedback for these tests. The output signal was a voltage which was fed to a high voltage amplifier with a gain of 1000. The amplified voltage was then used to drive the piezoelectric actuator.

All data were sampled at one Hz for these tests with the exception of the leakage rate during the tests in which leakage rate was utilized as the feedback. For these tests, the leakage rate was sampled at eight Hz, and the voltage applied to the controller was also updated at this rate.

The longer term transient tests typically consisted of eight, one-half hour cycles for a total test time of four hours. The leakage rate provided the feedback for these tests. During these tests the transients imposed on the seal included the step increases and decreases in pressure and speed, and a rapidly varying transient of pressure and speed. The ramp changes in pressure and speed were not included, because they were less severe than the step changes. Each half-hour cycle also included a startup and shutdown.

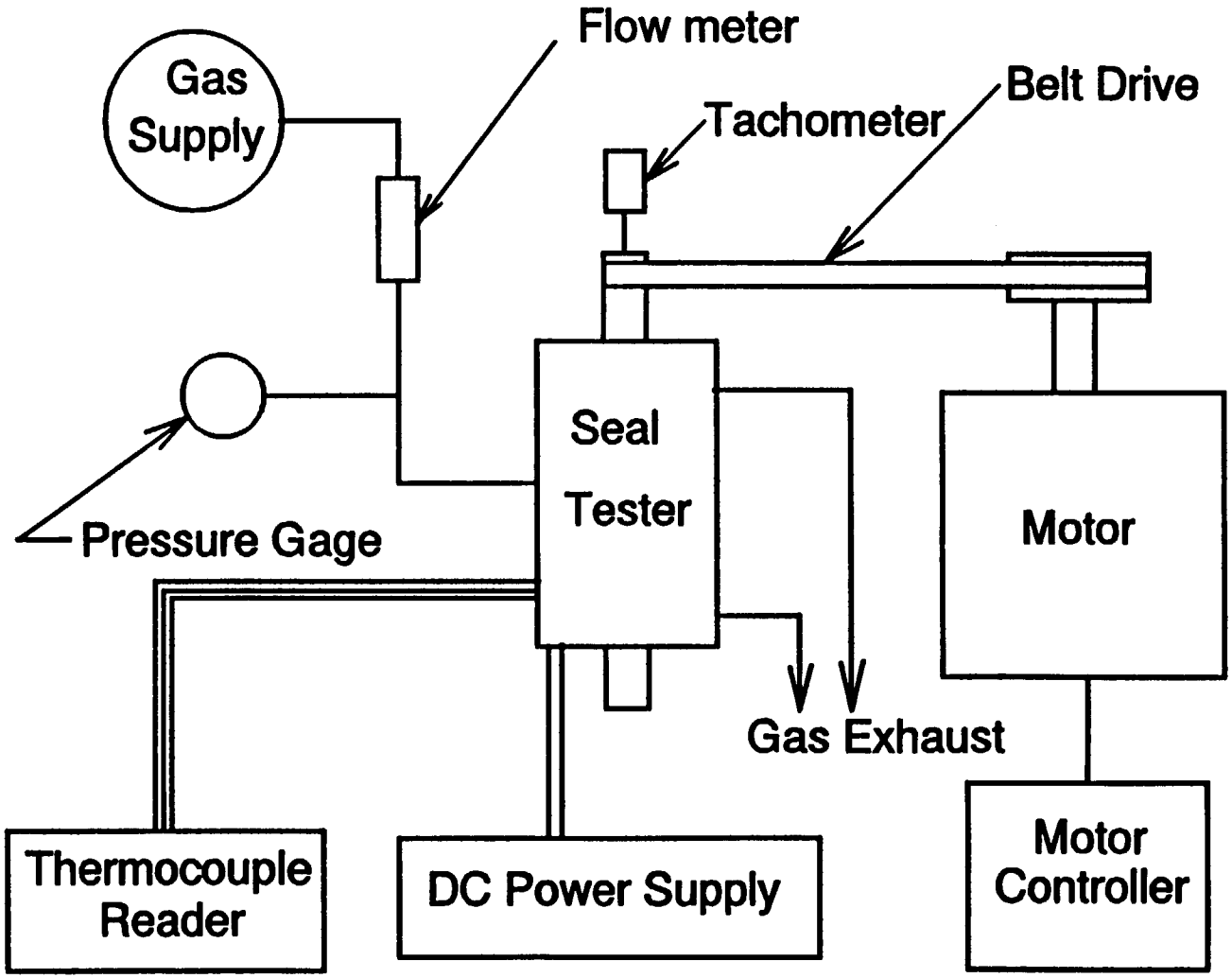

Figure 5-1. Schematic of Test Setup

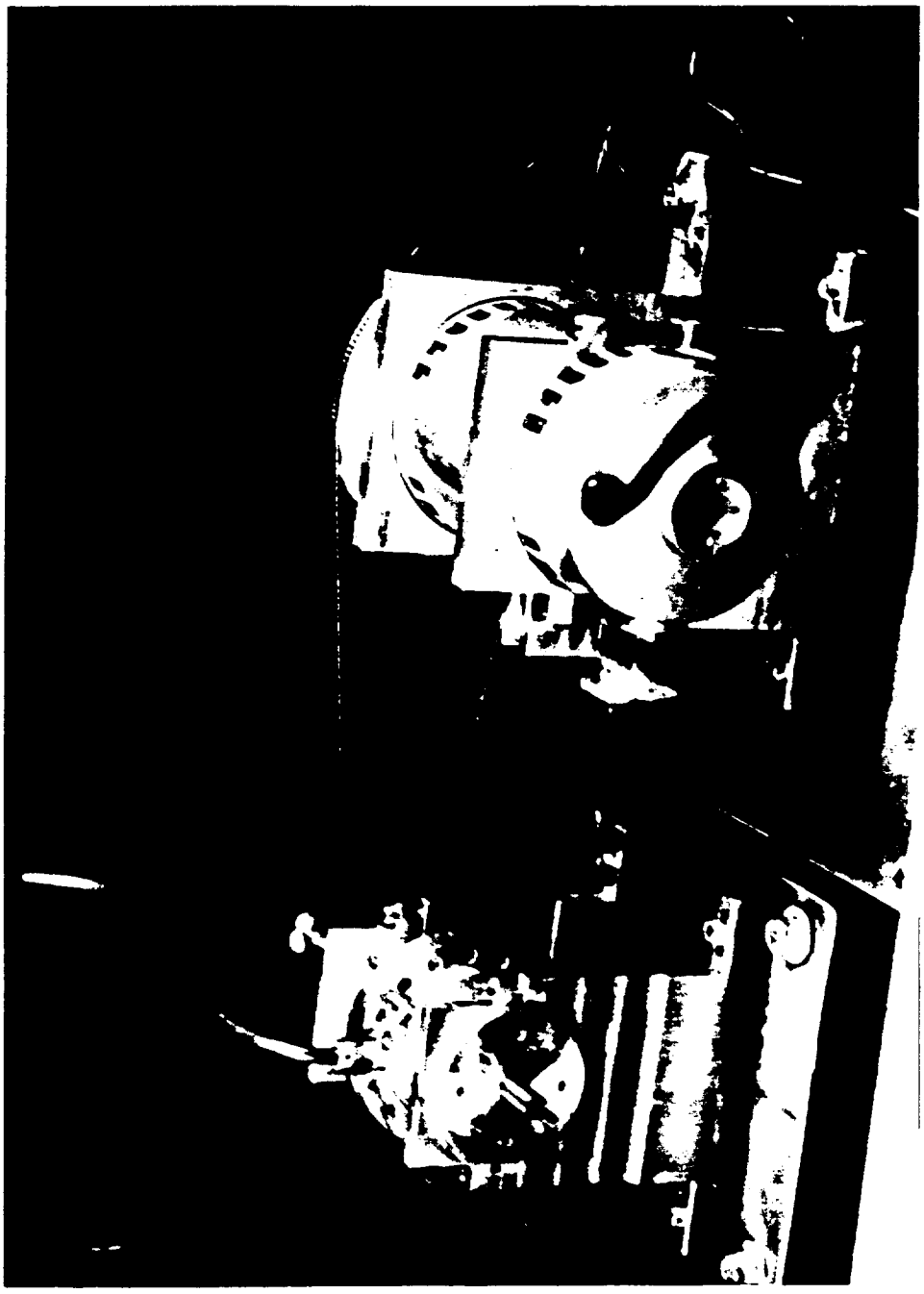

Figure 5-2. Photograph of Seal Tester and Motor

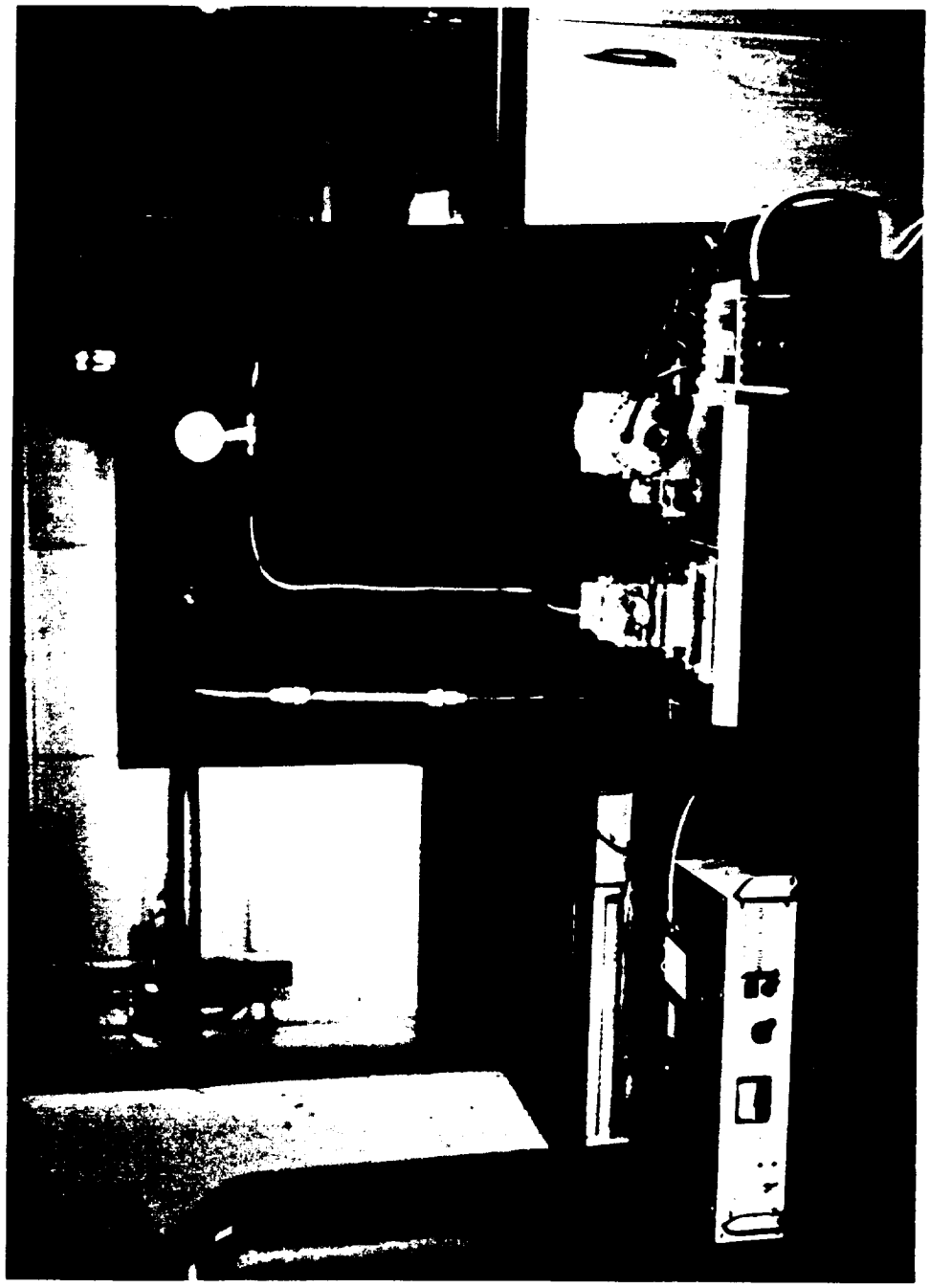

Figure 5-3. Photograph of Test Setup

CHAPTER VI

EXPERIMENTAL RESULTS

The experimental investigation of the actively controlled mechanical seal included three major tasks: bench testing of the deformable face assemblies to determine the range of coning they produce, steady state tests of the seal at various sealed pressures and rotational speeds, and transient tests of the seal with a closed-loop control system.

Bench Tests of Deformable Face Assemblies

The controllability of the seal is directly related to the range of coning that the deformable face assembly can produce; the larger the range of coning, the larger the range of film thickness that the seal can obtain. Figures 4-6 and A-2 present drawings of the deformable face assembly. The assembly utilized in these tests had the following radial dimensions: an outside diameter of 34.80 mm (1.370 in) with an inside diameter of 24.00 mm (0.945 in).

The coning was measured with a monochromatic light source and optical flat (see Chapter V - Experimental Equipment and Procedures). Figure 6-1 shows a plot of coning versus voltage for a typical deformable face assembly. The voltage was initially 3000 V and decreased in 500 V increments to a voltage level of -3000 V. The voltage was then increased in 500 V increments to a voltage of 3000 V. Figure 6-1 demonstrates that a range of coning from approximately 2 to -3.5 μm (79 to -138 μin) was produced by the deformable face assembly.

The coning deformation exhibited hysteresis over the voltage range applied to the deformable face assembly. The decreasing portion of the voltage loading path from 3000

to -3000 V exhibited a larger positive coning than the increasing portion from -3000 to 3000 V. At a voltage level of 0 V there was a difference in coning of 3 μm (118 μin) between the decreasing and increasing voltage loading paths.

Also presented in Figure 6-1 is a coning versus voltage plot in which the voltage range was limited to the range 0 to 3000 V. This plot exhibits much less hysteresis than the previous plot.

Figure 6-2 presents two coning versus voltage curves; one seal face was biased to produce a larger positive coning while the other curve is from a seal face that was biased to produce a larger negative coning. The coning can be biased in the positive direction by first applying a large negative voltage to the deformable face assembly. When the voltage load is removed, there will be some residual negative coning. The residual coning was observed to change slightly (less than a micron) over a period of several hours. Repolishing the seal face then removes the residual negative coning. This results in a deformable face assembly that produces a coning biased in the positive direction. In a similar manner, the coning can be biased in the negative direction by first applying a large positive voltage and then repeating the steps described above. Both curves present similar coning versus voltage characteristics with a 2 μm (79 μin) offset between them. This technique of biasing the coning can be utilized to produced a seal face with an initial positive or negative coning.

Steady State Tests

Several tests were performed to determine the steady state performance of the seal. The intent of these tests was to demonstrate that the leakage rate could be controlled by adjusting the voltage applied to the seal. The temperatures of the seal faces were also examined during these tests because high face temperatures can be an indication that the

faces are contacting, or conversely lower face temperatures could be an indication that there is a film between the seal faces.

During the steady state tests, the dependence of the leakage rate and face temperature were examined as functions of the following variables: the voltage applied to the piezoelectric actuator, the sealed pressure, and the rotational speed of the test rig. The temperature inside the seal cavity was also recorded during these tests.

Steady State Helium Tests

Figure 6-3 presents a plot of the leakage rate and voltage applied to the seal versus time. This test was performed at a sealed pressure of 1.48×10^6 Pa (200 psig) and a rotational speed of 3250 rad/sec (31,000 rpm). The seal was operated by initially applying a voltage of 2000 V. The voltage was decreased in 500 V increments to a minimum voltage level of 0 V and then increased in 500 V increments to a voltage of 2000 V. The seal was operated at each voltage level for three minutes.

Figure 6-3 demonstrates that the leakage rate can be varied over a significant range by varying the voltage applied to the seal. The leakage rate decreases (or increases) with each decrease (or increase) in voltage. Over the decreasing portion of the voltage curve, there is a decrease in leakage rate from 42 to 4 slm (1.48 to 0.14 scfm). At the lower leakage rates, the seal is less responsive to changes in applied voltage. Over the increasing portion of the voltage curve, the leakage rate increases from 4 to 46 slm (0.14 to 1.62 scfm).

Hysteresis is present in the leakage rate curve presented in Figure 6-3 and is generally present in each of the steady state tests. The leakage rate curve differs over the decreasing portion of the voltage load as compared to the increasing portion of the voltage load. The hysteresis could be produced by the hysteresis present in the coning deformation (see Figure 6-1) or by the response of the floating component of the seal. The second source

of hysteresis could arise from the o-rings located between the floating components and the seal housing.

Figures 6-4 and 6-5 present the effects of operating the seal at lower sealed pressures of 1.14 x 10^6 Pa (150 psig) and 7.91 x 10^5 Pa (100 psig), respectively. The rotational speed for these tests was again 3250 rad/sec (31,000 rpm). These figures demonstrate that the leakage rate of the seal can still be varied by controlling the voltages applied to the seal faces. For the test at 1.14 x 10^6 Pa (150 psig), the leakage rate varies between 28 and 3 slm (0.99 to 0.11 scfm) for voltages between 2000 and 0 V. This range of leakage rates is reduced compared to the previous test for the same voltage range. This reduced leakage rates at lower pressures is a result of thinner films between the seal faces, and less pressure to drive the seal leakage.

For the seal test performed at 7.91 x 10^5 Pa (100 psig) the leakage rate varies between 7 and 1 slm (0.25 to .03 scfm) for voltages between 2000 and 0 V. The ranges of leakage rates that can be obtained is seen to further decrease as the sealed pressure is decreased.

Figures 6-6 and 6-7 present the effects of operating the seal at rotational speeds of 2720 rad/sec (26,000 rpm) and 3665 rad/sec (35,000 rpm). The sealed pressure for these tests was 1.48 x 10^6 Pa (200 psig). The performance of the seal at these reduced speeds is similar to the performance demonstrated in Figure 6-3. The range of leakage rates obtained from the seal are similar; the maximum leakage rate is in the range of 40 to 50 slm (1.41 to 1.77 scfm) whereas the minimum leakage rate is in the range of 2 to 4 slm (.07 to 0.14 scfm)..

Figure 6-8 presents the temperatures of the seal faces and the cavity temperature for a sealed pressure of 1.48 x 10^6 Pa, and a rotational speed of 3665 rad/sec (35,000 rpm). This figure demonstrates that the temperature increases as the leakage rate of the seal

decreases. This is expected, since the film thickness between the seal faces is lower at the lower leakage rates, which increases the viscous heat generation produced by the interface between the rotating and nonrotating seal faces. During the increasing portion of the temperature curve, the temperature of the seal faces steadily increases from 40 to 65 °C. At the point of minimum leakage rate, the seal has not yet reached a steady state condition, and the temperature continues to increase even though the leakage rate has increased slightly. Therefore, there is a three minute time lag between the point of minimum film thickness and maximum face and cavity temperature. However, over the decreasing portion of the temperature curve, the face temperature decreases in a stepwise manner with each step increase in leakage rate.

Figure 6-8 demonstrates that face temperature can be used as an indication of leakage rate, and therefore film thickness, once the face temperature has reached a steady state condition. Thus, the face temperature could provide the feedback to an active control system. Based on studies performed with other actively controlled seals [Salant et. al., 1987], it had been expected that the temperature difference between the face temperature and cavity temperature could provide a better indication of film thickness and leakage rate. Figure 6-9 presents such a plot of the temperature difference (face temperature minus the cavity temperature) versus the leakage rate of the seal for the same conditions as the previous plot. The relationship between temperature difference and leakage rate is not as clear as compared to face temperature versus leakage rate. Therefore, for the transient seal tests, the temperature difference was not used as a feedback signal.

Steady State Air Tests

Steady state tests were also performed with air as the sealed gas. During these tests, the leakage rate and seal face temperature were again examined as functions of the voltage applied to the piezoelectric actuator, the sealed pressure, and the rotational speed of the test rig. These tests were performed by initially applying a voltage level of 3000 V. The voltage was then decreased in 500 V increments to 0 V and then increased in 500 V increments to 3000 V. The seal was operated at each voltage level for 1 minute.

Figure 6-10 presents the test results for a sealed pressure of 1.34×10^6 Pa (180 psig) at a speed of 3770 rad/sec (36,000 rpm). This figure again demonstrates that the leakage rate can be varied over a considerable range by controlling the voltage applied to the seal. With each step change in voltage there is a corresponding change in leakage rate. As the voltage is decreased from 3000 to 0 V, the leakage rate decreases from 17 to 4 slm (0.60 to 0.14 scfm). As the voltage is increased from 0 to 3000 V, the leakage rate increases from 4 to 19 slm (0.14 to 0.67 scfm). Hysteresis can again be seen in the seal response. Over the decreasing portion of the voltage curve, the leakage rate is generally higher than the leakage rate over the increasing portion of the voltage curve, for identical voltage levels.

Figure 6-11 presents the effects of operating the seal at a reduced pressure of 6.48×10^5 Pa (80 psig). The operating speed for this test was the same as the previous test, 3770 rad/sec (36,000 rpm). This figure demonstrates that the leakage can still be varied by controlling the voltage applied to the seal. However, the range of leakage rates is considerably reduced as compared to the previous test. The leakage rate varied between 8 and 2 slm (0.28 and .07 scfm) as the voltage was varied between 3000 and 0 V.

Figures 6-12, and 6-13 present the effects of the operating the seal at rotational speeds of 3140 and 2830 rad/sec (30,000 and 27,000 rpm), respectively. The sealed

pressure for these tests was 1.34 x 10^6 Pa (180 psig). The leakage rate can be adjusted at each speed by controlling the voltage applied to the seal. For the test at 3140 rad/sec, the leakage rate varied between 12 and 3 slm (0.42 and 0.11 scfm). For the test at 2830 rad/sec, the leakage rate varied between 9 and 4 slm (0.32 and 0.14 scfm). The range of the leakage rates is reduced as the speed is decreased. This could be a result of thermal effects or it could also be due to misalignment between the seal faces which produces a hydrodynamic effect.

Figure 6-14 presents the seal face temperature, cavity temperature, and leakage rate versus time for a sealed pressure of 1.34x10^6 Pa (180 psig) and a speed of 3770 rad/sec 36,000 rpm). The face and cavity temperature increase as the leakage rate decreases, and conversely the face temperature decreases as the leakage rate increases. The face temperature reaches a maximum of 103 °C while the cavity temperature reaches a maximum of 65 °C. At each step change in leakage rate there is a sudden change in the slope of both the face and cavity temperature curves. However, this trend is more obvious in the cavity temperature curve. A comparison of the cavity temperature for the helium test to the cavity temperature for the air test indicates that cavity temperature for the latter test is more responsive to changes in the leakage rate. This is due to the placement of the thermocouple. For the air tests, the thermocouple was located directly in front of the gas inlet, whereas for the helium tests it was located further away from the gas inlet.

A comparison of the helium and air tests indicates that the seal can operate successfully with either gas. The leakage rate is seen to vary considerably as the voltage is changed. Both tests also demonstrate that the controllability of the seal degrades as the sealed pressure decreases. For both tests, the leakage rate generally increases as the speed increases. This trend is partly due to the increased viscous heat generation, which increases the thermally induced coning deformations. The increased leakage rate with

speed could also be an indication that there is a hydrodynamic load support present. This could be produced by misalignment between the seal faces.

The leakage rate is seen to be generally higher for the helium tests as compared to the air tests. This is partly due to the reduced balance ratio for the helium tests, which produces a higher seal controllability. In addition, the air tests were performed at a slightly reduced pressure. This was due to a faulty pressure transducer, which was not detected until after the air tests were performed.

Transient Tests

The intent of the transient tests was to determine the seal performance when subjected to transient conditions while being operated with a simple closed-loop control system. Two different signals were examined as feedback to the control system: the leakage rate and the temperature of one of the seal faces. A commercial proportional, integral, derivative control system was used for these tests (see Chapter IV -Experimental Equipment and Procedures). The performance objective for these tests was to maintain the setpoint of the controlled parameter. In addition, the control systems were evaluated based on their effectiveness in limiting leakage while preventing excessive face temperature.

Transient tests were performed for two different time periods. The time period for the short term tests was approximately one half hour, while that for the longer term tests was four hours.

Short Term Transient Tests

Figure 6-15 presents the pressure and speed transients imposed on the seal during the short term tests. The seal was started and operated for approximately three minutes with a cavity pressure of 1.48×10^6 Pa (200 psig) and a rotational speed of 3770 rad/sec

(36,000 rpm). The following operating transients were then imposed on the seal: a ramp decrease followed by a ramp increase in both speed and pressure and a step decrease followed by a step increase in both speed and pressure. The speed of the shaft was varied between 3770 and 2000 rad/sec (36,000 and 19,000 rpm) while the pressure was varied between 1.48×10^6 and 4.46×10^5 Pa (200 and 50 psig). During the speed transients, the pressure was held constant at 1.48×10^6 Pa, and during the pressure transients, the speed was held constant at 3770 rad/sec.

Figure 6-16 presents the leakage rate and temperature of the seal faces versus time for the test that used the leakage rate as the feedback from the seal. The three coefficients (K_P, K_I, and K_D) of the P.I.D. controller were set to 0.1 V/slm, 0.2 V/(slm sec), and 0.01 (V sec)/slm, respectively. The sampling rate for the flow rate was 8 Hz, which was also the rate at which the voltage to the seal is updated. All other data were sampled at 1 Hz.

Figure 6-16 demonstrates that the control system can maintain the setpoint leakage rate of 12 slm (0.42 scfm). The maximum deviation in the setpoint occurs during the stepwise pressure transients. At the lower cavity pressure, the leakage rate deviates more from the setpoint than at the higher cavity pressures. This trend was generally observed in the seal tests; at lower pressures the leakage rate of the seal oscillated. (During some seal tests at higher speeds, these oscillations became much larger and severely affected the performance of the seal - see discussion of instability below.) By maintaining the leakage rate at a constant value, the temperature of the seal faces is also limited. During this test the maximum seal face temperature was 81 °C. This is as expected; a set leakage rate of the seal ensures that there is a lubricating film between the seal faces, which prevents the seal faces from contacting and becoming too hot.

Figure 6-17 presents the voltage applied to the seal by the control system, versus time for this test. This figure clearly demonstrates that the control system was very active.

The voltage range that was available to the controller during this test was 0 to 3000 V and Figure 6-17 demonstrates that the full range was utilized.

Figure 6-17 demonstrates that as the transients in rotational speed were imposed on the seal, the voltage applied to the seal changed at the same time. This could be an indication that there was a hydrodynamic load support, produced by slight misalignment between the seal faces.

The voltage in Figure 6-17 increases as the pressure decreases (see Figure 6-16). This is as expected; as the pressure decreases, the film thickness must increase to maintain a constant flow rate.

Figure 6-18 presents the leakage rate and temperature of the seal faces versus time for the control system with temperature of a seal face as the feedback. The transients imposed during this test were identical to the transients imposed in the test that utilized leakage rate as the feedback signal (see Figure 6-15). The data presented in this figure begins once the seal face temperature was close to the setpoint of 80 °C. The voltage applied to the seal was controlled manually up to this point. The three coefficients (K_P, K_I, and K_D) of the P.I.D. controller were set to -0.5 V/°C, -0.1 V/(°C sec), and -0.5 (V sec)/°C, respectively. All data were sampled at 1 Hz for this test, and the voltage to the control system was also updated at this rate.

The setpoint temperature of 80 °C is maintained closely during this test. Maximum deviations from the setpoint occurred during the stepwise changes in pressure. However, these deviations were less than 3 °C. The leakage rate varied from 2 to 16 slm (.07 to 0.57 scfm) during this test with larger spikes occurring as the pressure transients occurred. The wide variation in leakage rates points out a disadvantage of utilizing temperature as the feedback signal to the control system. During transients when the face temperature decreases rapidly, the control system dramatically reduces the leakage rate to prevent a

decrease in face temperature. Face contact and wear of the seal faces, is likely to occur at this point. An additional disadvantage of this control system is that with the basic P.I.D. controller, the controller must be operated manually until the face temperature nears the setpoint. Otherwise, the controller will set the voltage at the minimum level to bring the face temperature to its setpoint rapidly, which could promote face contact.

Figure 6-19 presents the voltage applied to the controller during this test. The voltage varied from 0 to 3000 volts which indicates that the control system was very active. The voltage decreased as the rotational speed decreased which is opposite to what occurred when leakage rate was utilized as the feedback signal. This is explained by considering the viscous heat generation between the seal faces. The viscous heat generation is proportional to the rotational speed of the shaft, therefore for a constant voltage level and film thickness, the temperature of the seal faces decrease as the speed is decreased. A decrease in voltage then decreases the film thickness to maintain a constant face temperature. The voltage during this test, increased as the pressure decreased (see Figure 6-15 for pressure trace) which is what also occurred in the previous test. The lower pressures produce a smaller film thickness, for a constant coning. This produces a larger viscous heat generation and the control system must then increase the voltage to maintain a constant temperature of the seal face.

Figure 6-20 presents the results of increasing the setpoint temperature. This test was similar to the test in which the temperature of a seal face provided the feedback to the control system except that the setpoint was increased to 95 °C. The leakage rate remained at approximately 5 slm (.18 scfm) for a large portion of the test which is significantly lower than the leakage rate from the previous test. The leakage rate can be decreased at the expense of allowing the seal to operate at higher temperatures.

Long Term Transient Tests

The short term transient tests demonstrated that the leakage rate and temperature of the seal faces could be controlled in a closed-loop system. The intent of the long term transient tests was to determine the operating characteristics of the seal for a longer period of time while operated with a basic P.I.D. controller. The three coefficients (K_P, K_I, and K_D) of the P.I.D. controller were set to 0.3 V/slm, 0.2 V/(slm sec), and 0 (V sec)/slm, respectively.

Figure 6-21 presents the transients imposed on the seal during these tests. The time period for each cycle was one-half hour and the cycle was repeated nine times for a total test time of four and one-half hours. These transients included a step decrease and then increase in both pressure and rotational speed as well as a startup and shutdown at the beginning and end of each cycle. During the pressure transient, the speed was held constant at the nominal rotational speed, and during the speed transients the pressure was held constant at 1.48×10^6 Pa (200 psig). During the seal shutdown at the end of each cycle, the air flow line was closed and the seal was stopped. The nominal rotational speed for this test was 2600 rad/sec (25,000 rpm).

Oscillating type transients were also imposed on the operation of the seal during the long term tests, in which either the pressure or the speed were rapidly varied between the maximum and minimum values. The maximum and minimum pressure values were 1.48×10^6 Pa (200 psig) and 7.90×10^5 Pa (100 psig), respectively while the maximum and minimum rotational speeds were 3250 to 1500 rad/sec (31,000 to 15,000 rpm), respectively. The step changes in operating conditions presented a more severe transient condition than the ramp changes; therefore, the latter were not included during the long term transient tests. The feedback for the long term transient tests was the leakage rate of

the seal, since short term transient tests demonstrated the disadvantages of utilizing face temperature as the feedback signal.

Figure 6-22 presents the leakage rate and face temperature versus time for a long term transient test. The setpoint for this test was 12 slm (0.42 scfm). The leakage rate tracked the setpoint during each cycle while the face temperature was limited to a maximum value of 85 °C. This indicates that the seal operated successfully during the long term test.

Figure 6-23 presents a typical 30 minute operating cycle for this test. The largest deviations between the setpoint and operating value occurred during rapid variations in pressure (see Figure 6-21 for pressure trace). Such spikes in leakage rate do not represent a serious problem with the operation of the seal. The deviations endured for a very short time period and do not represent a large loss of air. The minimum deviations do not represent a significant wear problem. The face temperature did not increase significantly during this time period and surface analyses of the seal faces after the long term tests demonstrated that no discernible wear occurred (see Surface Analysis of Seal Faces below).

Figures 6-24 presents the voltage applied to the seal and the cavity pressure during a 30 minute cycle for this test. The voltage followed the same trends as occurred in the short term transient test; the voltage increased as the pressure decreased, and conversely the voltage decreased as the pressure increased.

Figure 6-25 presents the voltage applied to the seal and the rotor speed versus time during the same 30 minute cycle for this test. The voltage changes occurred simultaneous with the speed changes, as can be seen when the rapidly varying speed transients were applied to the seal. The voltage changes occurred in phase with the speed changes. This is most likely an indication that a hydrodynamic load support mechanism was present. If

these voltage changes were the result of thermal deformations, it is likely there would have been a phase lag between the voltage changes and speed transients.

Figure 6-26 present the transients imposed on a seal during a second long term transient test. The operating cycles were similar to the previous test except that the nominal rotational speed was increased to 3200 rad/sec (30,500 rpm). .

Figure 6-27 presents the leakage rate and face temperature versus time for this long term transient test. The leakage rate tracked the setpoint of 10 slm (0.35 scfm) during each cycle while the face temperature of the seal reached a maximum of 76 °C. This indicates that the seal operated successfully during this test at the higher rotational speed.

Figure 6-28 presents a typical 30 minute operating cycle for this test. The largest deviations in the leakage rate occurred as the pressure was varied rapidly. A comparison of the two long term tests reveals that the leakage rate oscillated more during low pressure operation at the higher rotational speed as compared to low pressure operation at the lower rotational speed. This trend was generally observed, that the oscillations in the leakage rate increased as the rotational speed was increased, and as the cavity pressure was decreased.

A comparison of the two long term tests also reveals that the face temperature of the seal was lower during the second long term test as compared to the first long term test. This is surprising, because the setpoint for the leakage rate was lower for the second test and the nominal rotational speed was higher. Both of these factors should produce a higher face temperature. These trends are probably due to fabrication and installation tolerances of the seal faces. Between the long term tests, the seal was disassembled, the faces were polished, and the seal was reassembled. This could have changed the runout in the seal faces between the long term tests. This difference in runout could have led to the lower face temperature at the lower leakage rate and higher rotational speed. This clearly

indicates that minimizing fabrication and assembly tolerances is important for higher speed mechanical seals.

Figure 6-29 presents a test in which the operation of a conventional seal was simulated. The coning was biased in the positive direction to establish a lubricating film between the seal faces. The coning was measured at 0 volts to be approximately 1.7 μm (66 μin) for both seal faces. The nominal speed for this test was 3200 rad/sec (30,500 rpm). The transients imposed during this test were identical to the ones presented in Figure 6-26. The voltage level was 0 V throughout the test.

This test demonstrates that the seal performs poorly without the control system. During the first cycle, the face temperature reached a temperature of 110 °C. During the second cycle, the temperature of the seal faces increased dramatically after the step increase in pressure. The test was then aborted to prevent damage to the seal components.

Constant Voltage, Long Term Tests

It is well known for hydrostatic face seals that if the seal faces are coned in the positive direction a lubricating film will exist between the seal faces. Therefore, a very simple control system would operate the seal with a constant positive voltage, large enough to ensure that the seal faces have positive coning. However, during startup and shutdown, increasing the voltage could prevent face contact produced by transient operating conditions.

Two tests were performed with constant voltage levels of 2000 V and 1000 V. The transients imposed on the seal were similar to the transients imposed during the previous tests with a few slight differences. The nominal cavity pressure was 1.48×10^6 Pa (200 psig) which was decreased to 4.46×10^5 Pa (50 psig) during the stepwise pressure

transients. The nominal rotational speed for these tests was 3660 rad/sec (35,000 rpm) with the stepwise decrease down to 2100 rad/sec (20,000 rpm).

Figure 6-30 presents the leakage rate and face temperature versus time for a 4 hour test in which the voltage level was set to 2000 V. The leakage rate remained less than 10 slm (0.35 scfm) during the entire test except when the pressure transients were imposed on the seal. At the times when the pressure was suddenly changed, spikes in the leakage rate occurred. The temperature of the seal face remained below 90 °C over the entire test. This test demonstrates that a simple control system that ensures a positive coning of the seal faces may be adequate to limit the face temperature while preventing excessive leakage.

Figure 6-31 presents an additional 4 hour test in which the voltage level was maintained at 1000 V. However, during startup of the seal, the voltage was increased to approximately 2500 V to promote a larger film thickness. This minimized the torque required by the motor that drove the test rig to start the seal, and it also prevented the wear that might have occurred due to startup transients. The transients imposed on the seal were identical to the previous 4 hour test with a constant voltage of 2000 V.

Figure 6-31 demonstrates that the leakage rate was decreased during this test at the expense of higher face temperatures. The leakage rate was generally less than 5 slm (0.18 scfm) during the entire test. The maximum face temperature reached as high as 110 °C. The surface profiles of the seal faces were measured after these tests and they indicated that very little wear had occurred (see discussion of wear below).

Surface Analysis of Seal Faces

The seal design in this study is based on the assumption that the faces of the seal are not in contact. Surface analyses of the seal faces were performed to evaluate this assumption. The surface analyses consisted of performing a measurement with a surface

profilometer immediately after polishing the seal faces, and after the seals had been utilized in a test. The surfaces of both the carbon and tungsten carbide faces were measured. A comparison of these measurements was used to evaluate the noncontacting assumption.

Figure 6-32 presents four typical surface profiles obtained from a carbon face. These traces have been leveled and an offset has been introduced for ease of comparison on one plot. Otherwise, no additional numerical manipulations of the traces have been performed. The profiles include that of a freshly lapped face, one after a long term transient test presented in Figure 6-27, one after a short term test with no control as presented in Figure 6-29, and one after 8 hours of operation with constant voltage levels as presented in Figures 6-30 and 6-31. These profiles indicate that almost no degradation in the surface finish occurred between the tests.

It is somewhat unexpected that the short term test with no control resulted in no degradation of the seal faces. The temperature of the carbon face was as high as 120 °C during this test which could have been an indication that the faces were contacting. However, the test was aborted at this point to prevent damage to the seal components. Extended operation at this condition could have degraded the surface finish of the seal faces.

Figure 6-33 presents three typical surface profiles obtained from the tungsten carbide rotor. These profiles have been leveled and an offset has been introduced between them for the sake of comparison. The profiles include that of a freshly lapped face, one after the 4 hour test with control (see Figure 6-27), and one after the short term test with no control (see Figure 6-29). These measurements indicate that no degradation in the surface finish of the tungsten carbide face has occurred during these seal tests.

Both the carbon surface profiles and the tungsten carbide profiles indicate that no discernible differences were present in the surface finish of the seal faces before and after

testing. This could be an indication that the seal faces were not contacting and wearing during these tests. Longer term seal tests could provide additional insight to determine whether no wear is occurring and that the noncontacting assumption is valid.

Some Observations of Seal Instabilities

Fabrication and assembly tolerances always lead to a certain amount of runout between the seal faces, which can adversely affect the performance of the seal. Such effects were observed during the experimental testing of this seal.

Figure 6-34 presents a short term test in which sudden increases in leakage rate occurred simultaneously with an increase in face temperature. Such a condition will be subsequently referred to as a seal instability. This condition could indicate that the lubricating film varies a great deal circumferentially. This could lead to an excessive film thickness at certain cirumferential points while contacting at others. The excessive film thickness would promote increased seal leakage while the face contact would lead to higher face temperatures.

The test presented in Figure 6-34 began with a rotational speed of 3660 rad/sec (35,000 rpm) and a cavity pressure of 1.48×10^6 Pa (200 psig). The voltage was initially set to 2700 V for startup and then held constant at 2000 V for the first ten minute period of operation. No sharp changes in leakage rate occurred during the first five minutes of operation. The temperature of the seal face was also not drastically increasing which indicates the seal was operating successfully at this point.

Figure 6-35 shows that after the first five minutes of operation, the pressure was reduced to 7.8×10^5 Pa (100 psig). This induced the first two instabilities. Figure 6-34 shows that after the pressure was reduced, there were two incidences in which the leakage rate suddenly increased while the face temperature suddenly increased. After eight

minutes of operation the pressure was returned to 1.48 x 10^6 Pa (200 psig). This prevented further instances of sharp spikes in the leakage rate.

After ten minutes of operation the voltage was reduced to 1000 V (see Figure 6-36) and at a time of eleven minutes the pressure was decreased to 7.91 x 10^5 Pa (100 psig) (see Figure 6-35). The decrease in pressure then led to two spikes in leakage rate at eleven and a half and twelve minutes. At fourteen minutes the voltage was increased slightly. This perturbation induced an additional sudden increase in leakage rate. At this point the cavity pressure was then returned to 1.48 x 10^5 (200 psig) which prevented further spikes in the leakage rate.

At fifteen minutes the speed of the test rig was reduced to 3000 rad/sec (28,500 rpm) as presented in Figure 6-37. The voltage was also increased at this point to 2000 V. At sixteen minutes the pressure was reduced to 4.46 x 10^5 Pa (50 psig) and held at this point for three minutes. No leakage rate instabilities occurred at this reduced speed and pressure thus demonstrating that the onset of seal instabilities is sensitive to the rotational speed.

This test demonstrates that reduced cavity pressure and increased rotational speed promote seal instabilities. To prevent these instabilities it is essential to minimize fabrication and assembly tolerances which could produce excessive runout.

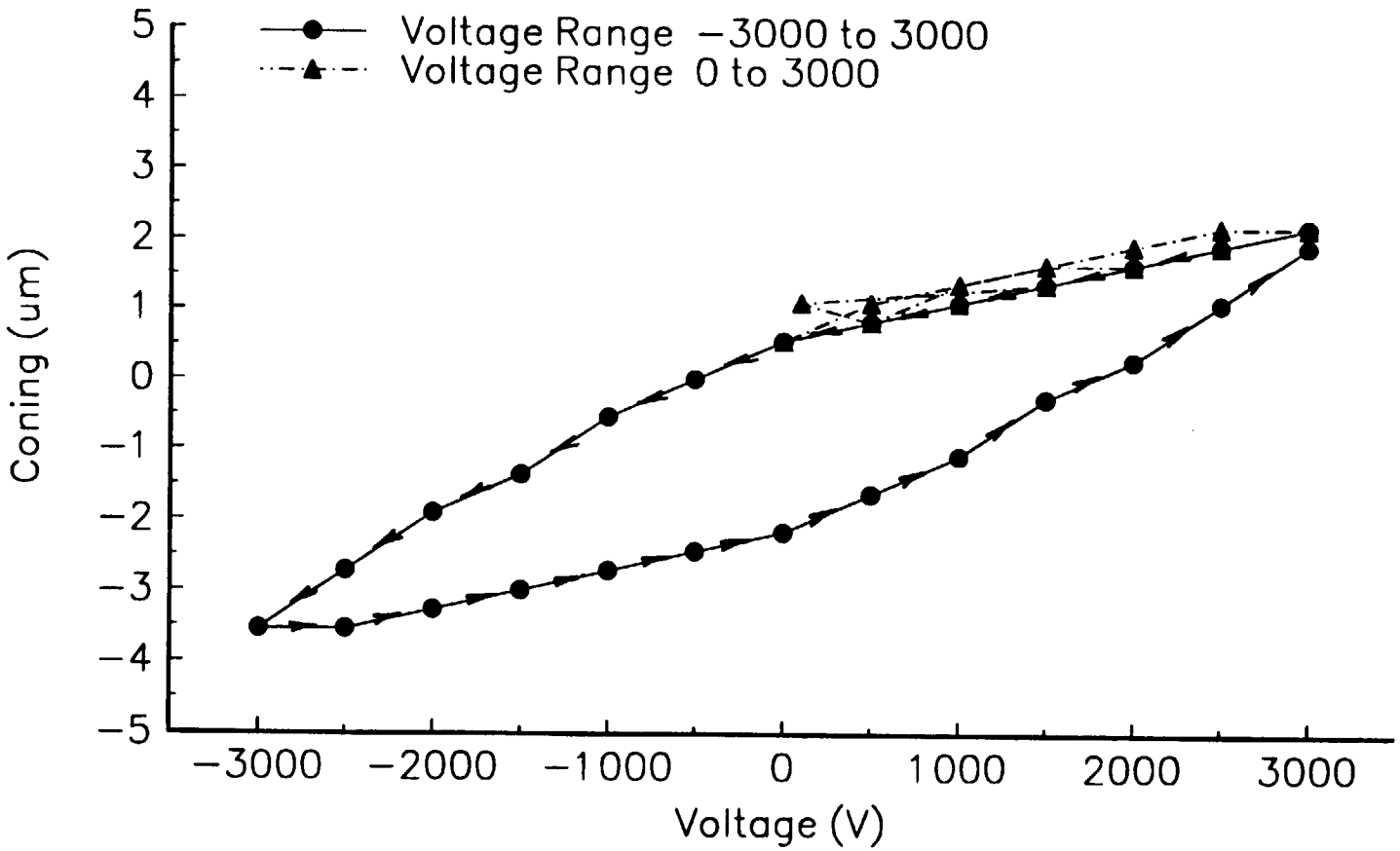

Figure 6-1. Experimental Coning versus Voltage

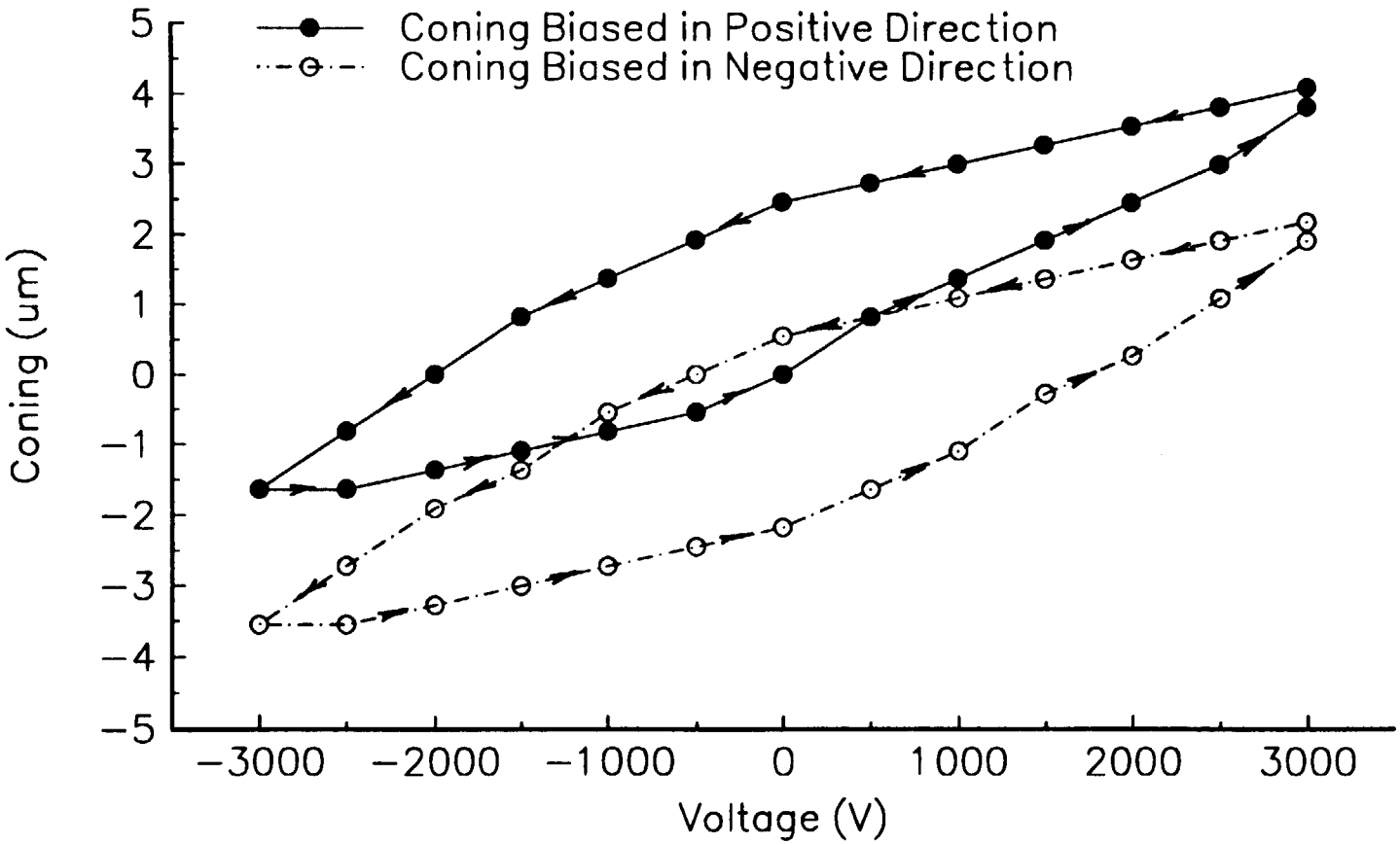

Figure 6-2. Experimental Coning versus Voltage - Effects of Biasing

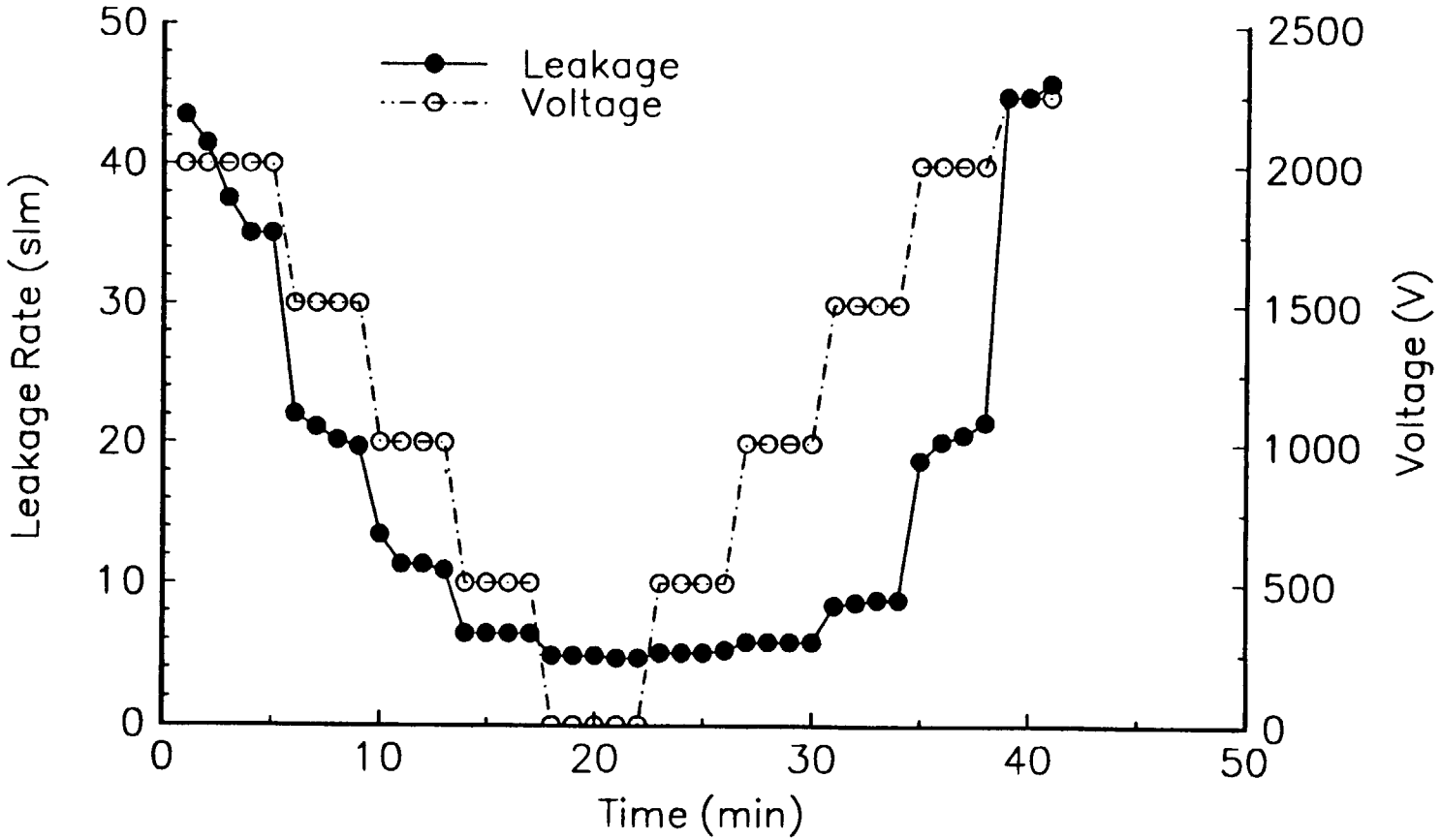

Figure 6-3. Steady State Helium Test - P = 1.48 x 10^6 Pa, ω = 3250 rad/sec

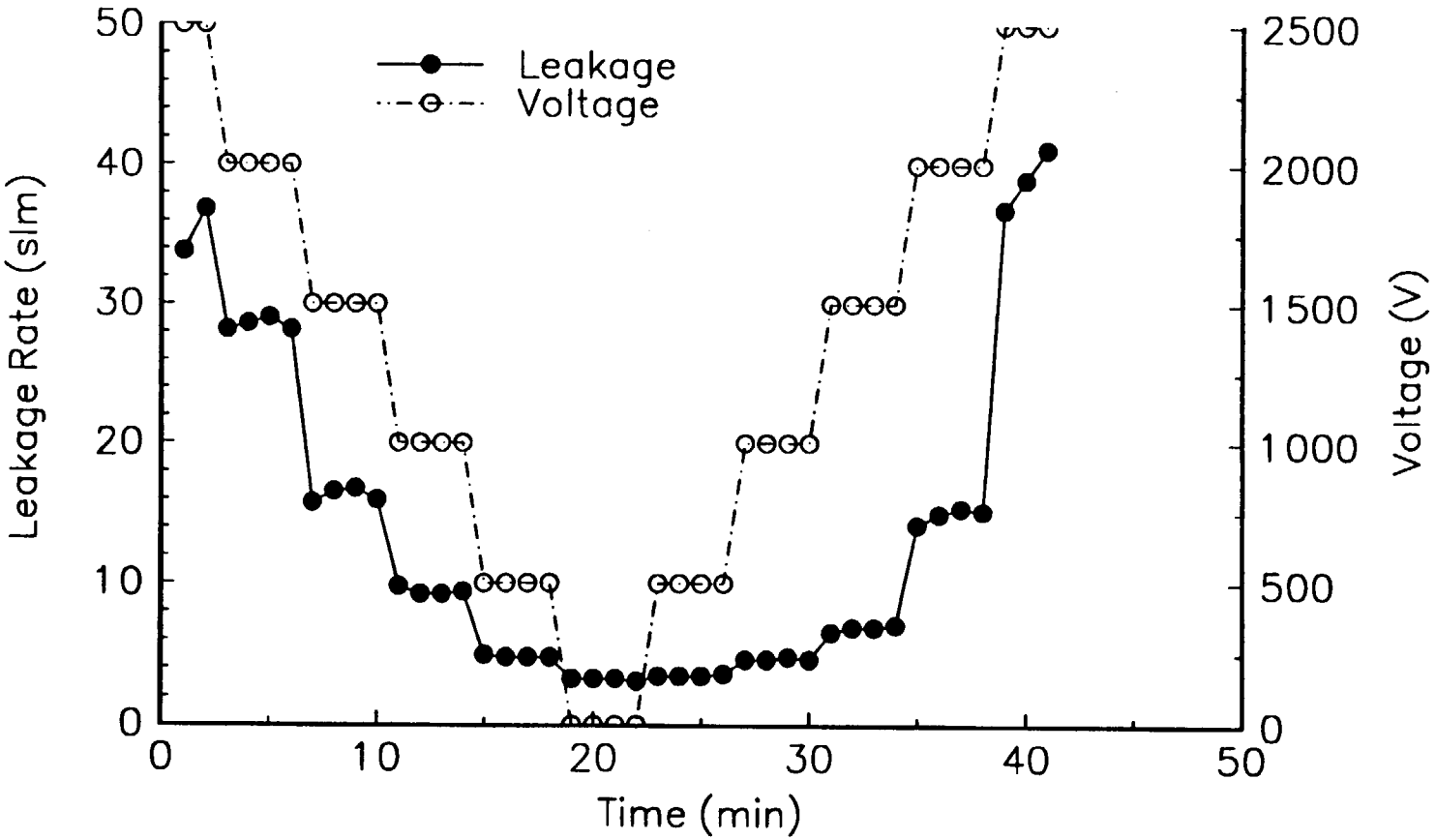

Figure 6-4. Steady State Helium Test - P = 1.14 x 10^6 Pa, ω = 3250 rad/sec

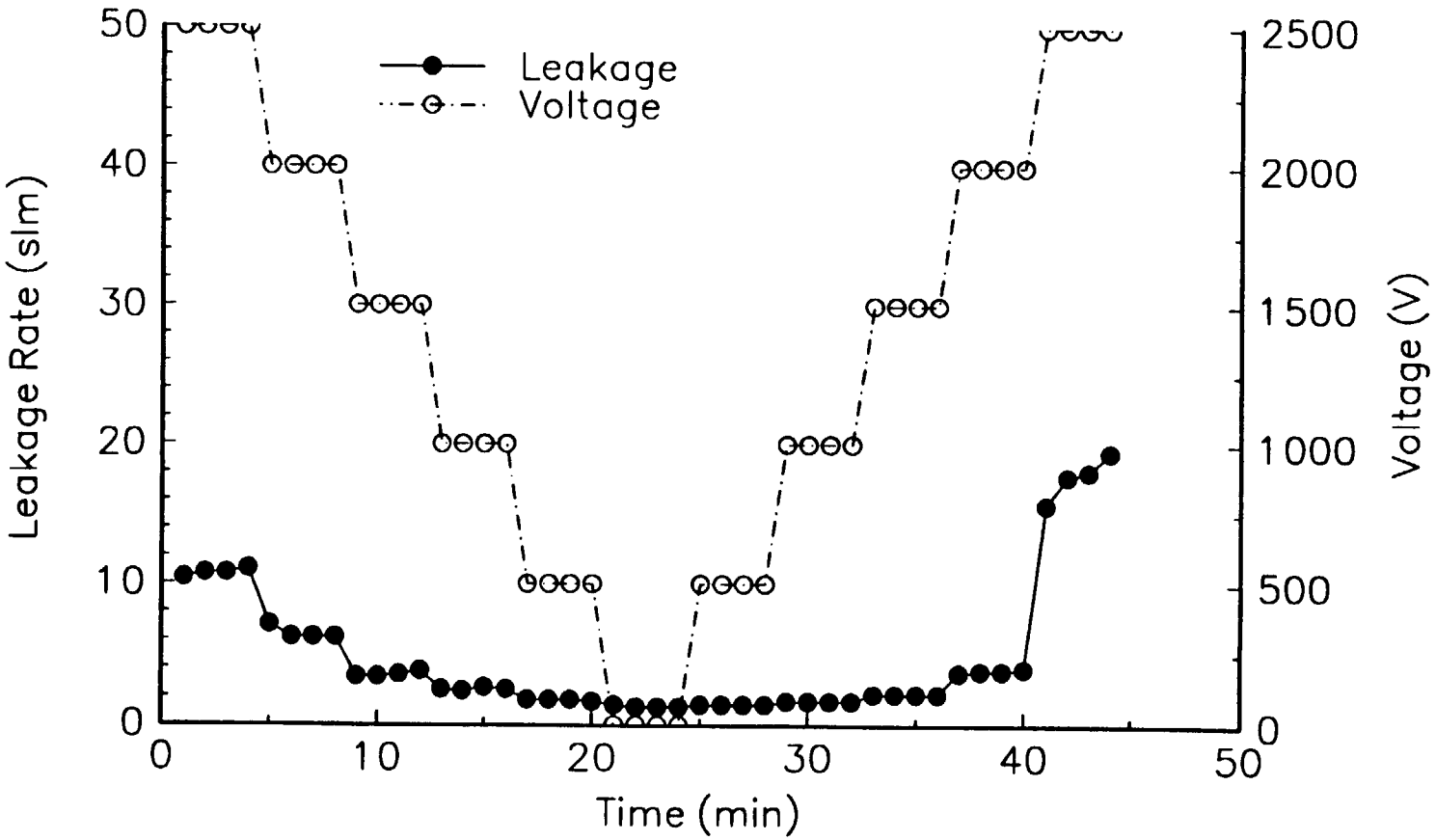

Figure 6-5. Steady State Helium Test - P = 7.91 x 10^5 Pa, ω = 3250 rad/sec

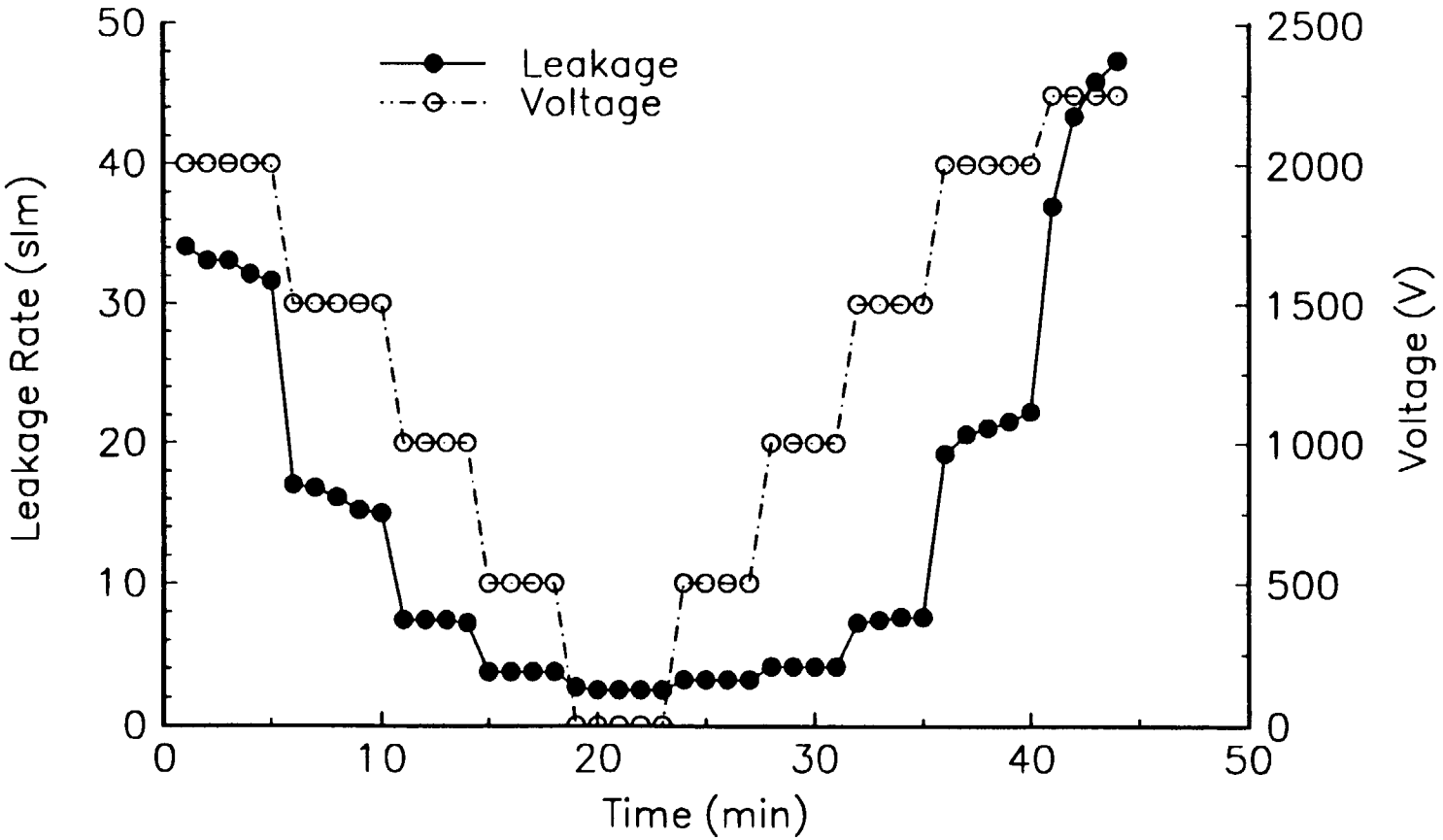

Figure 6-6. Steady State Helium Test - P = 1.48 x 10^6 Pa, ω = 2720 rad/sec

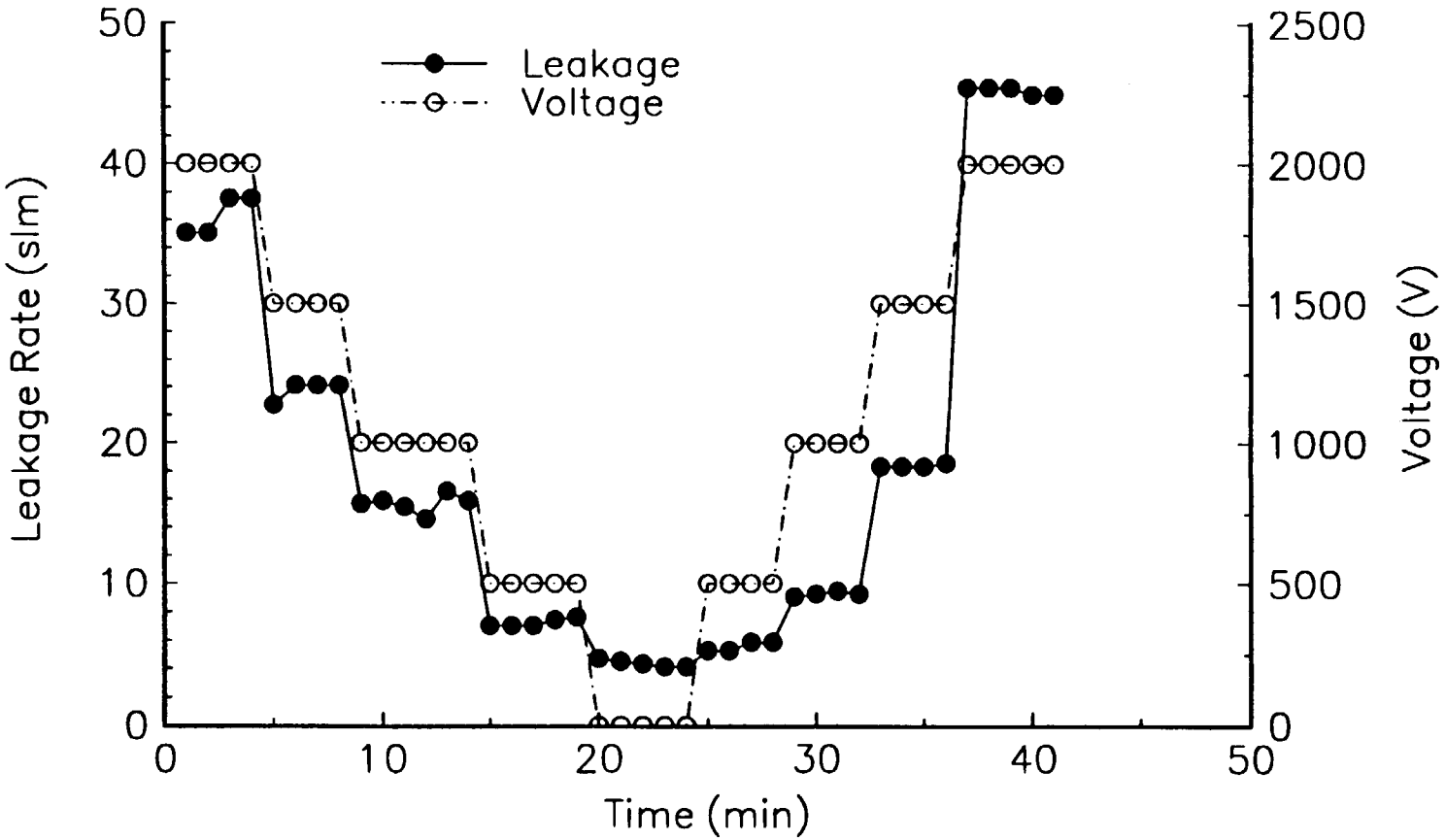

Figure 6-7. Steady State Helium Test - P = 1.48 x 10^6 Pa, ω = 3770 rad/sec

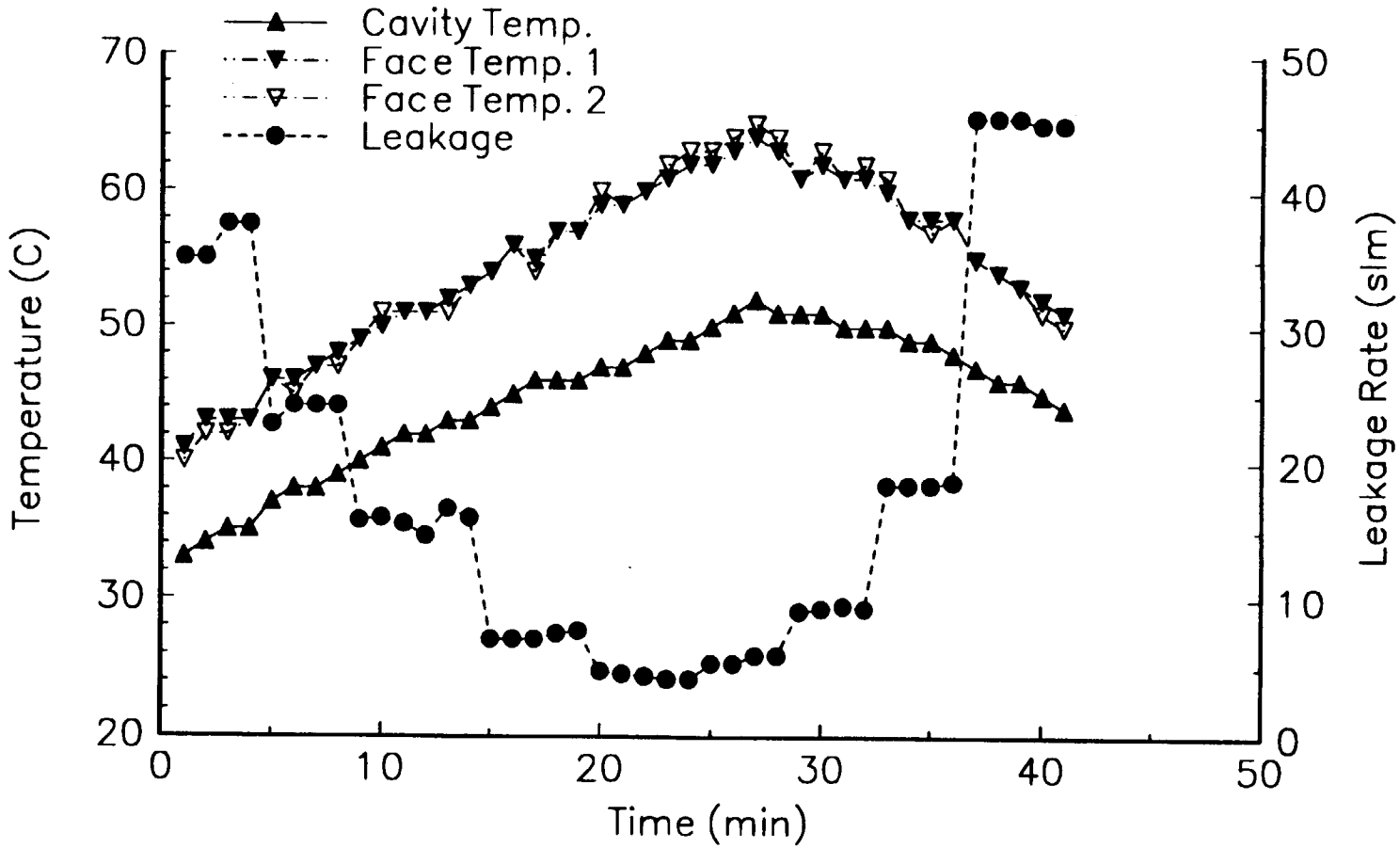

Figure 6-8. Steady State Helium Test - Face and Cavity Temperatures

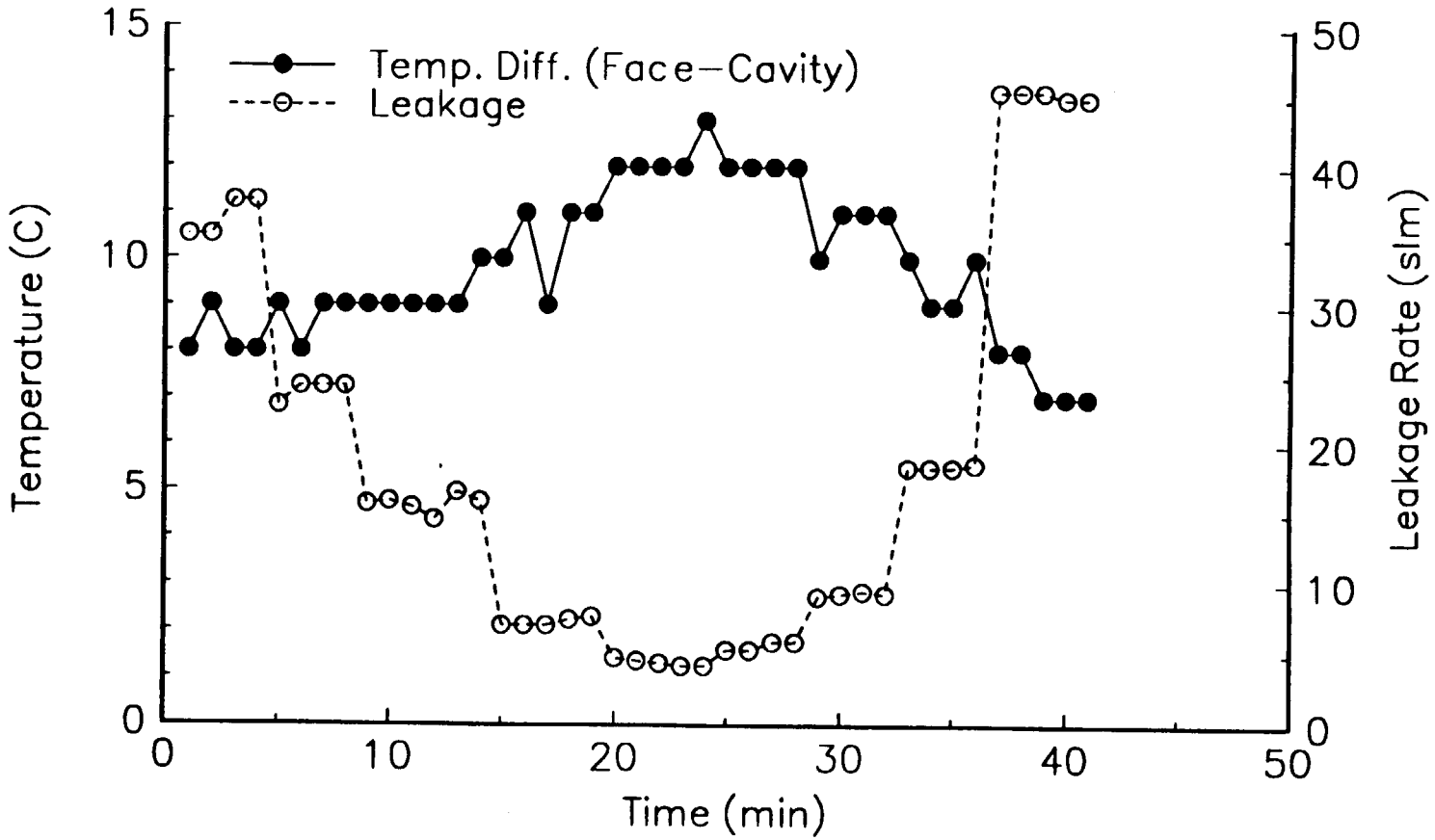

Figure 6-9. Steady State Helium Test - Temperature Difference versus Leakage Rate

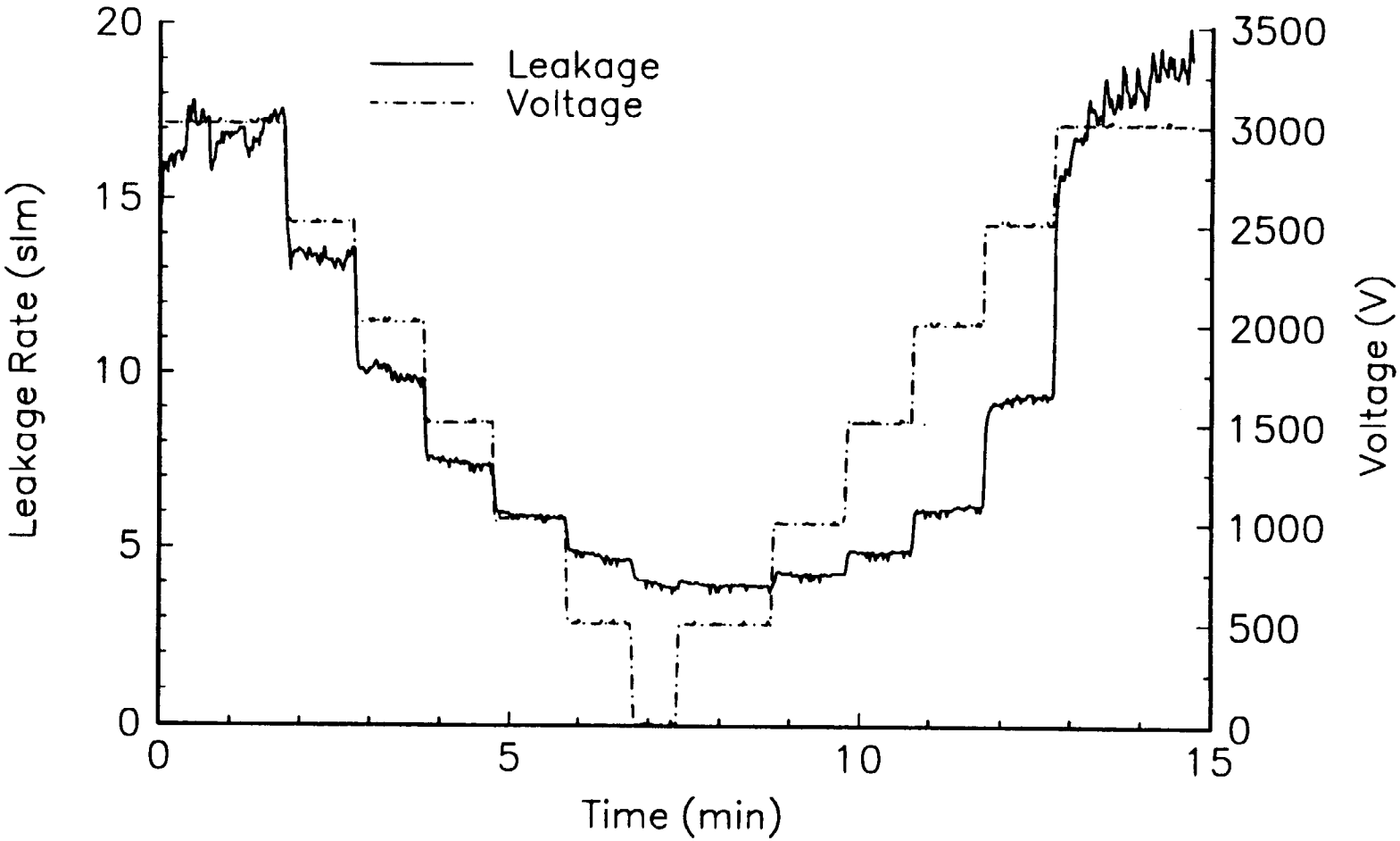

Figure 6-10. Steady State Air Test - P = 1.34 x 10^6 Pa, ω = 3770 rad/sec

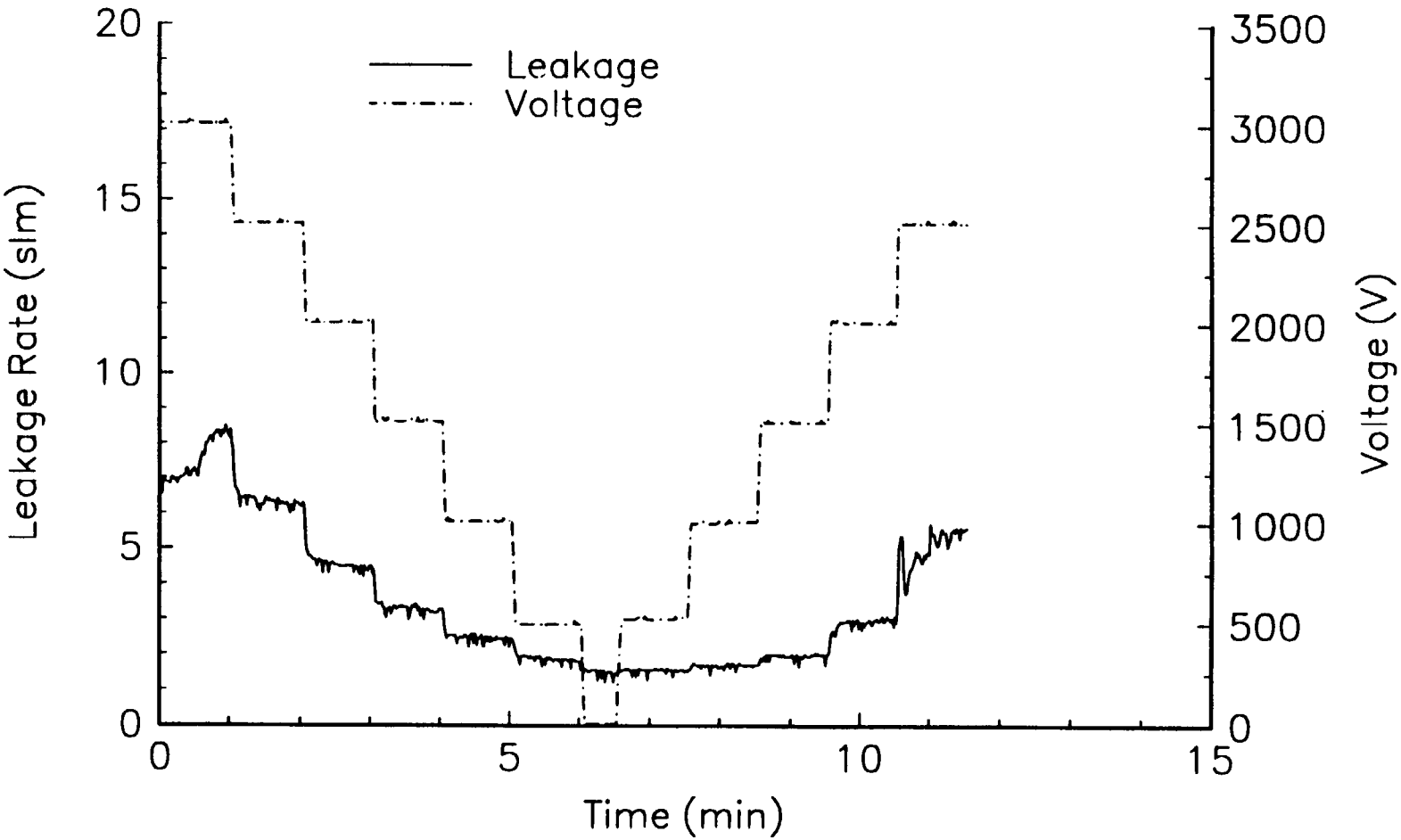

Figure 6-11. Steady State Air Test - P = 6.48 x 10^5 Pa, ω = 3770 rad/sec

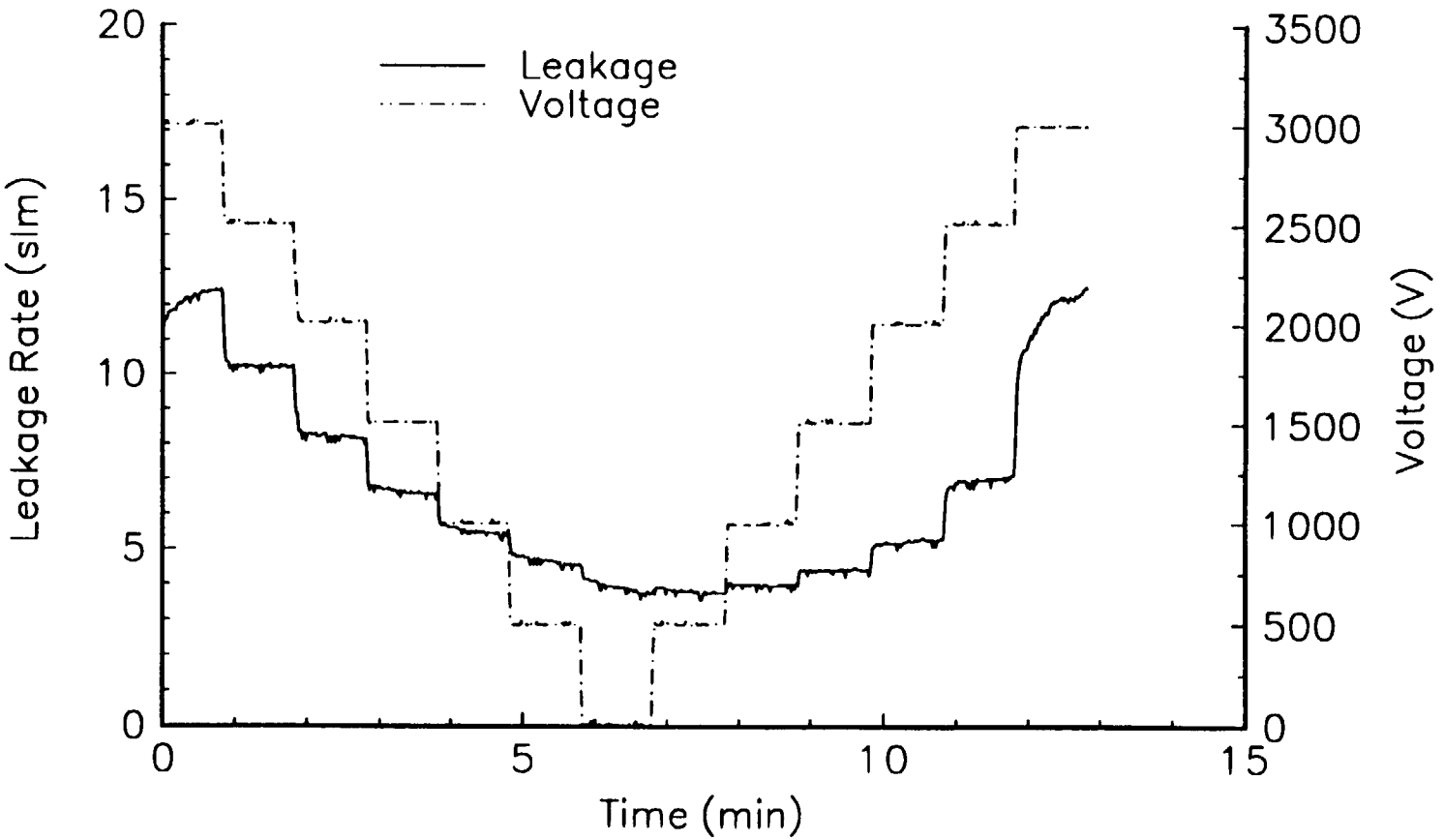

Figure 6-12. Steady State Air Test - P = 1.34 x 10^6, ω = 3140 rad/sec

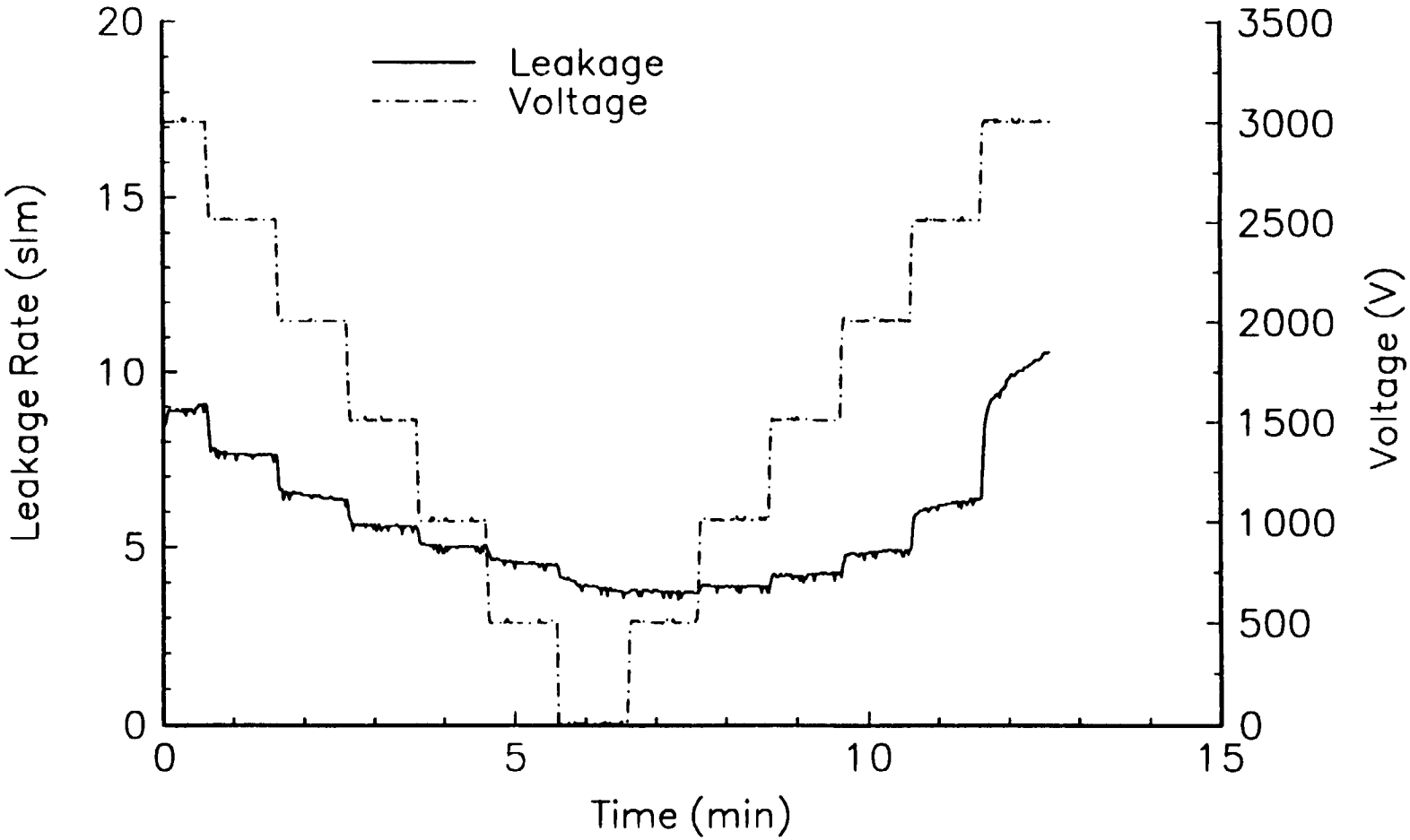

Figure 6-13. Steady State Air Test - P = 1.34 x 10^6 Pa, ω = 2830 rad/sec

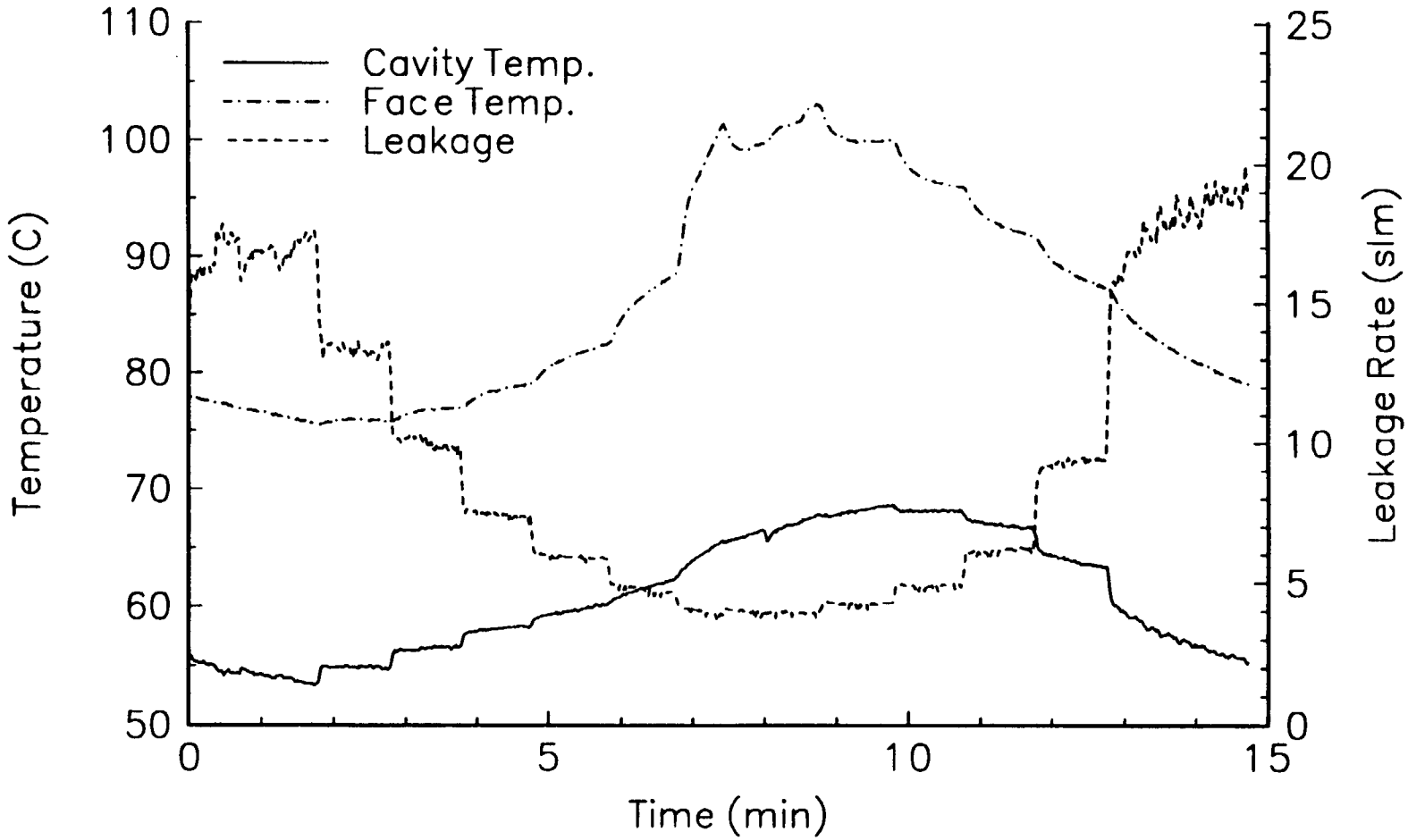

Figure 6-14. Steady State Air Test - Face and Cavity Temperatures

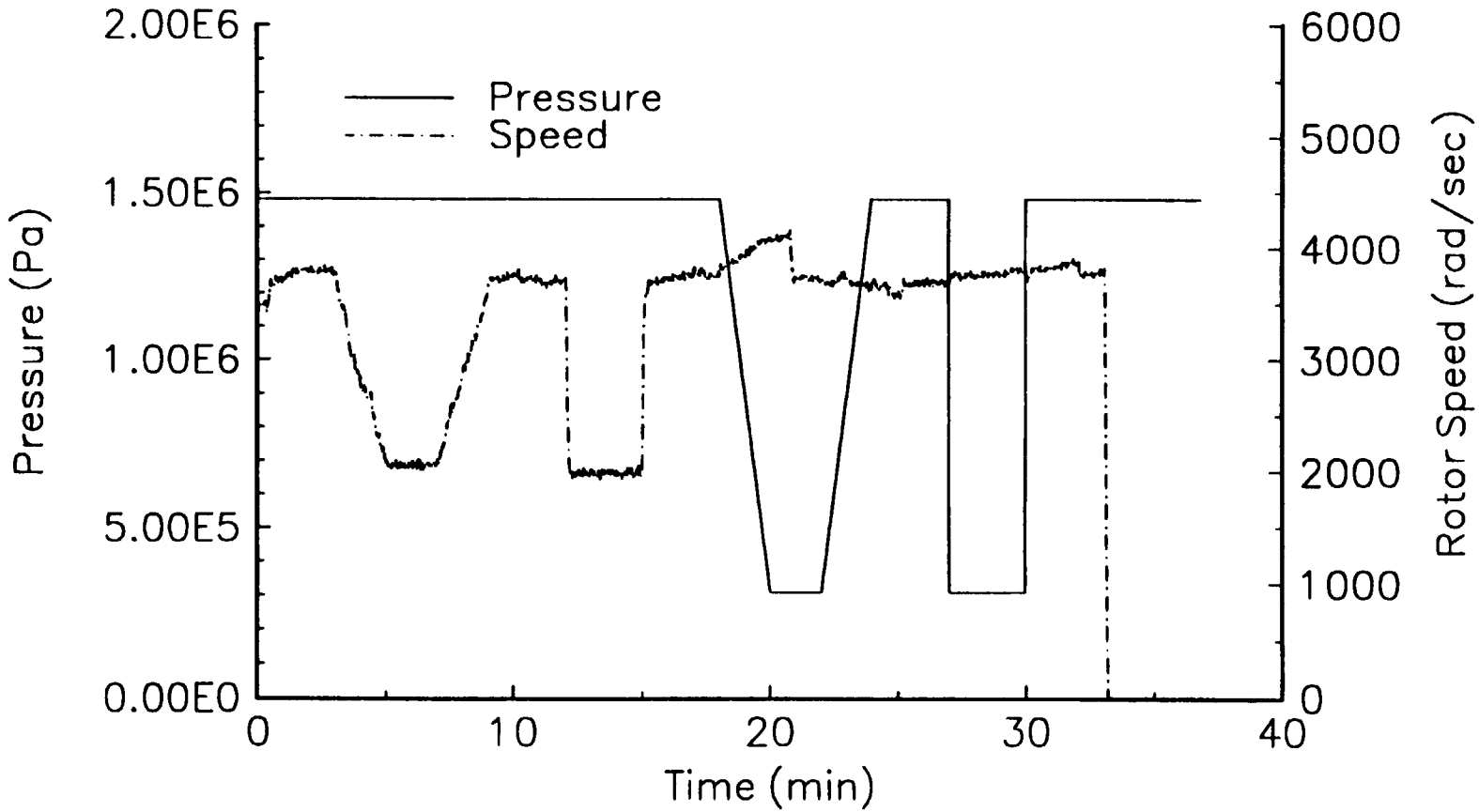

Figure 6-15. Short Term Transient Test 1 - Pressure and Speed Transients

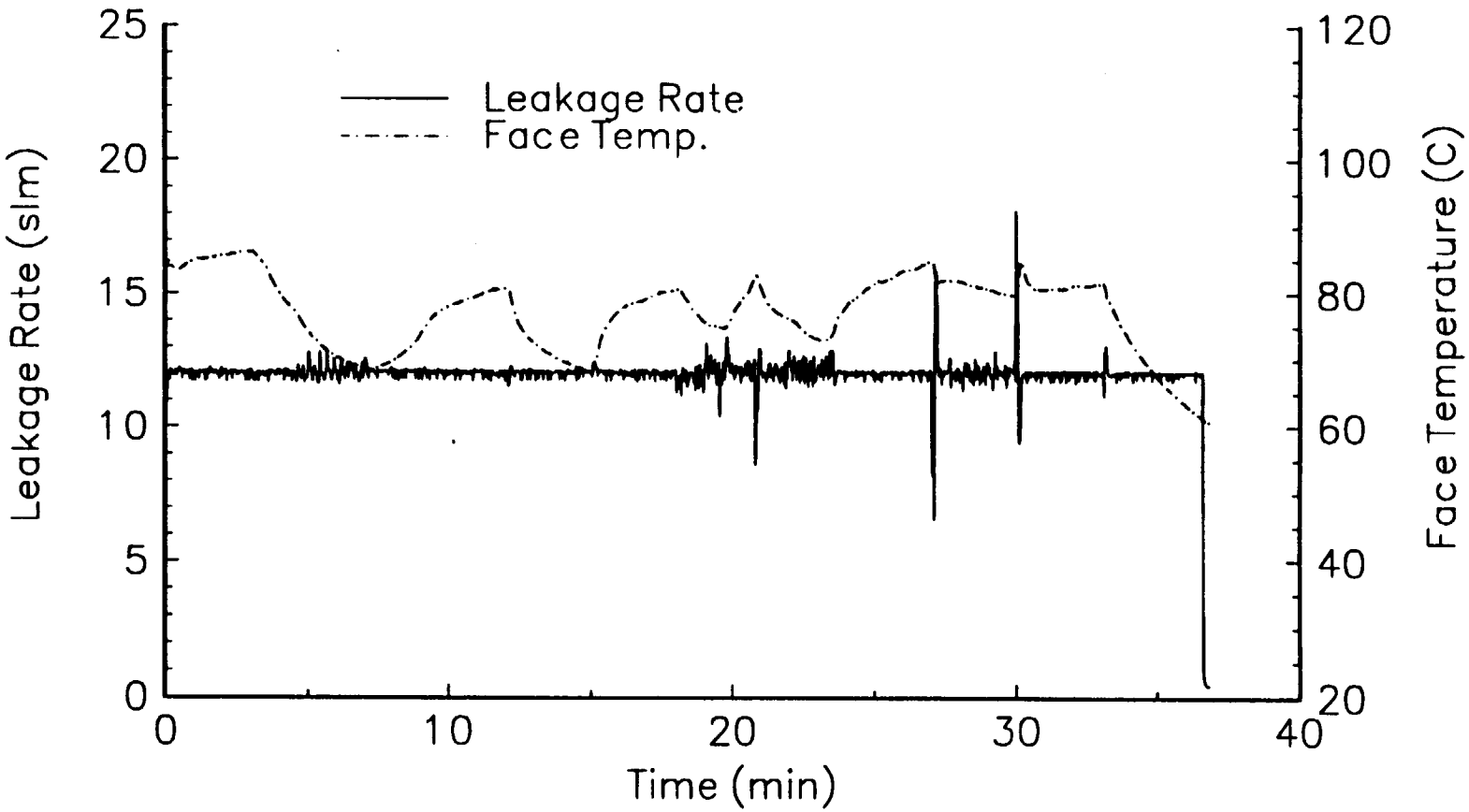

Figure 6-16. Short Term Transient Test 1 - Leakage Rate and Face Temperature

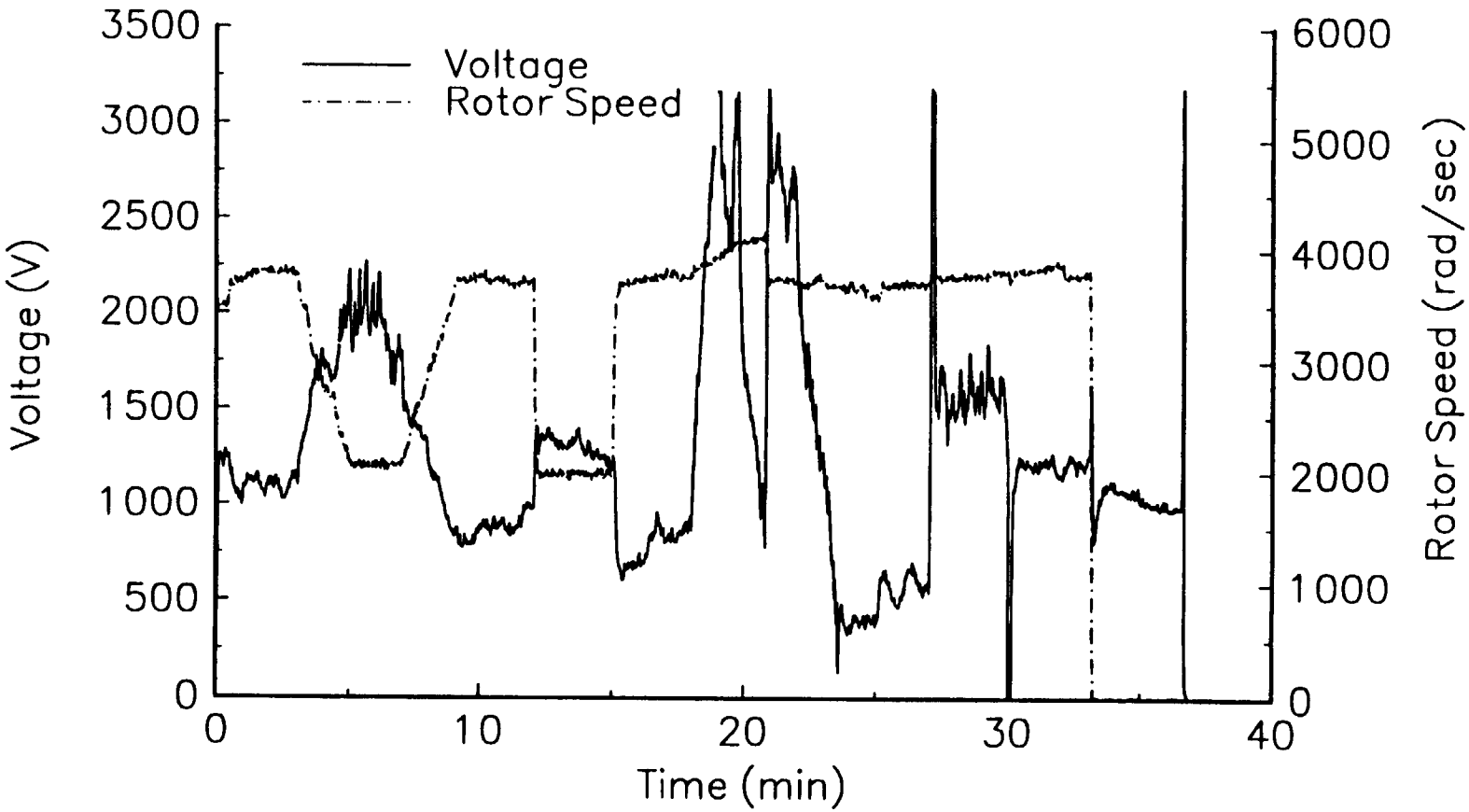

Figure 6-17. Short Term Transient Test 1 - Voltage and Speed

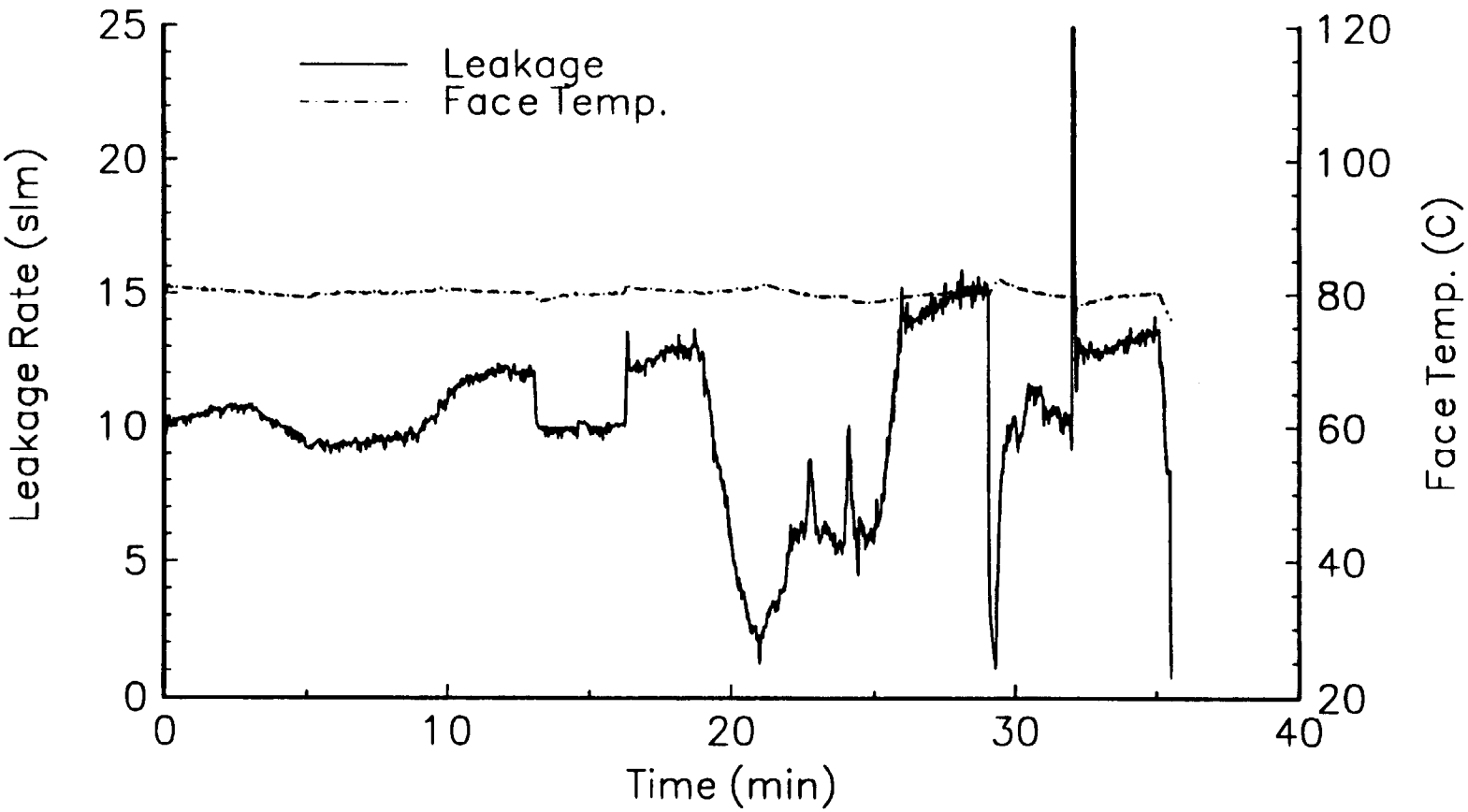

Figure 6-18. Short Term Transient Test 2 - Leakage Rate and Face Temperature

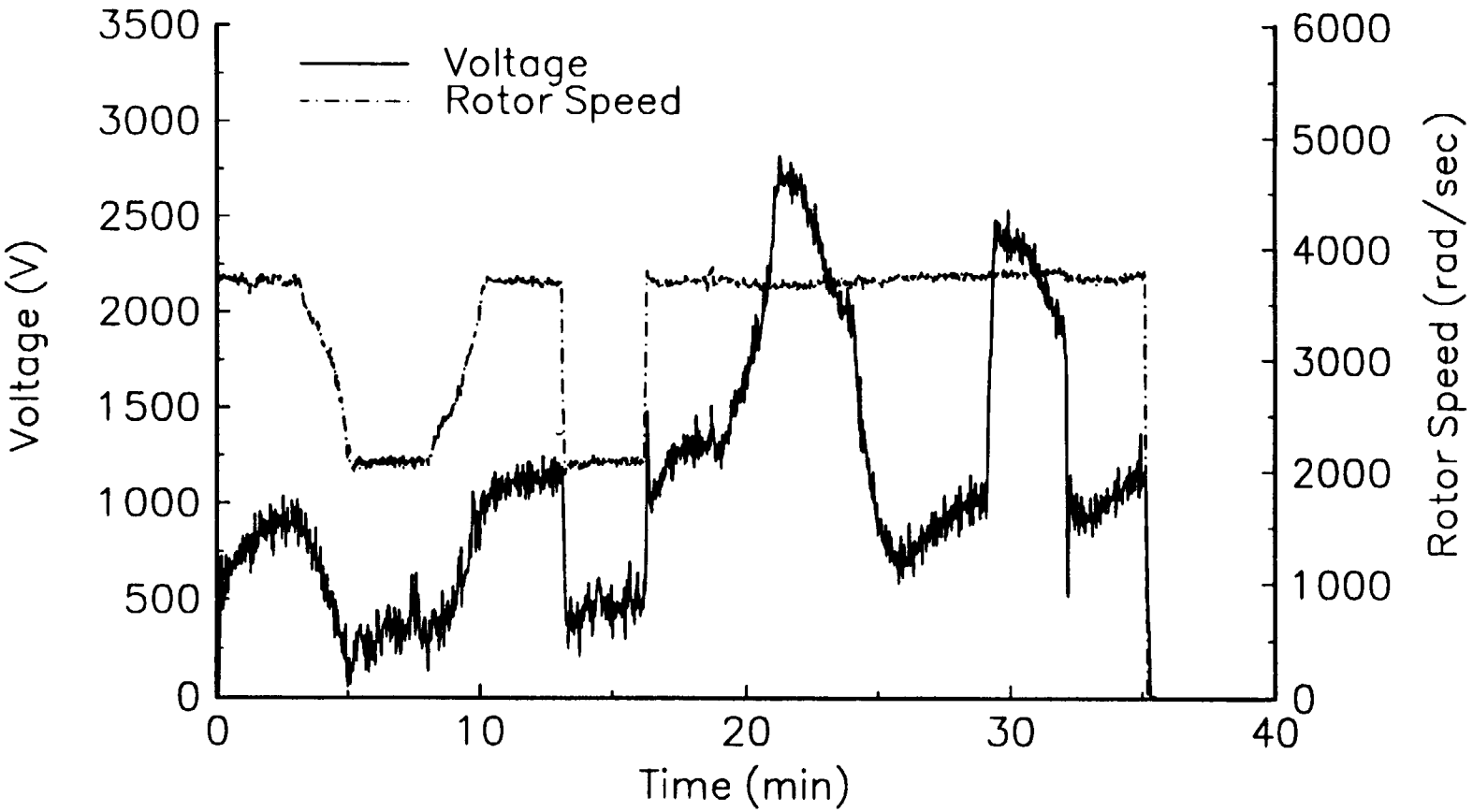

Figure 6-19. Short Term Transient Test 2 - Voltage and Speed

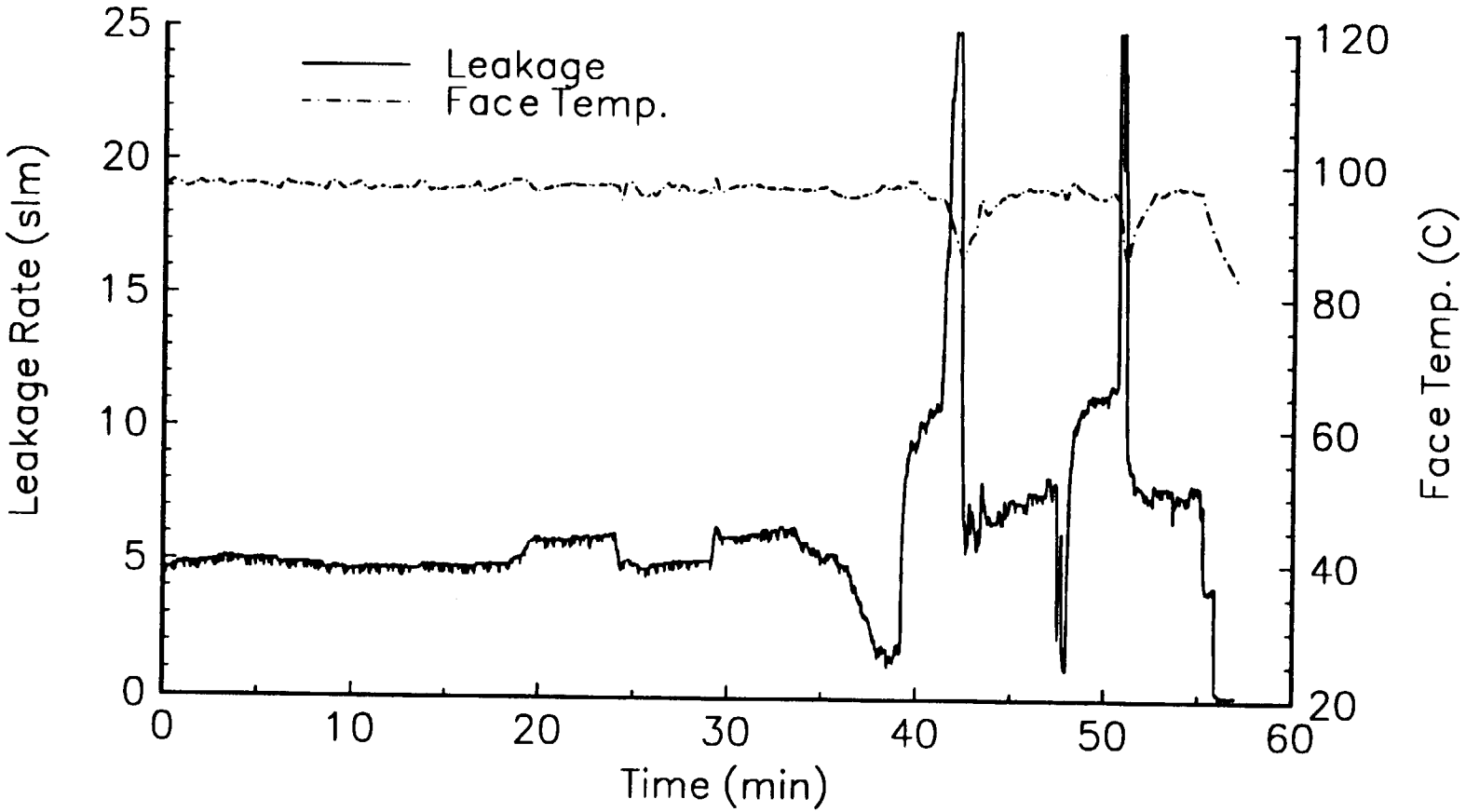

Figure 6-20. Short Term Transient Test 3 - Leakage Rate and Face Temperature

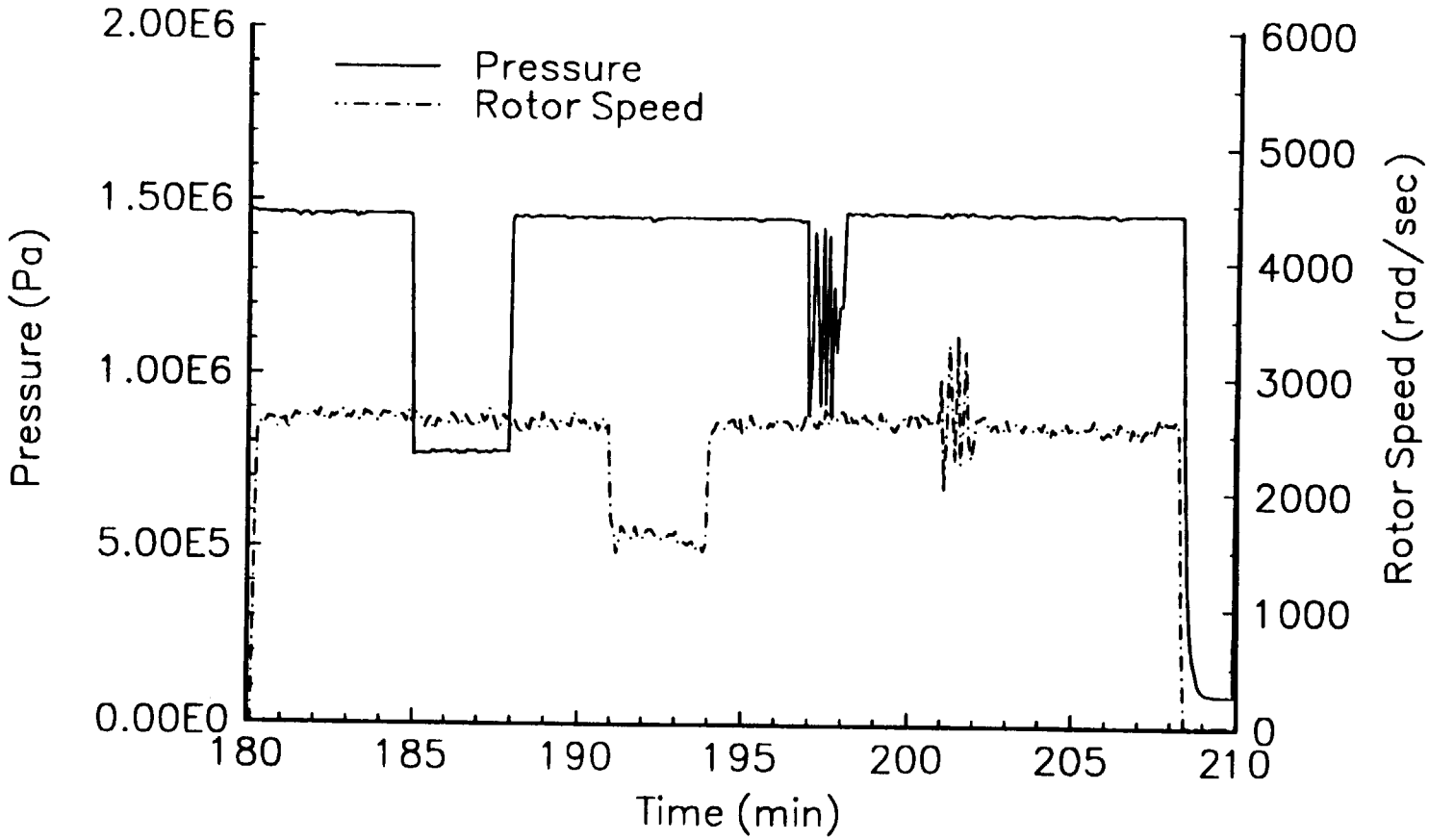

Figure 6-21. Long Term Transient Test 1 - Pressure and Speed Transients

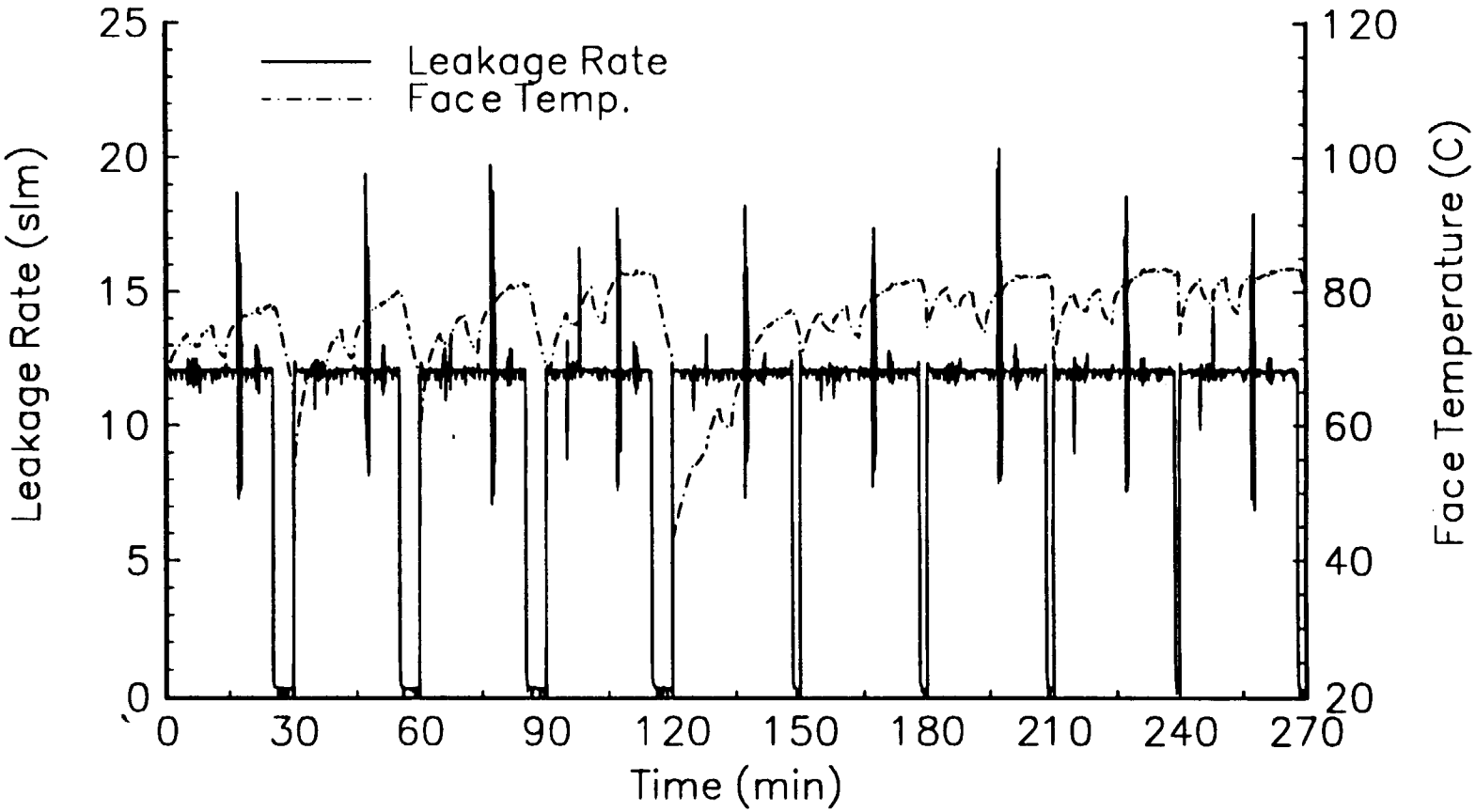

Figure 6-22. Long Term Transient Test 1 - Leakage Rate and Face Temperature for Entire Test

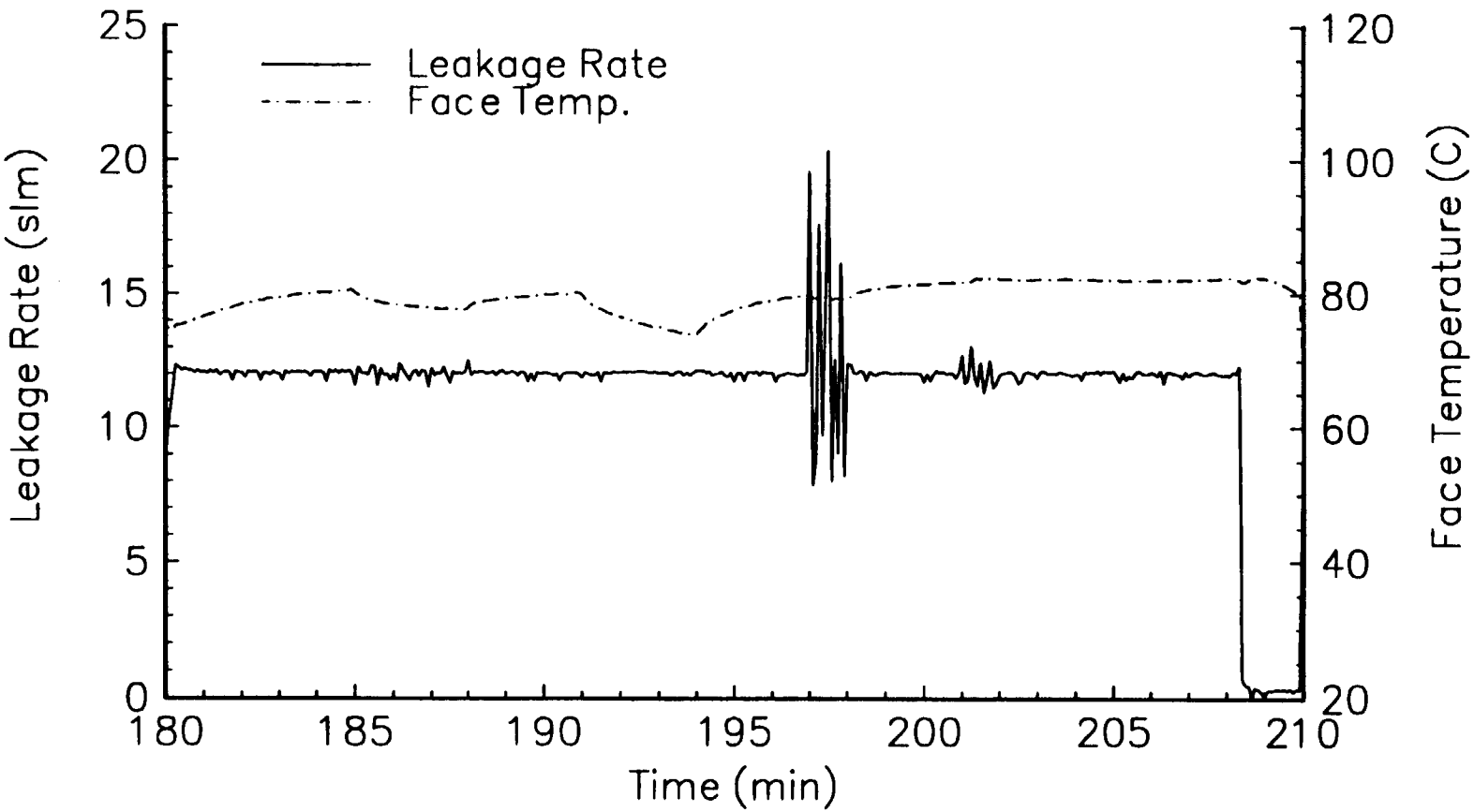

Figure 6-23. Long Term Transient Test 1 - Leakage Rate and Face Temperature for One Test Cycle

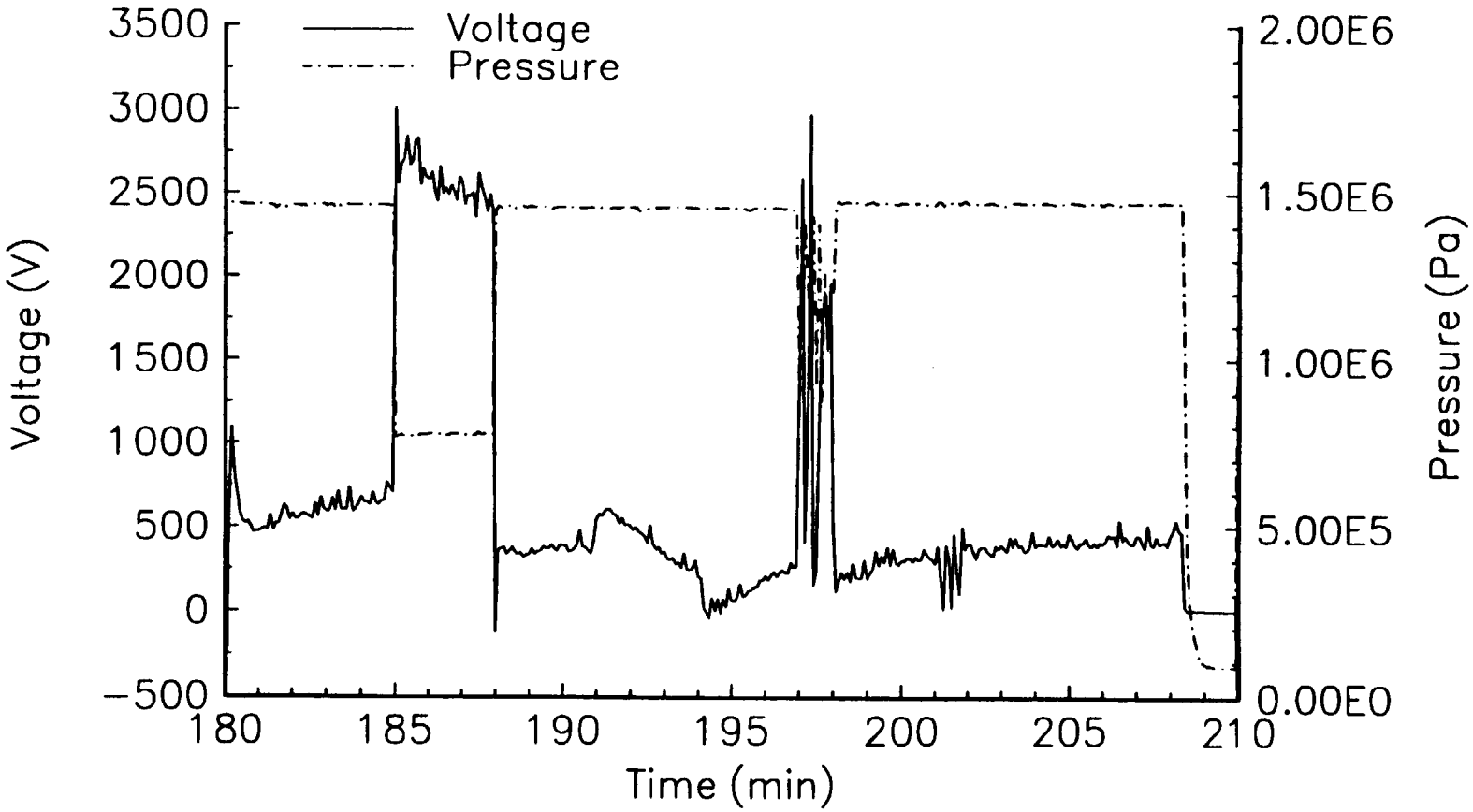

Figure 6-24. Long Term Transient Test 1 - Voltage and Pressure

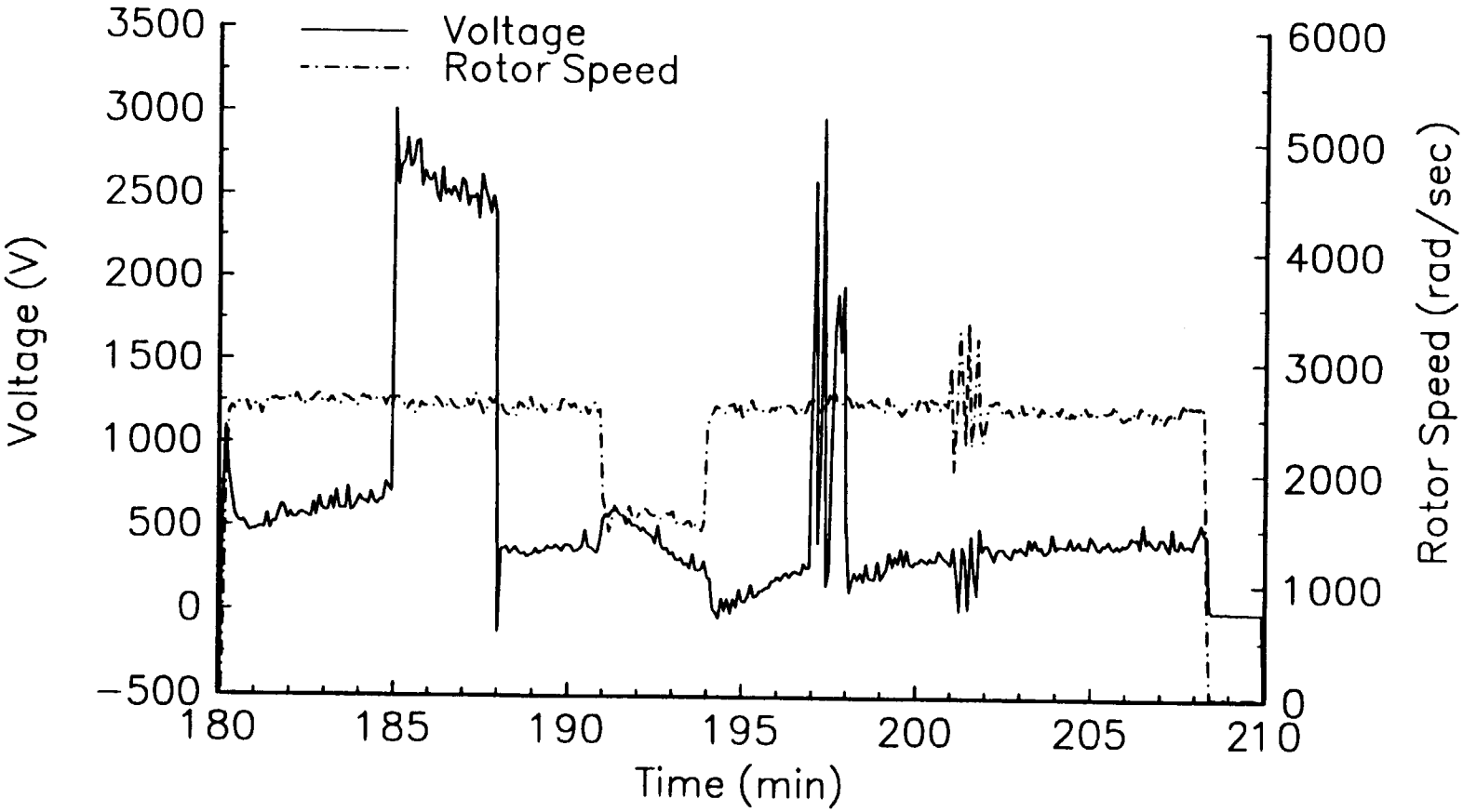

Figure 6-25. Long Term Transient Test 1 - Voltage and Speed

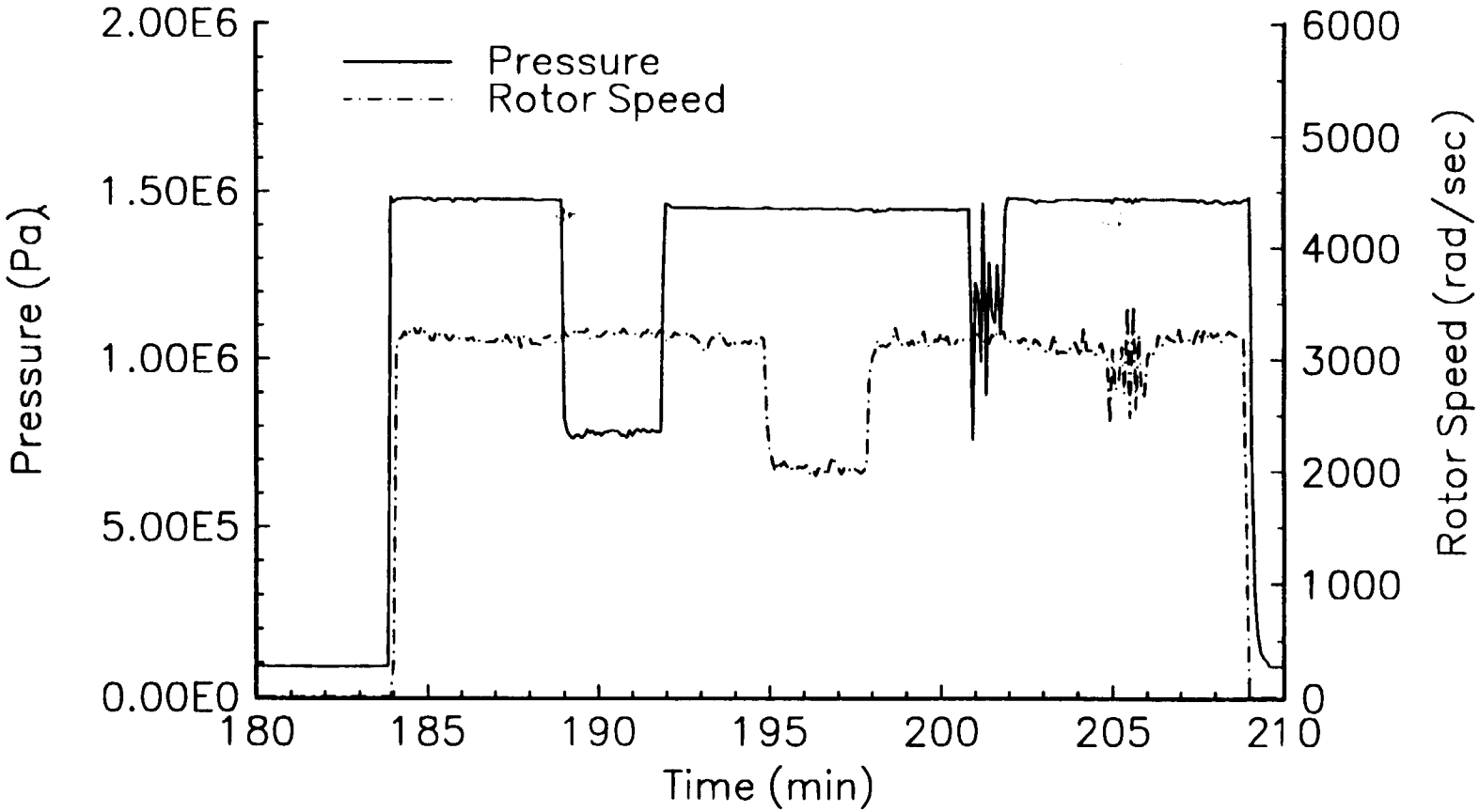

Figure 6-26. Long Term Transient Test 2 - Pressure and Speed Transients

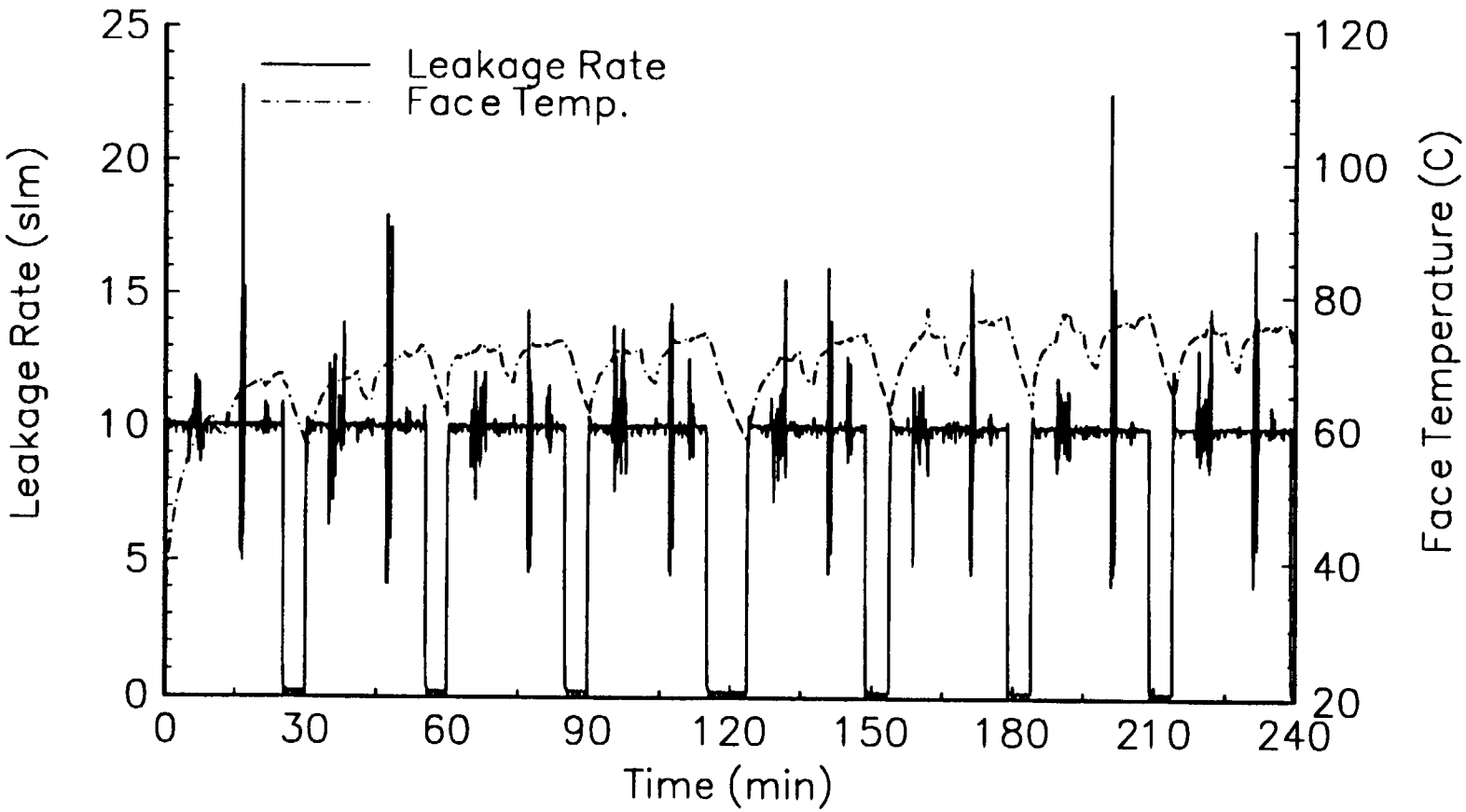

Figure 6-27. Long Term Transient Test 2 - Leakage Rate and Face Temperature for Entire Test

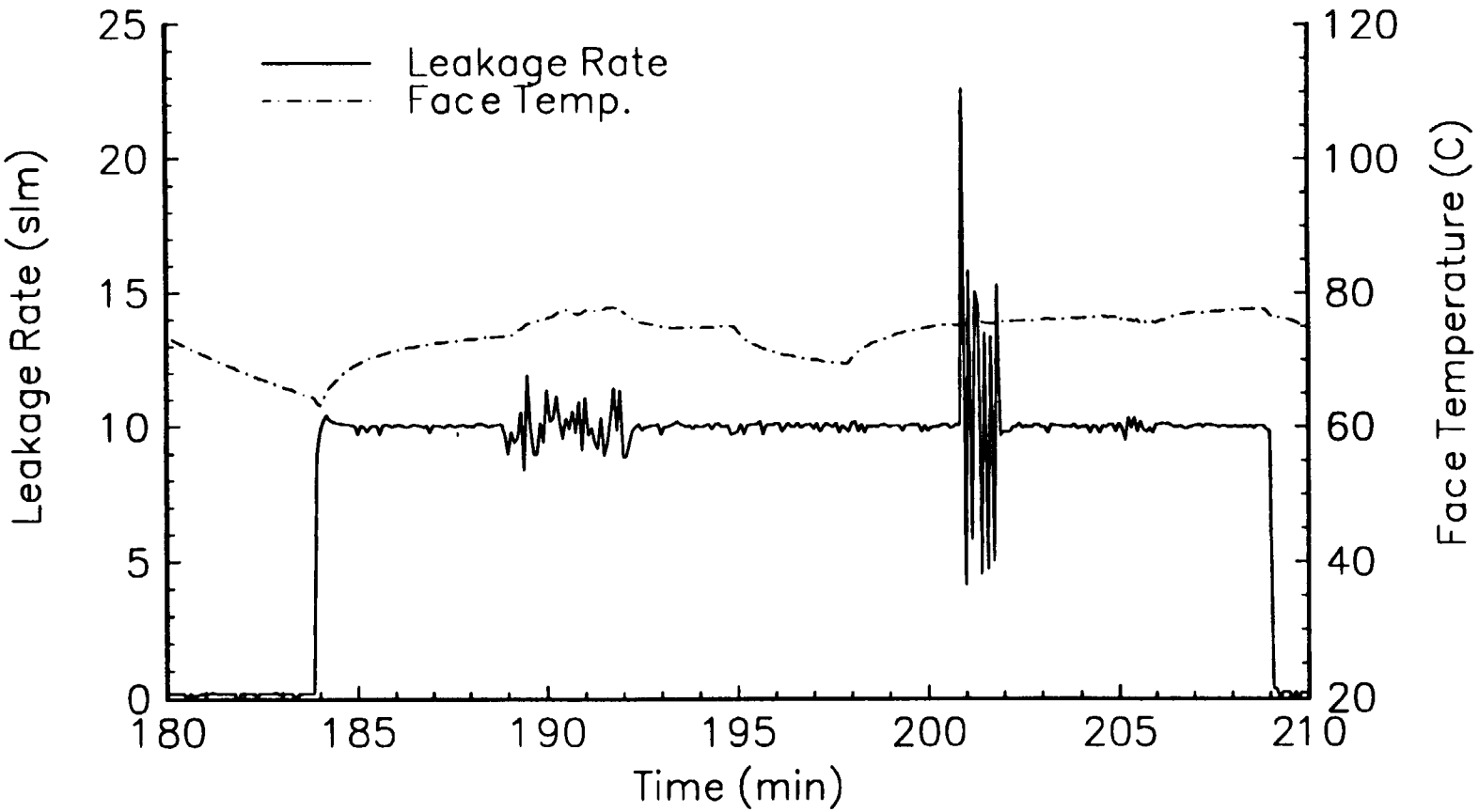

Figure 6-28. Long Term Transient Test 2 - Leakage Rate and Face Temperature for One Test Cycle

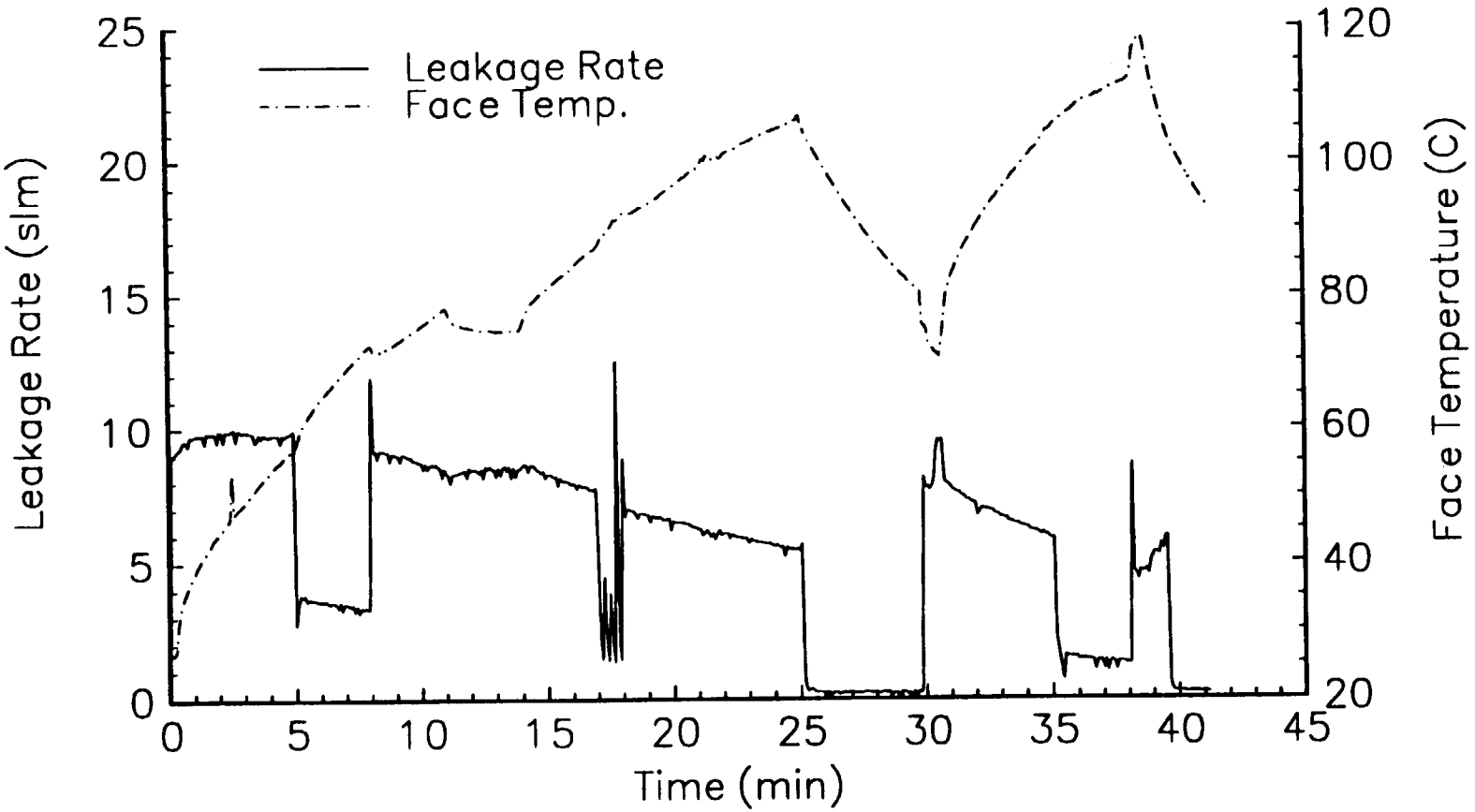

Figure 6-29. Simulation of a Conventional Seal

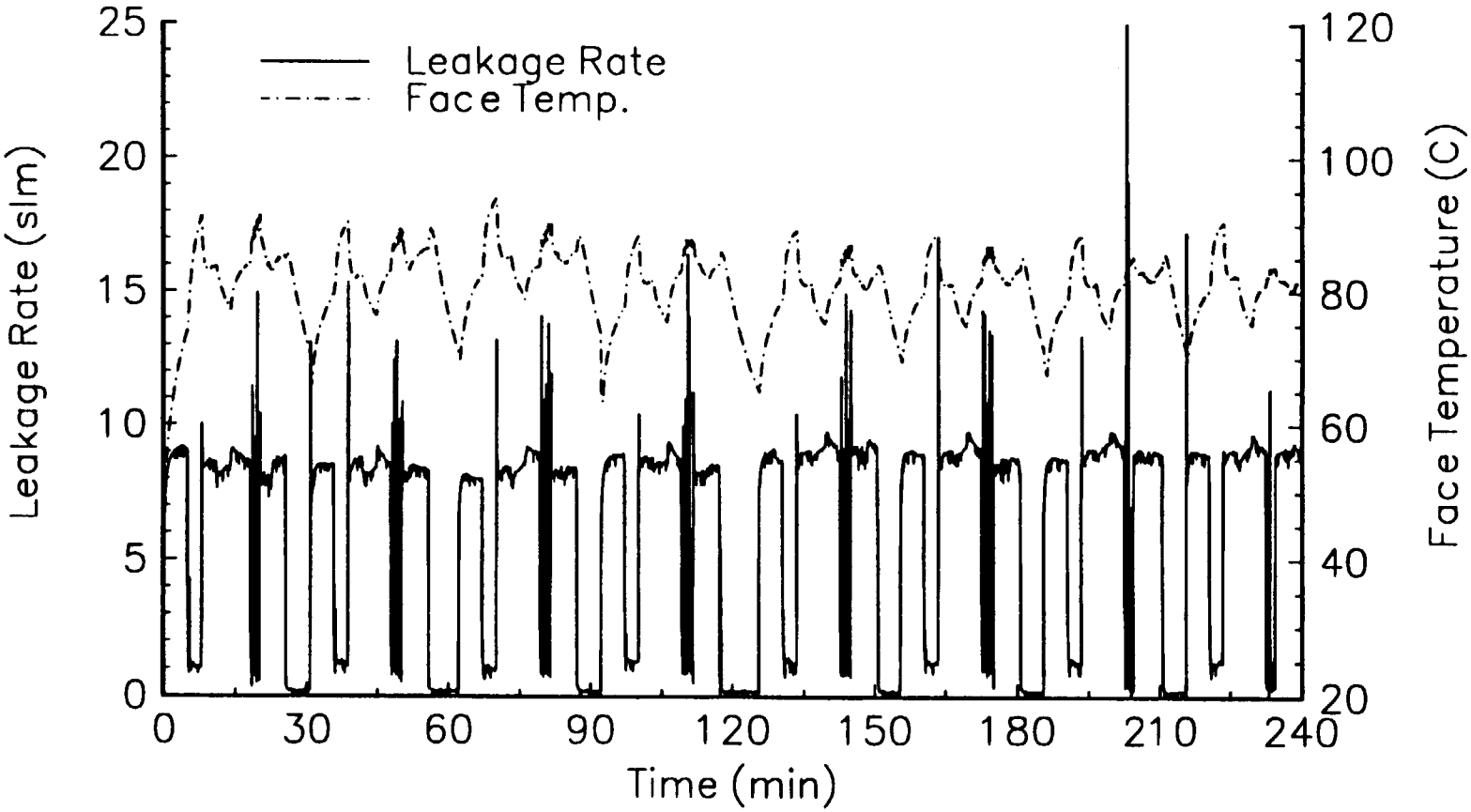

Figure 6-30. Constant Voltage Test 1 - Leakage Rate and Face Temperature

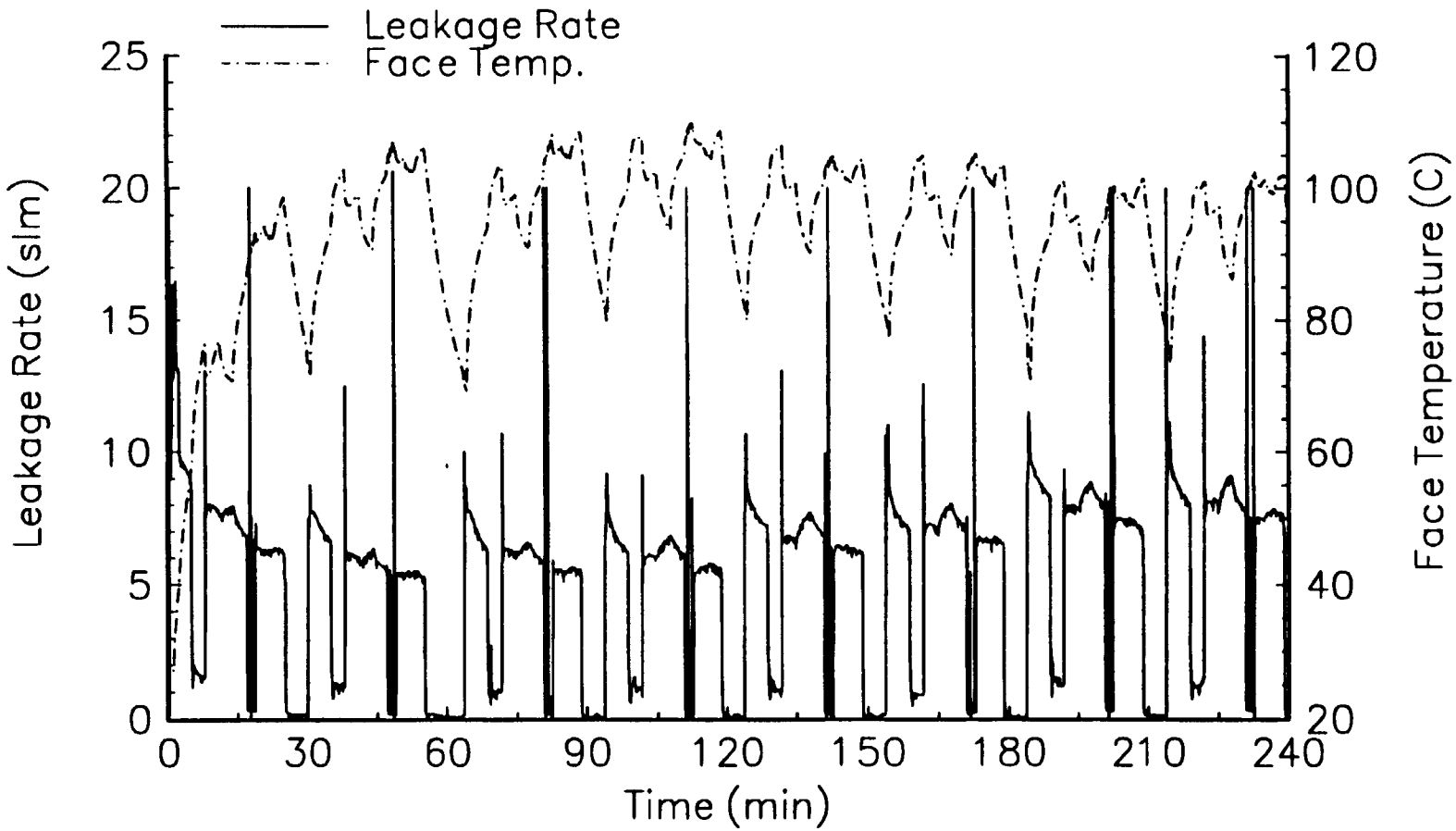

Figure 6-31. Constant Voltage Test 2 - Leakage Rate and Face Temperature

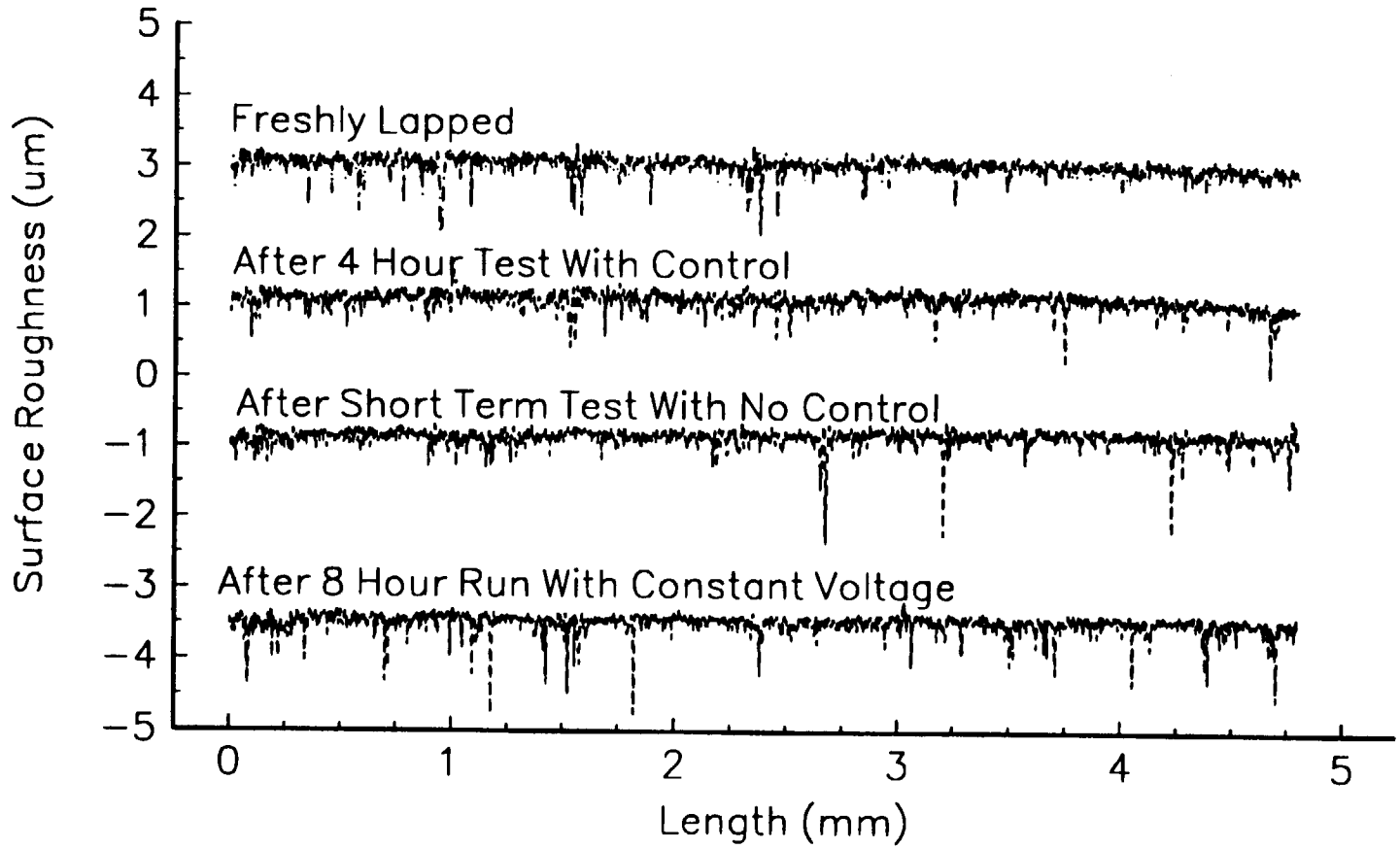

Figure 6-32. Surface Profiles of Carbon Face

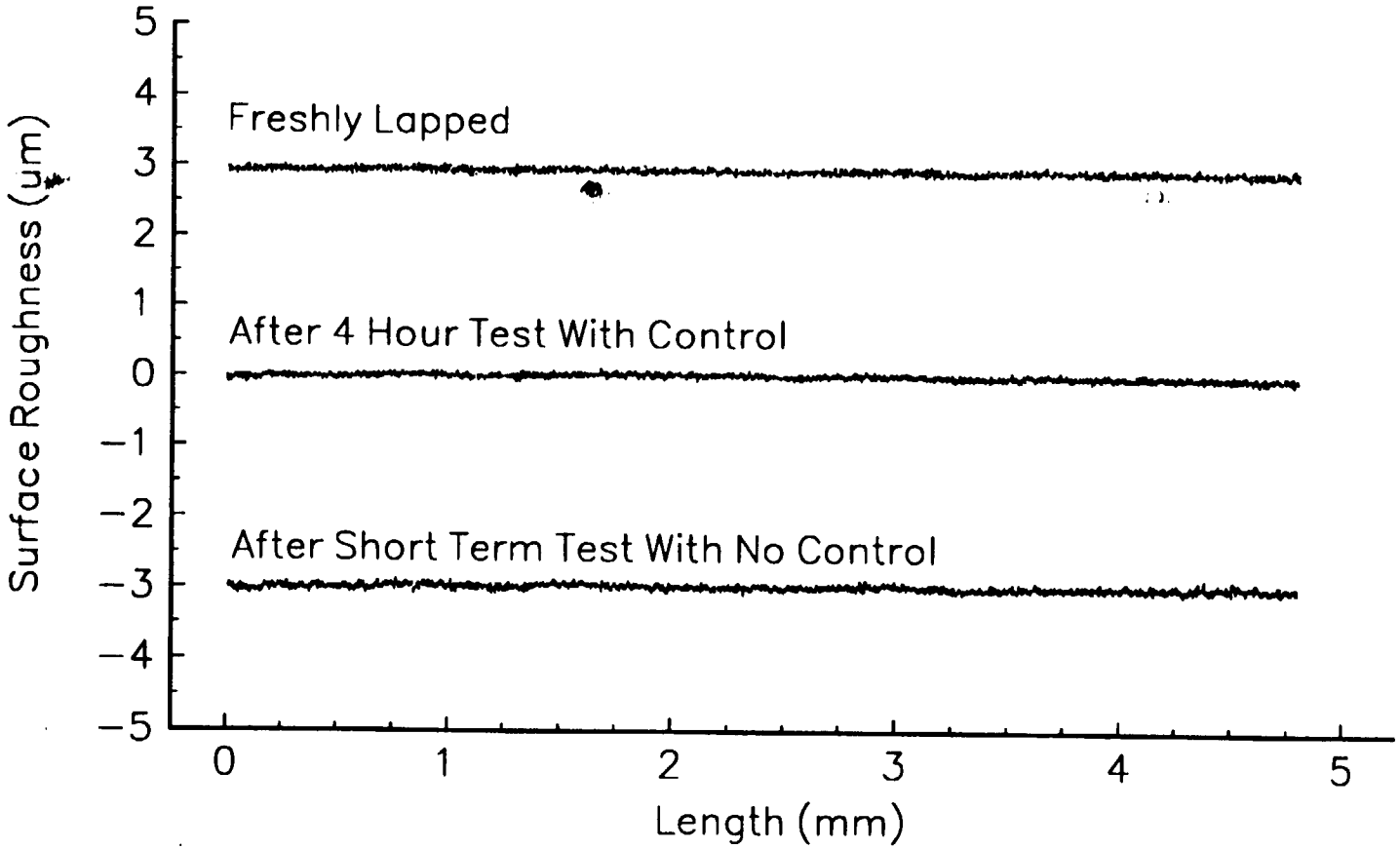

Figure 6-33. Surface Profiles of Tungsten Carbide Face

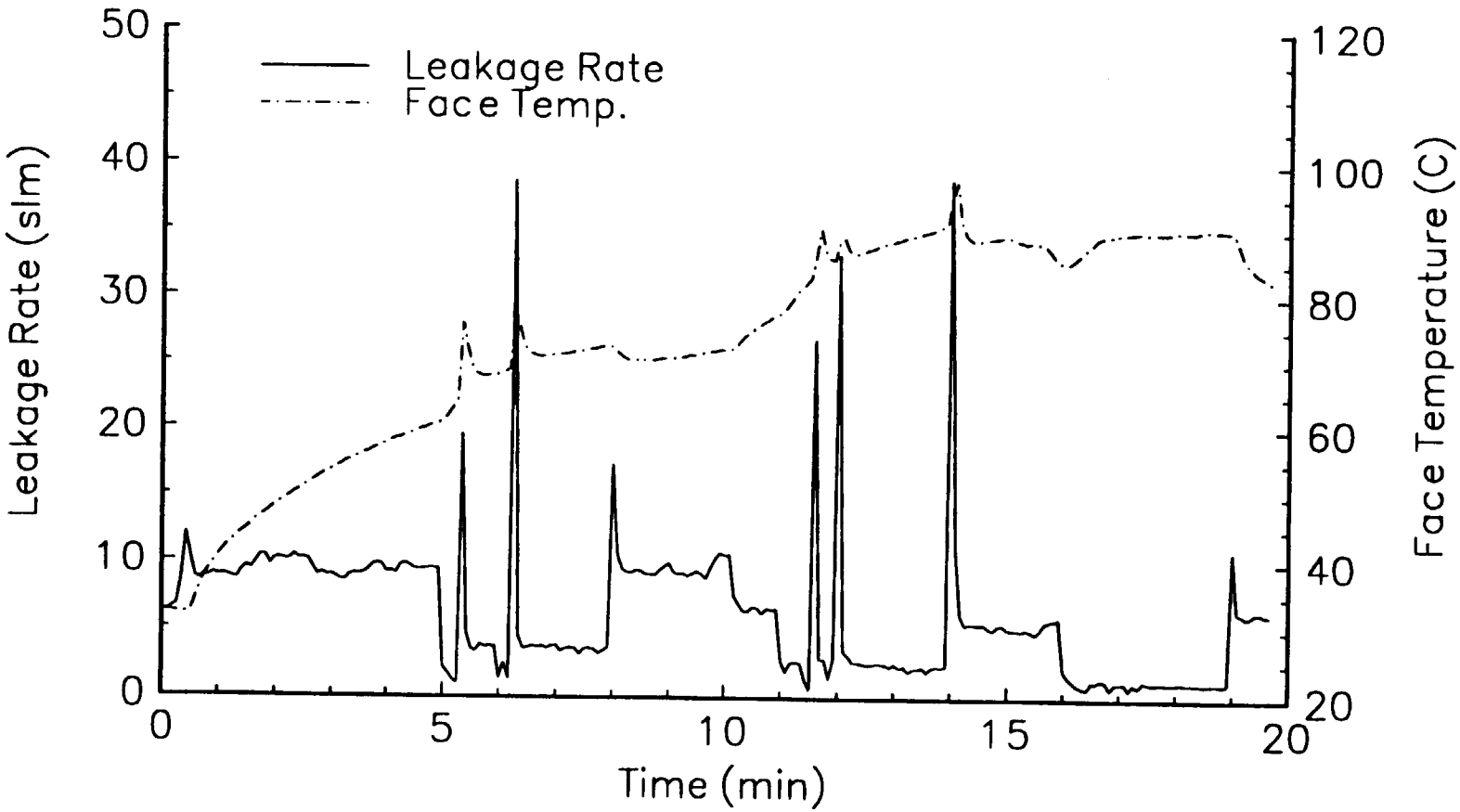

Figure 6-34. Seal Instabilities - Leakage Rate and Face Temperature

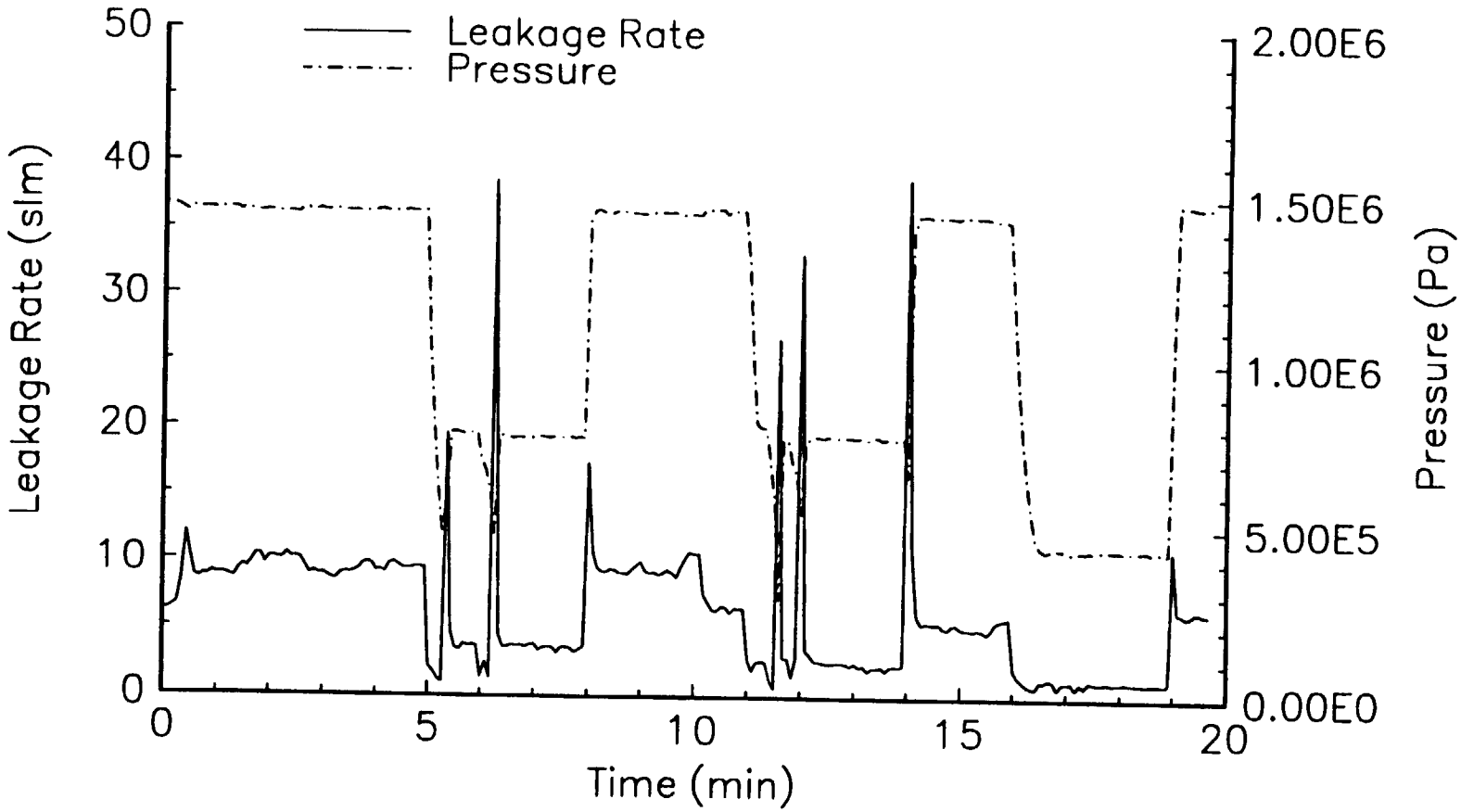

Figure 6-35. Seal Instabilities - Leakage Rate and Pressure

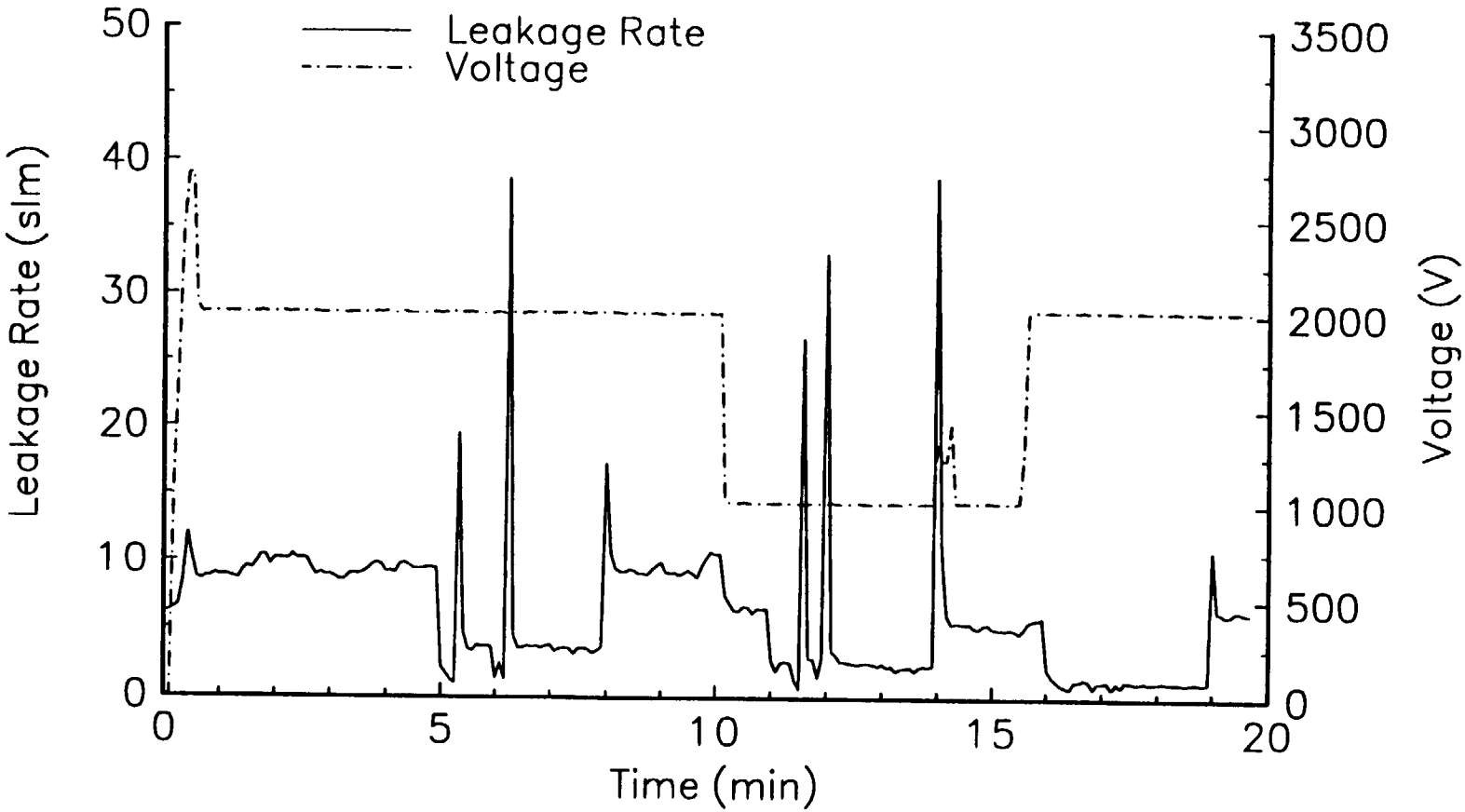

Figure 6-36. Seal Instabilities - Leakage Rate and Voltage

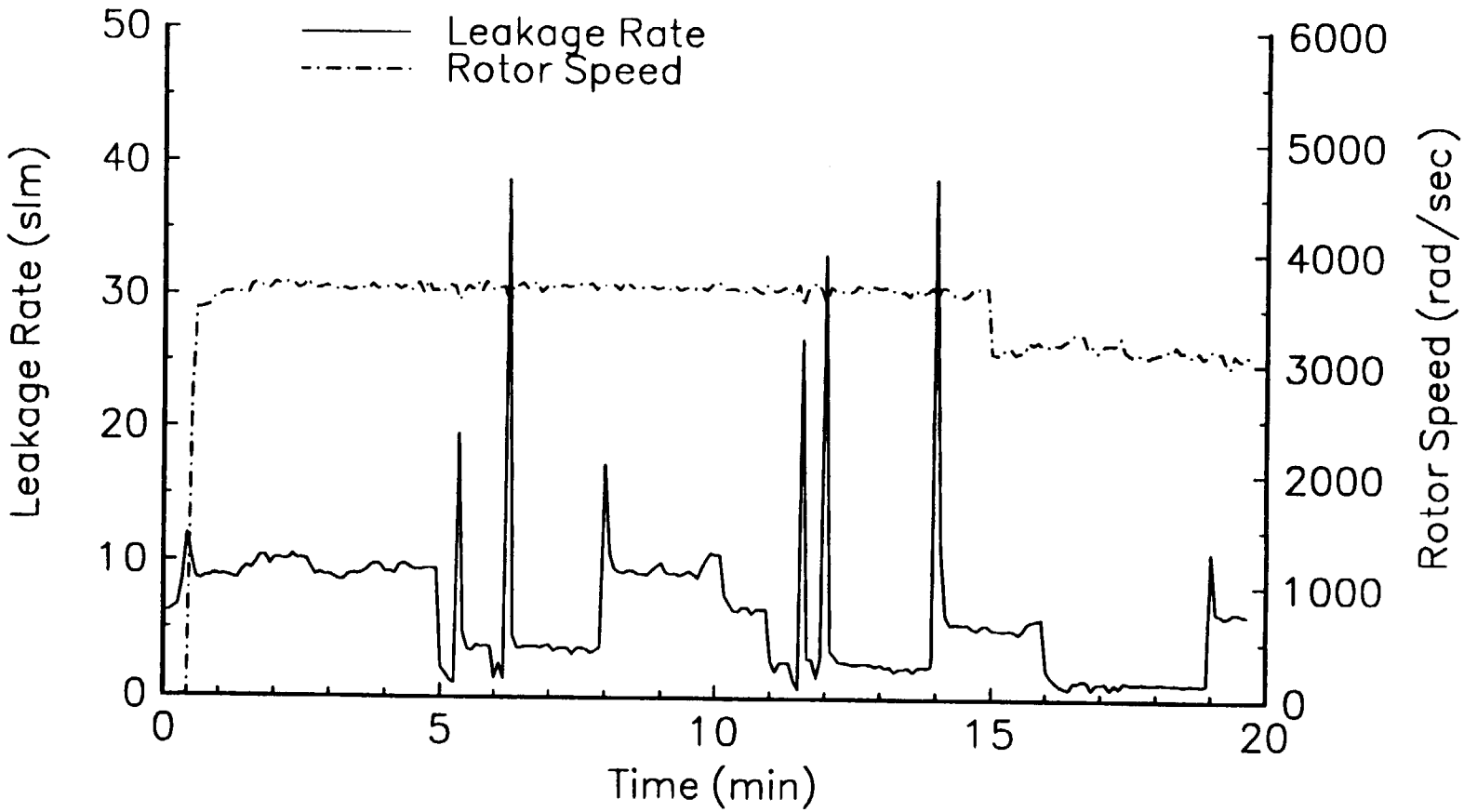

Figure 6-37. Seal Instabilities - Leakage Rate and Speed

CHAPTER VII

COMPARISON OF MATHEMATICAL MODEL WITH EXPERIMENTAL RESULTS

A mathematical model was utilized to evaluate various seal designs before the mechanical seal used in this study was built [Wolff, 1991]. It is useful to compare the mathematical model with the experimental results to evaluate the utility of the mathematical model as a design tool. Due to simplifications in the mathematical model (see Chapter III - Mathematical Model) and the configuration of the test rig (see Appendix A - Detailed Design Drawings), this comparison involved several simplifying assumptions. Therefore, it was not expected that the computational model would predict the leakage rates with a high level of accuracy. However, a mathematical model that can predict the trends in the leakage rate as a function of the seal geometry, and as a function of the operating conditions, is a useful design tool.

The simplifying assumptions in the mathematical model include hydrostatic load support, axisymmetric seal faces, linear elastic seal faces, and simplified thermal boundary conditions. These assumptions limit the complexity of the mathematical model such that a computational run can be made in a reasonable amount of time. An additional assumption made in interpreting the test data is that the seal leaks equally through both sealing interfaces. The double seal configuration provides two leakage paths for the gas while only one leakage rate was measured, the gas flow into the seal cavity. Measuring the flow rate from each side of the seal would have involved extensive modification of the test rig housing. Therefore, care was taken prior to each test such that the coning deformations versus voltage of each deformable face assembly were similar. This helped establish equal

leakage rates through both sides of the seal. The mathematical model computed the leakage rate from one side of the double seal. Therefore, the mathematical and experimental leakage rates presented below are half the total leakage rate of the double seal

The primary parameter of interest is the leakage rate of the seal, which strongly depends on the coning of the seal faces. Therefore, as a first comparison, the measured coning deformations are compared to the predicted coning deformations from the mathematical model. The measured leakage rate is then compared to the computed leakage rate for the steady state air and helium tests.

Coning of the Deformable Face Assembly

The coning of a deformable face assembly is presented in Figure 6-1. This figure demonstrates that a large amount of hysteresis is present in the coning versus voltage curve. However, over a smaller voltage range the hysteresis is reduced. Figure 7-1 compares the measured coning over the smaller voltage range to the coning predicted by the mathematical model. The material coefficients for the piezoelectric material were obtained from a commercial publication provided by a company that produces piezoelectric ceramics [Vernitron]. The slopes of the curves presented in Figure 7-1 match closely, however there is an offset of approximately 0.75 μm (29 μin) between them. The offset in coning is due to the hysteresis present in the coning deformation of the seal face, which is not accounted for in the mathematical model. This offset in coning is compensated for by introducing an initial coning in the carbon face of the mathematical model.

Figure 7-2 presents the predicted effects of pressure and thermal deformations on the coning of the deformable face assemblies. Four curves are presented, one with pressure

loading only and three different curves with pressure and thermal loading. The thermal loading is based on the runs that were used to model the steady state air tests at three different rotational speeds of 3770, 3140, and 2830 rad/sec (35,000, 30,000, and 27,000 rpm), at a cavity pressure of 1.34×10^6 Pa (180 psig). The computational runs for the steady state air tests include an initial coning to compensate for the initial offset in coning observed in Figure 7-1. This initial coning has been subtracted from the coning deformations presented in Figure 7-2.

Figure 7-2 demonstrates that the pressure loading decreases the coning deformation while the thermal deformations increase the coning deformation. The thermal deformations increase as the rotational speed increase. This is due to the increased viscous heat generation produced between the seal faces.

The thermal deformations computed by the mathematical model are strongly influenced by the thermal boundary conditions. The thermal boundary conditions were selected such that the computed face temperatures matched the experimental face temperatures (see Chapter III - Mathematical Model). Figures 7-3 and 7-4 compare the computed face temperatures to the experimental temperatures for the air and helium tests, respectively. For the decreasing portion of the temperature curves, the computed temperatures match the experimental temperatures within about 5 °C. For the increasing portion of the temperature curves, the seal faces have not reached a steady state condition and agreement is not as good.

Figure 7-3 also compares two different means to model the thermal boundary conditions. One of the curves uses an average measured cavity temperature (46 °C) to model the bulk temperature of the fluid, while the convective coefficient and initial coning were adjusted such that the computed faced temperatures matched the experimental face temperatures. The convective coefficient and initial coning for this curve are 40 $W/m^2{}^oC$

and 1.25 μm, respectively. The second curve is based on adjusting each of the three variables (bulk temperature, convective coefficient, and initiial coning) to match the experimental data. The bulk temperature, convective coefficient, and initial coning for this curve are 35 °C, 15 W/m^2°C, and 0.9 μm, respectively. Adjusting each of the three variable produces a better match to the experimentally measured face temperature, therefore the latter method was used in all subsequent computations, including those of Figure 7-4. For the mathematical model presented in Figure 7-4, the bulk temperature, convective coefficient, and initial coning are 27 °C, 5 W/m^2°C and 0.15 μm, respectively.

Comparison of Leakage Rates

In this section, leakage rates predicted by the mathematical model are compared to the experimental leakage rates. Leakage rates could be interpreted in terms of film thickness by noting that once the seal geometry and sealed pressures are specified, the film thickness can be determined from leakage rate (see Equation 3-17). Figure 7-5 presents half the leakage rate as a function of film thickness for the air and helium tests. This figure demonstrates that leakage rates from 2-10 slm correspond to film thicknesses from 3-5 μm.

Figures 7-6 through 7-9 compare the leakage rates from the mathematical model to half the leakage rates measured during the steady state air tests. These comparisons are performed for three different rotational speeds (3770, 3140, and 2830 rad/sec), and for two different sealed pressures (1.34 x 10^6 and 6.48 x 10^5 Pa). The balance ratio for these tests was 0.766. For the following comparison, the initial coning, convective coefficient, and bulk temperature were set to 0.15 μm, 5 W/m^2°C, and 27 °C, respectively..

Figure 7-6 compares the experimental results to the mathematical model for a rotational speed of 3770 rad/sec and a sealed pressure of 1.34 x 10^6 Pa. For this test, the

mathematical model predicts the magnitude and range of half the leakage rate reasonably well. The mathematical model predicts the leakage rate to vary from 2.4 to 6.4 slm as the voltage is increased from 0 to 3000 V while the measured leakage rate varies from 2 to approximately 8.5 slm.

The experimental leakage rate exhibits a significant amount of hysteresis. The arrows on the leakage rate curve indicate the voltage loading sequence for this test; the voltage is initially 3000 V, decreased to 0 V, and then increased to 3000 V. No hysteresis is present in the leakage rate curves from the mathematical model because it is based on a linear elastic model.

Figures 7-7 and 7-8 compare half the experimental leakage rates to the mathematical model for reduced rotational speeds of 3140, and 2830 rad/sec, respectively. The range of leakage rates predicted by the mathematical model compare reasonably well with those from the tests. Both the mathematical model and the test data demonstrate that as the rotational speed decreases, the leakage rate generally decreases. This can be partly attributed to the decreased viscous heat generation, that results in a reduced amount of coning produced by thermal deformations. However, at the lower voltage levels, the mathematical model differs from the test data, and this difference increases as the rotational speed decreases. For all three rotational speeds, the leakage rate from the test data is approximately 2 slm. The mathematical model, predicts that the leakage rate should decrease as the rotational speed decreases for all voltage levels. The constant leakage rate of 2 slm at 0 V for the test data could indicate that another load support mechanism was present such as a hydrodynamic effect or partially contacting seal faces.

Figure 7-9 compares half the leakage rate from the experimental and mathematical model for a reduced pressure of 6.48×10^5 Pa, at a rotational speed of 3770 rad/sec. Both the mathematical model, and the test data, demonstrate that the leakage rate and the range

of the leakage rate decrease as the pressured decreases. There is an offset between the two curves, which increases with increasing voltage. This offset could be due to errors in the closing force, or errors in the predicted coning deformation.

Figures 7-10 through 7-12 compare the leakage rates from the mathematical model to half the leakage rates measured during the steady state helium tests. These comparisons are performed for three different rotational speeds (3665, 3240, and 2830 rad/sec), respectively. For these comparisons, the initial coning, convective heat transfer coefficient, and bulk temperature were set to 0.9 μm, 15 $W/m^2°C$, and 35 °C, respectively The balance ratio for these tests was 0.748.

Figures 7-10 through 7-12 show that the leakage rates predicted by the mathematical model are significantly lower than the experimental leakage rates. Factors that could produce this difference are the sensitivity of the seal design to slight changes in the coning deformation and closing force, and hydrodynamic effects, which the mathematical model ignores. The seal was designed such that small changes in coning produced relatively large changes in leakage rate (see Chapter IV - Seal Design). This also causes the film thickness (and leakage rate) to be sensitive to slight errors in the coning deformation and closing force used in the mathematical model.

Figure 7-1 demonstrates that there is a large amount of hysteresis present in the coning deformations. The slope of this curve varies, depending on the voltage level and the voltage loading sequence. The experimental data indicates that the leakage rate increases more than what is predicted as the voltage is increased. This could be a result of the seal face operating on a portion of the coning deformation curve that has a larger slope.

Errors in the closing force could also produce errors in the leakage rate. For the seal design used in the helium tests, a one percent decrease in closing force could increase the

leakage rate by as much as 40 percent. These deviations in the closing force could be produced by tolerances in the seal geometry, tolerances in the spring force, measurement errors in the sealed pressure, and forces produced by the O-rings.

A comparison of the data from the steady state air tests to the steady state helium tests indicate that the leakage rates are higher for the helium tests. This trend is predicted by the mathematical model and is partly due to the lower balance ratio for the helium steady state tests, which causes the film thickness (and leakage rate) to be more sensitive to changes in the coning.

Figure 7-13 compares the leakage rate from the mathematical model to the test data for the steady state helium test, at a reduced pressure of 7.91×10^5 Pa, and at a rotational speed of 3240 rad/sec. The mathematical model predicts the decreased leakage rate and the decreased range of leakage rates reasonably well for this test. However, the experimental leakage rate is significantly higher than the leakage rate from the mathematical model at the higher voltage levels.

The comparisons between the test data and mathematical model demonstrate that the mathematical model is successful in predicting trends that occur with the test data. The mathematical model is successful in predicting the decreased leakage rate as the rotational speed decreases, as the sealed pressure decreases, and as the balance ratio increases. However, the mathematical model does not predict the actual leakage rate with a high degree of accuracy. This is not unexpected, given the number of idealizations used in modeling the system.

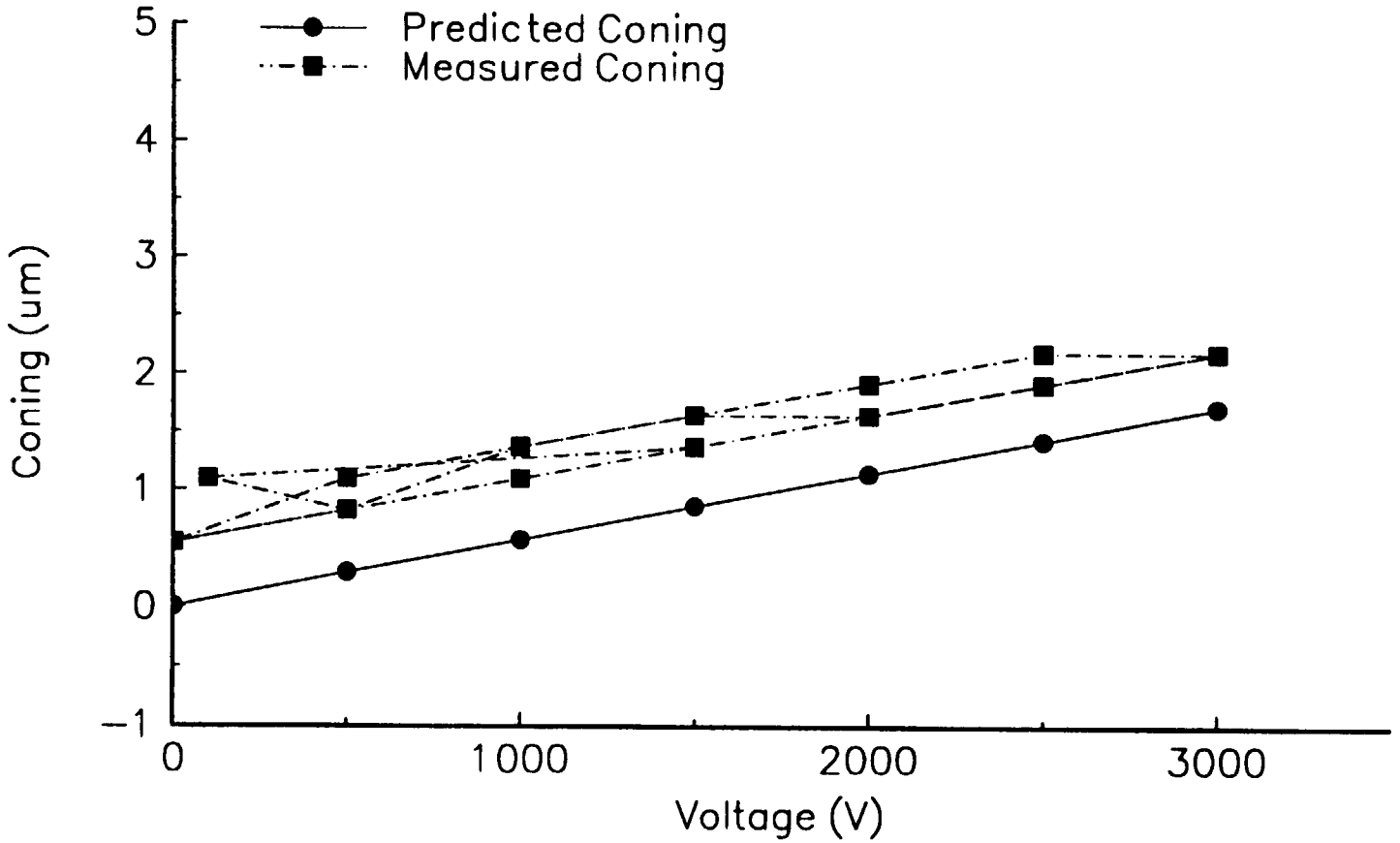

Figure 7-1. Predicted versus Measured Coning

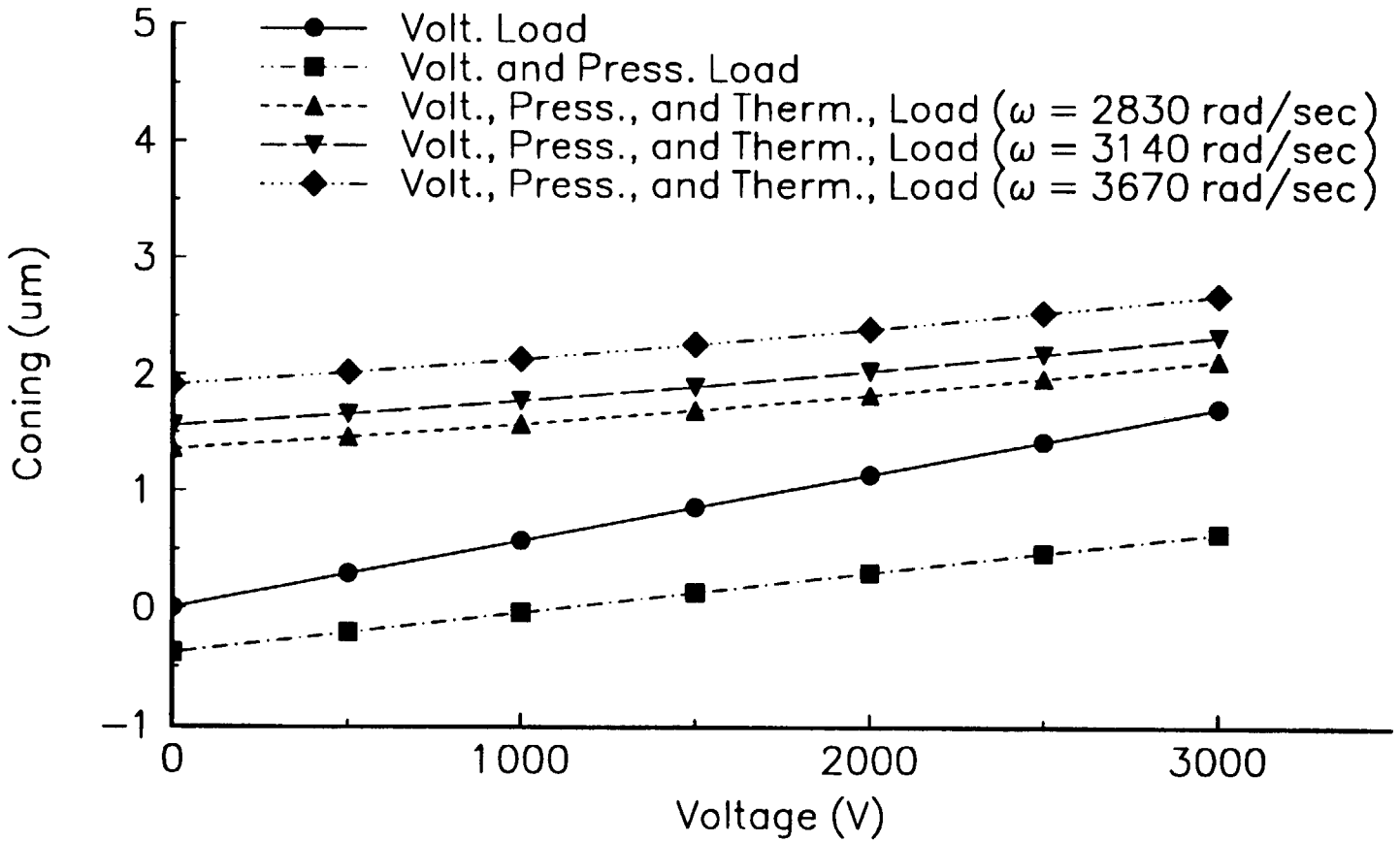

Figure 7-2. Predicted Coning - Effects of Pressure and Thermal Loading

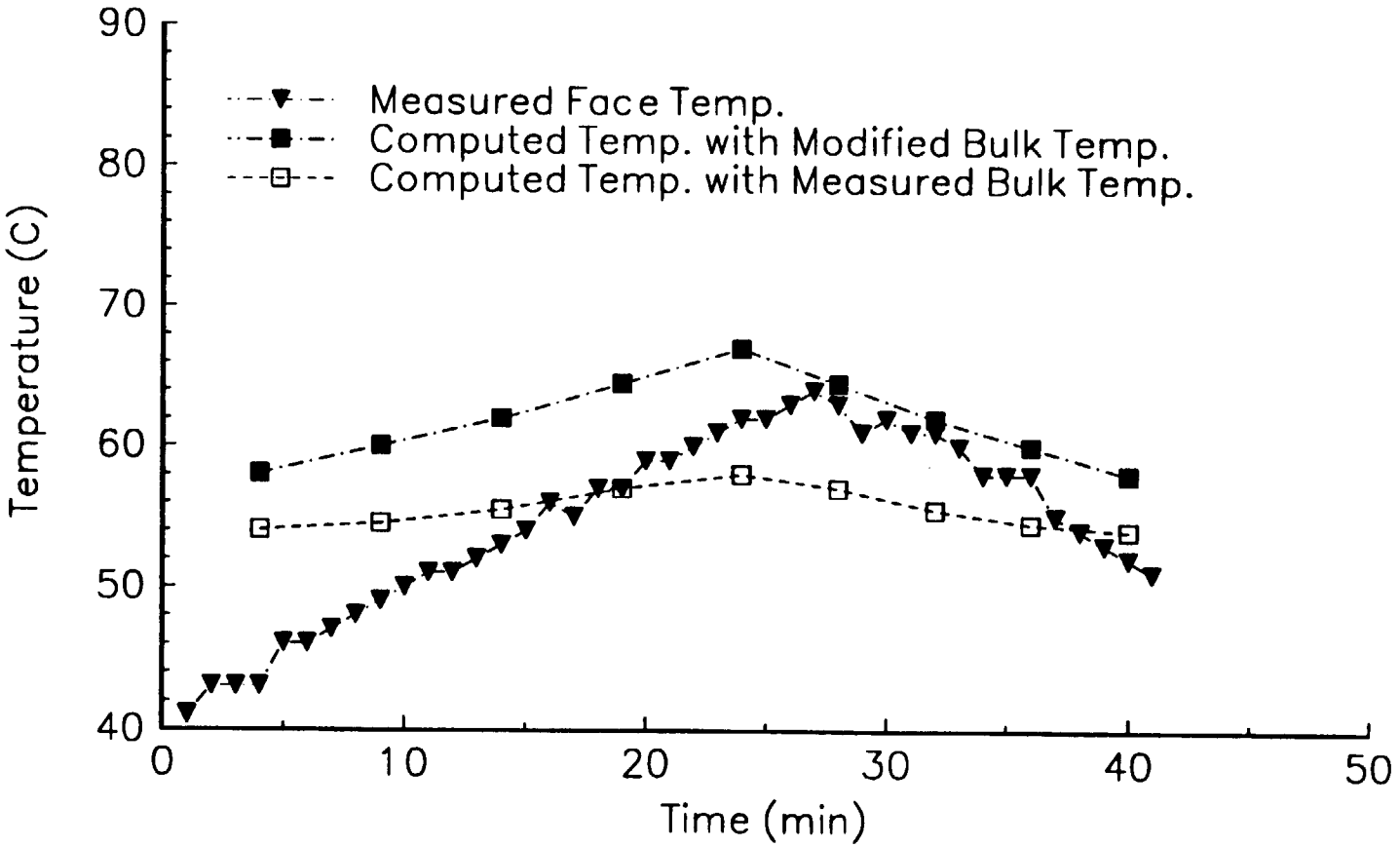

Figure 7-3. Predicted versus Measured Face Temperature - Helium Test

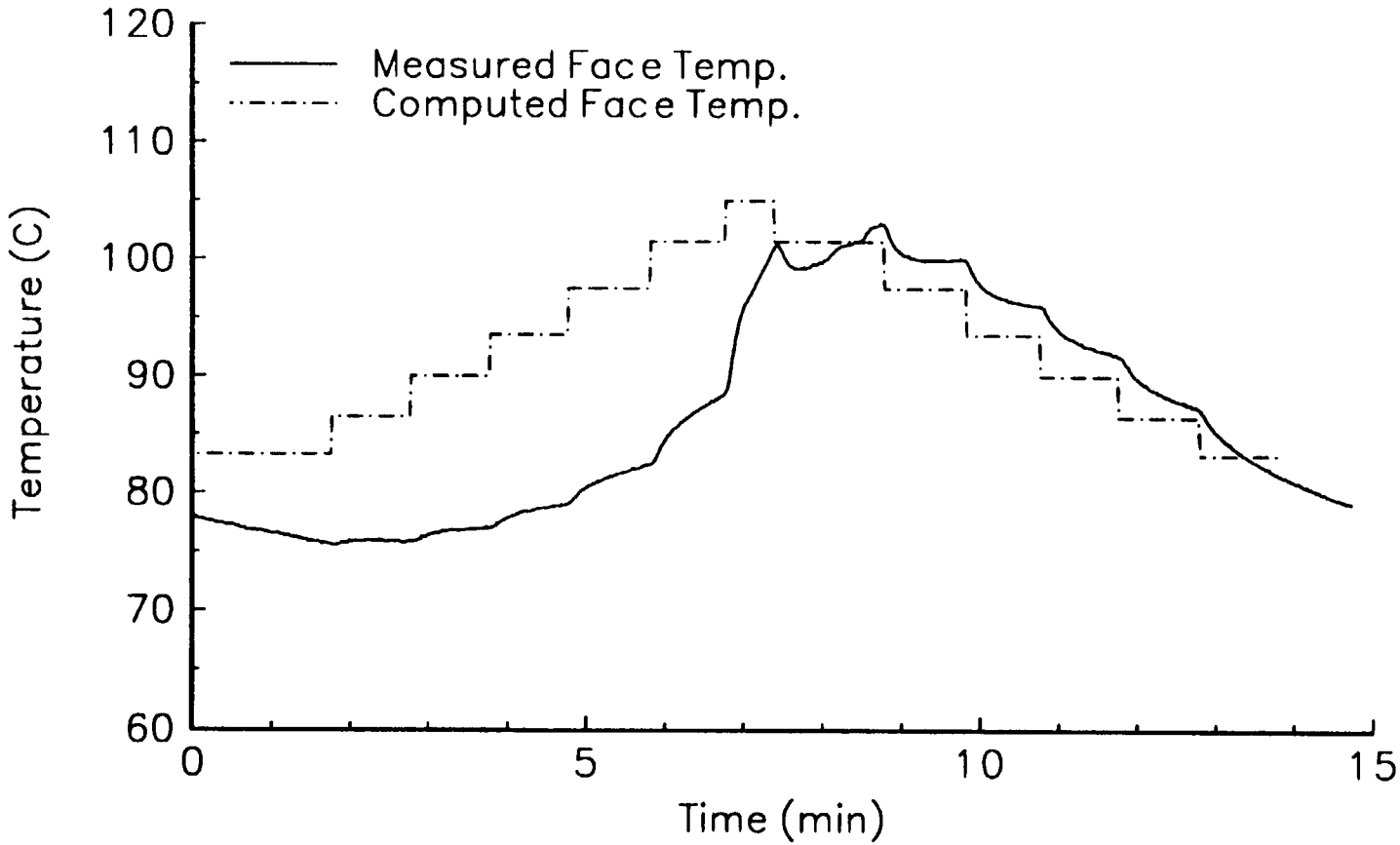

Figure 7-4. Predicted versus Measured Face Temperature - Air Test

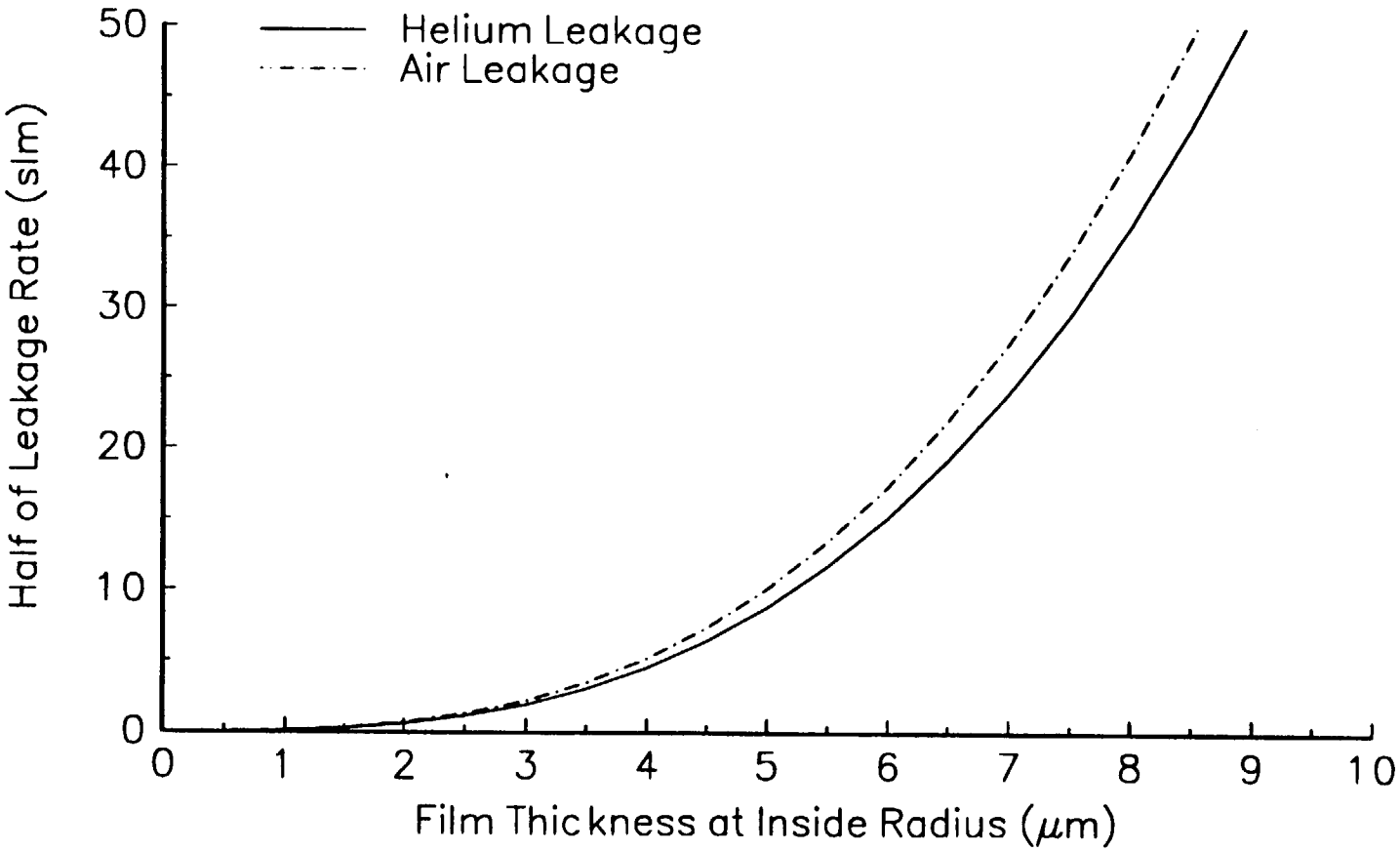

Figure 7-5. Leakage Rate versus Film Thickness

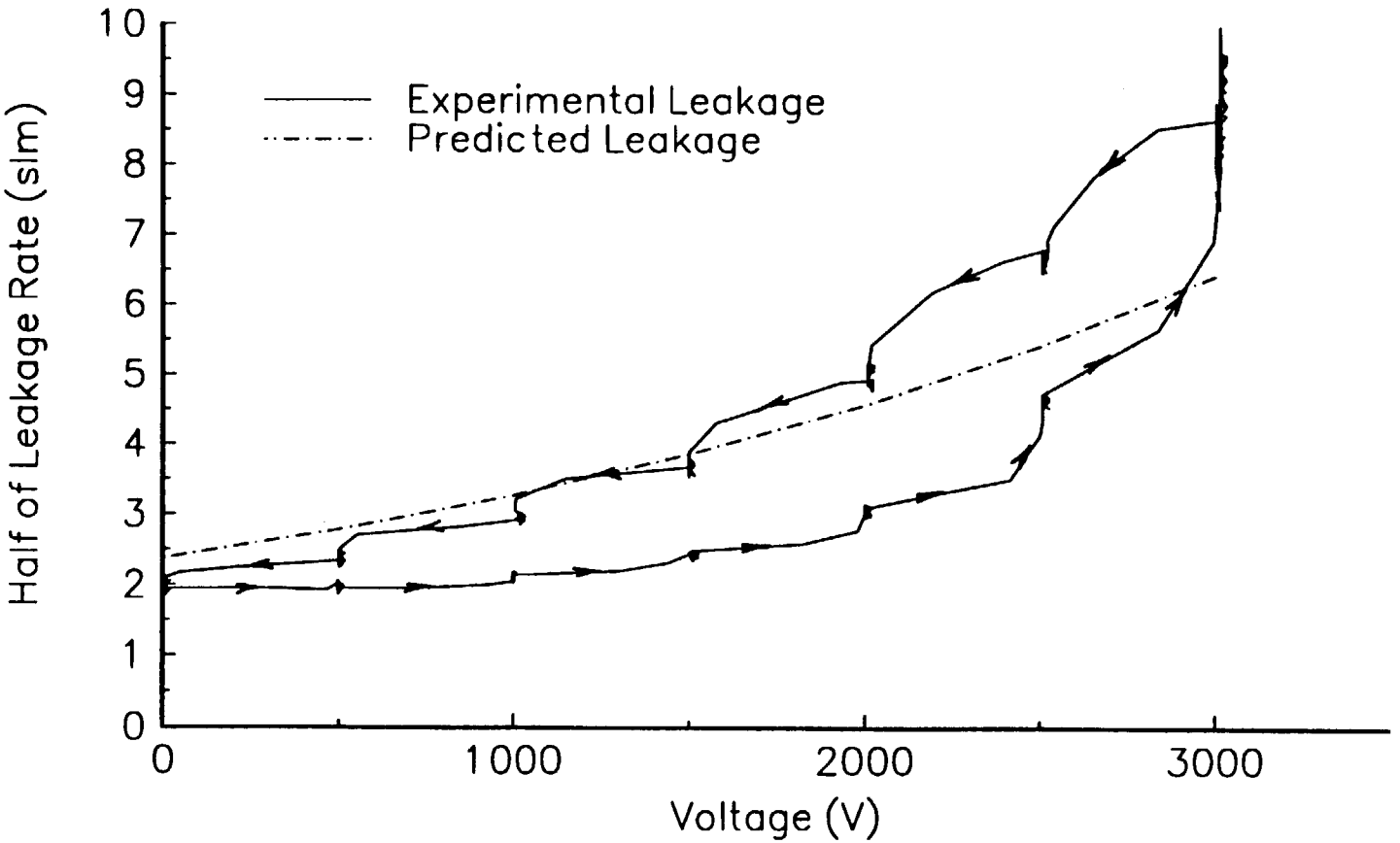

Figure 7-6. Predicted versus Measured Leakage Rate - Air Test
($P = 1.34 \times 10^6$ Pa, $\omega = 3770$ rad/sec)

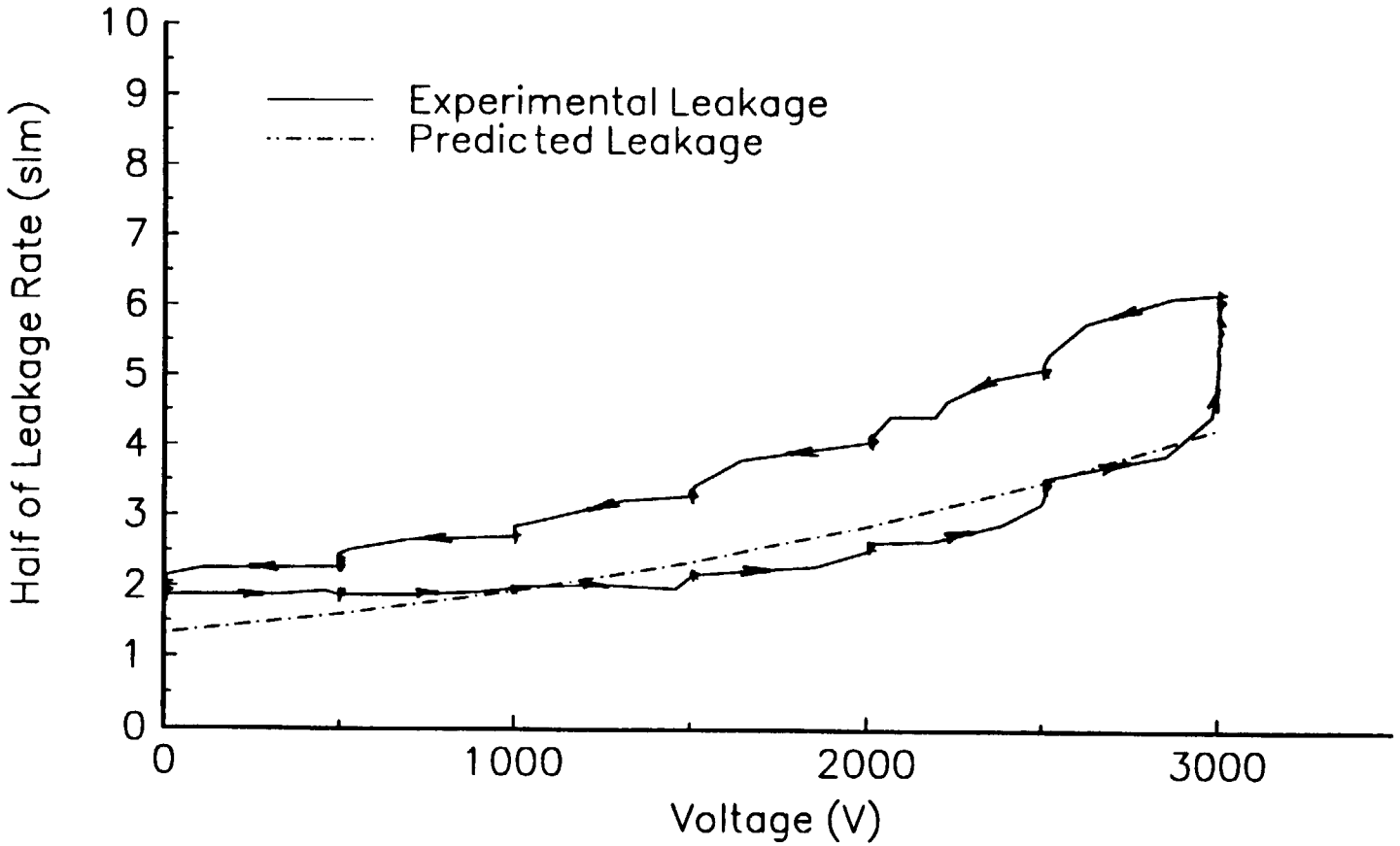

Figure 7-7. Predicted versus Measured Leakage Rate - Air Test
($P = 1.34 \times 10^6$ Pa, $\omega = 3140$ rad/sec)

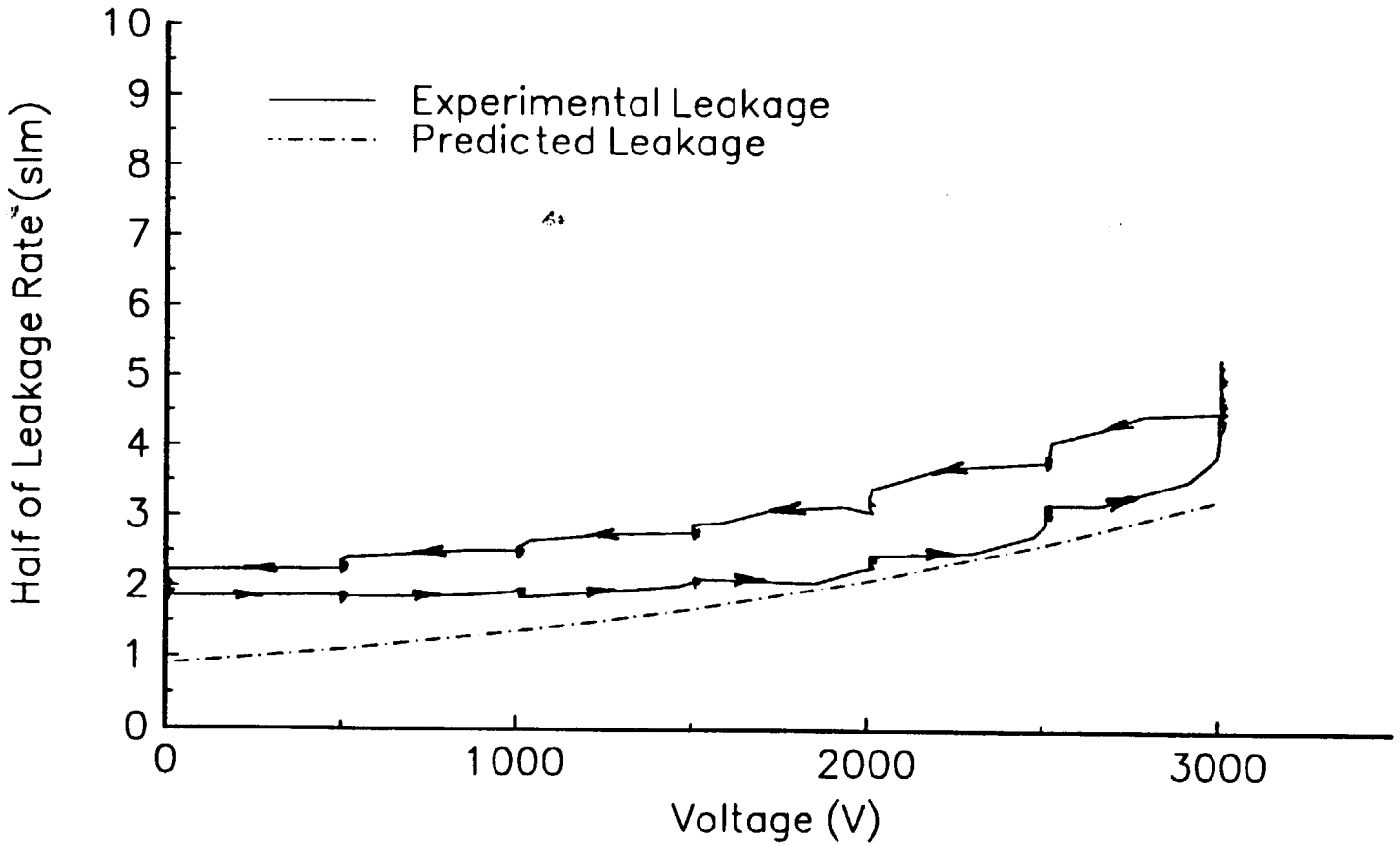

Figure 7-8. Predicted versus Measured Leakage Rate - Air Test
($P = 1.34 \times 10^6$ Pa, $\omega = 2830$ rad/sec)

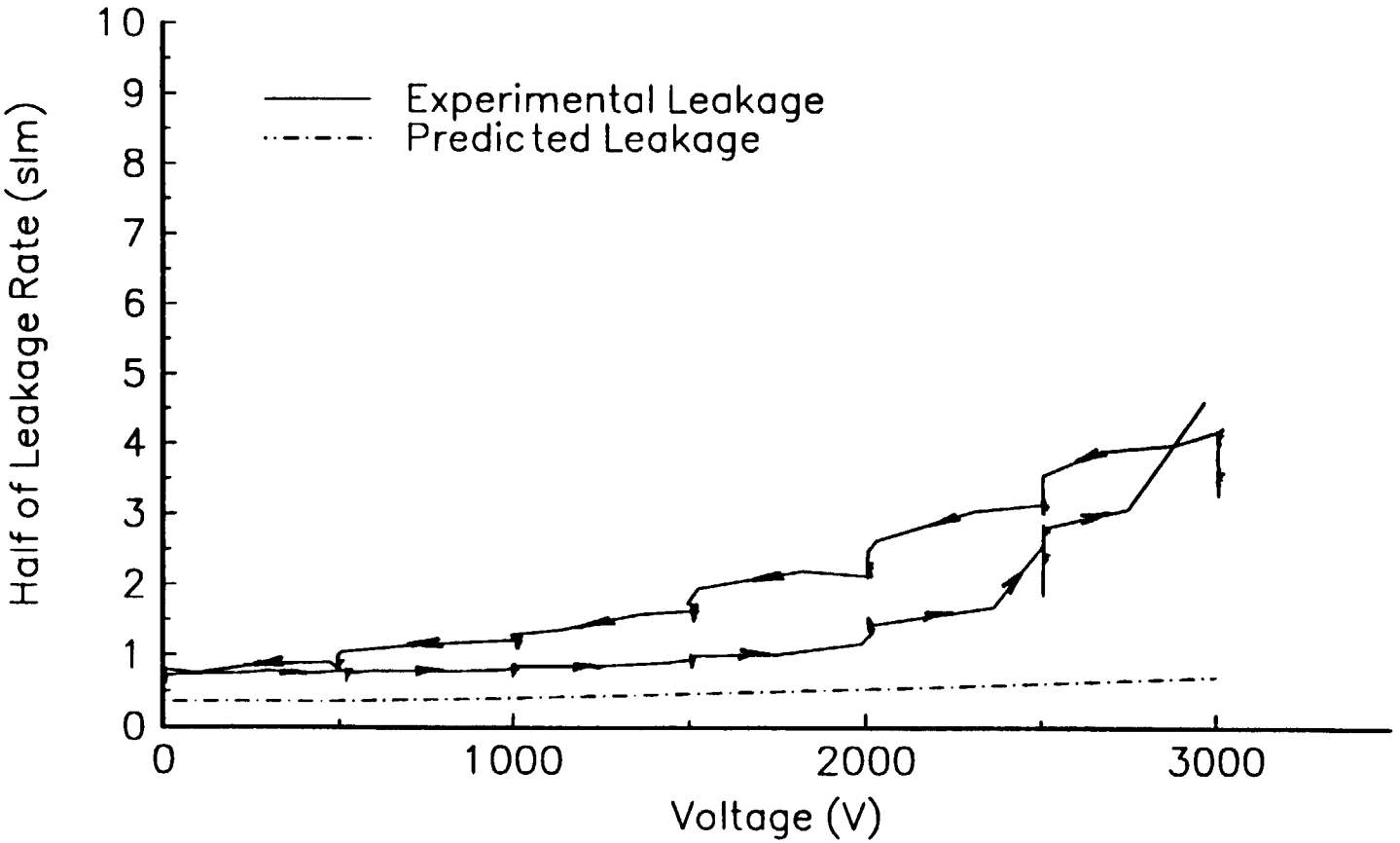

Figure 7-9. Predicted versus Measured Leakage Rate - Air Test
($P = 6.48 \times 10^5$ Pa, $\omega = 3770$ rad/sec)

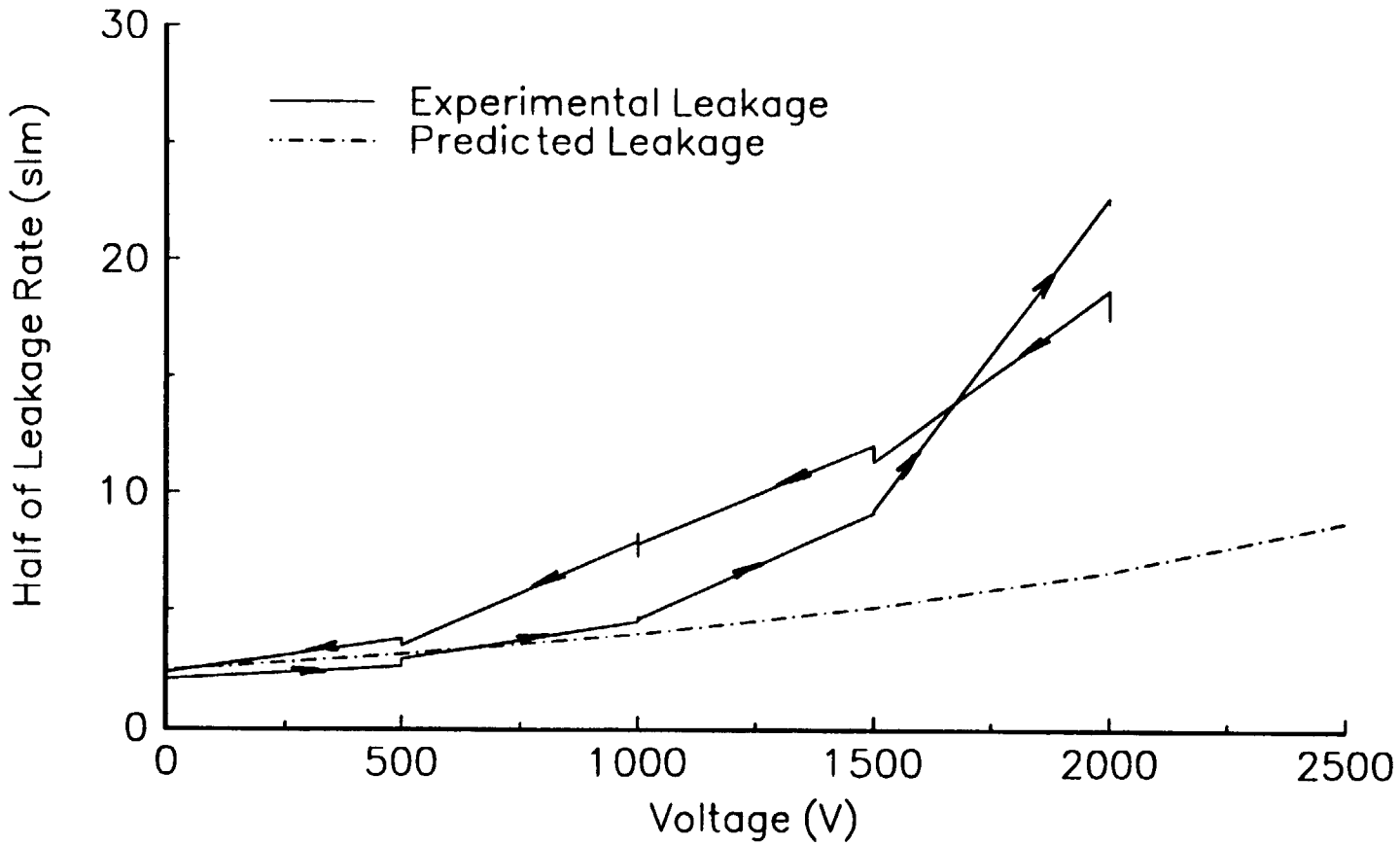

Figure 7-10. Predicted versus Measured Leakage Rate - Helium Test ($P = 1.48 \times 10^6$ Pa, $\omega = 3770$ rad/sec)

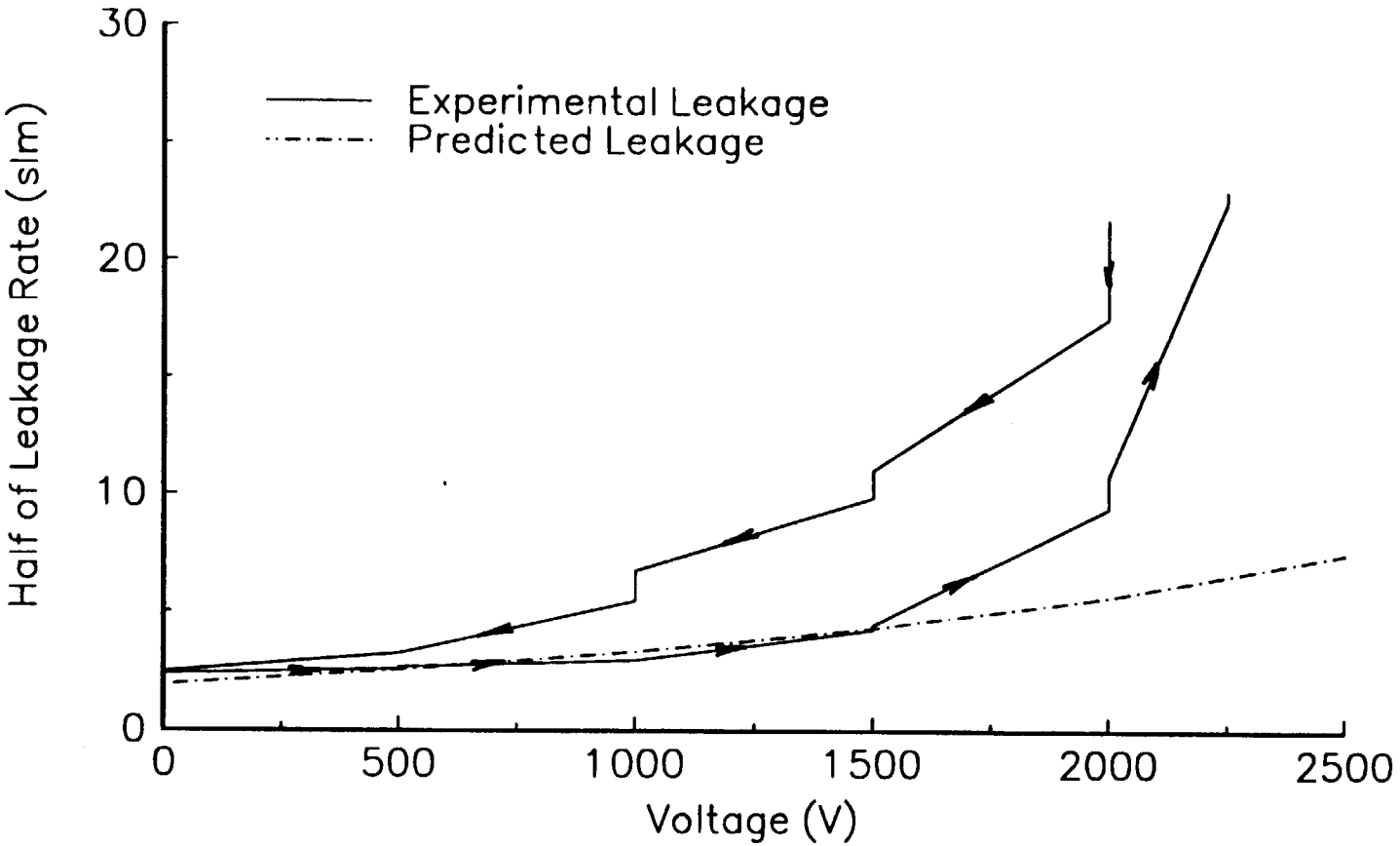

Figure 7-11. Predicted versus Measured Leakage Rate - Helium Test ($P = 1.48 \times 10^6$ Pa, $\omega = 3240$ rad/sec)

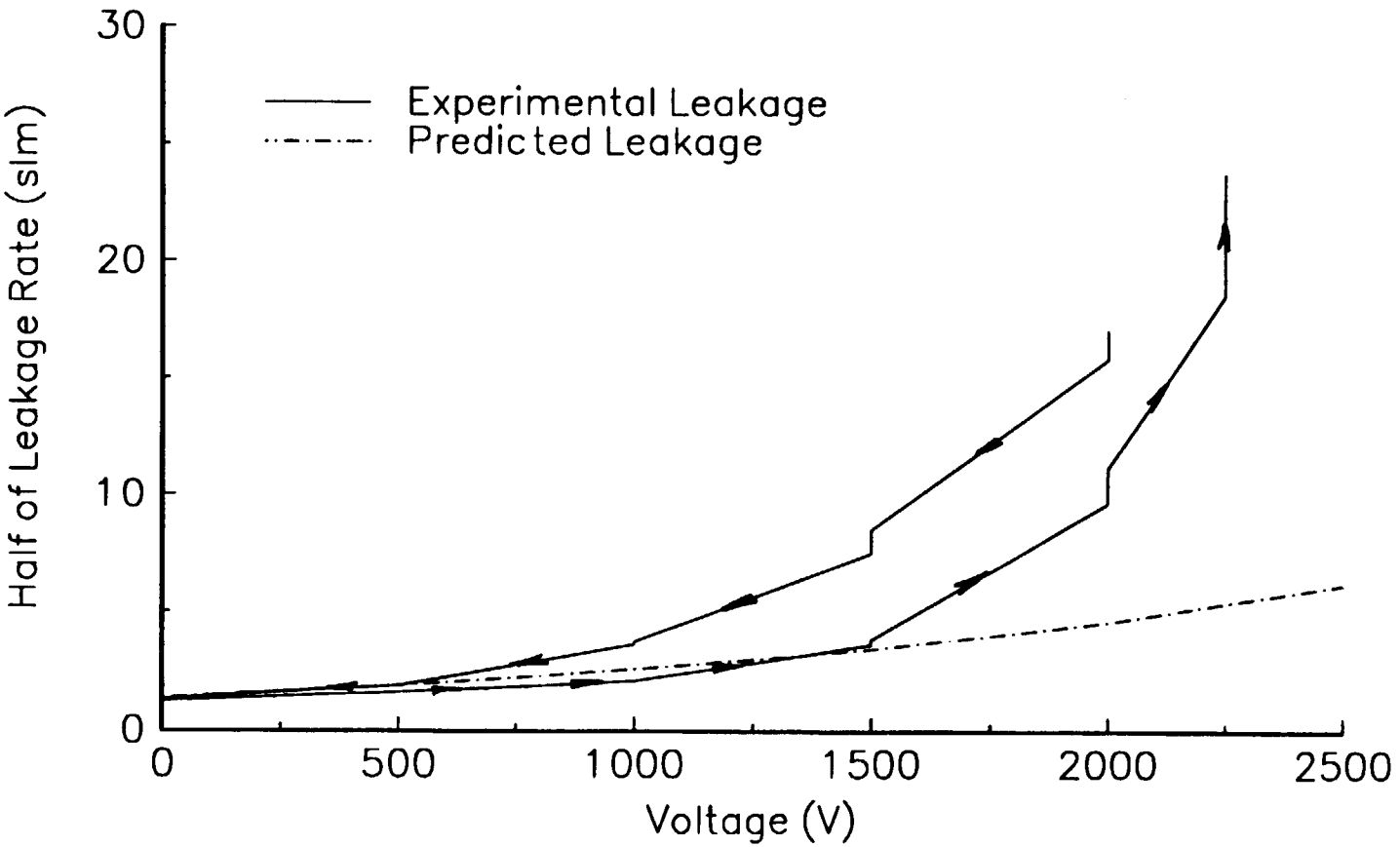

Figure 7-12. Predicted versus Measured Leakage Rate - Helium Test ($P = 1.48 \times 10^6$ Pa, $\omega = 2830$ rad/sec)

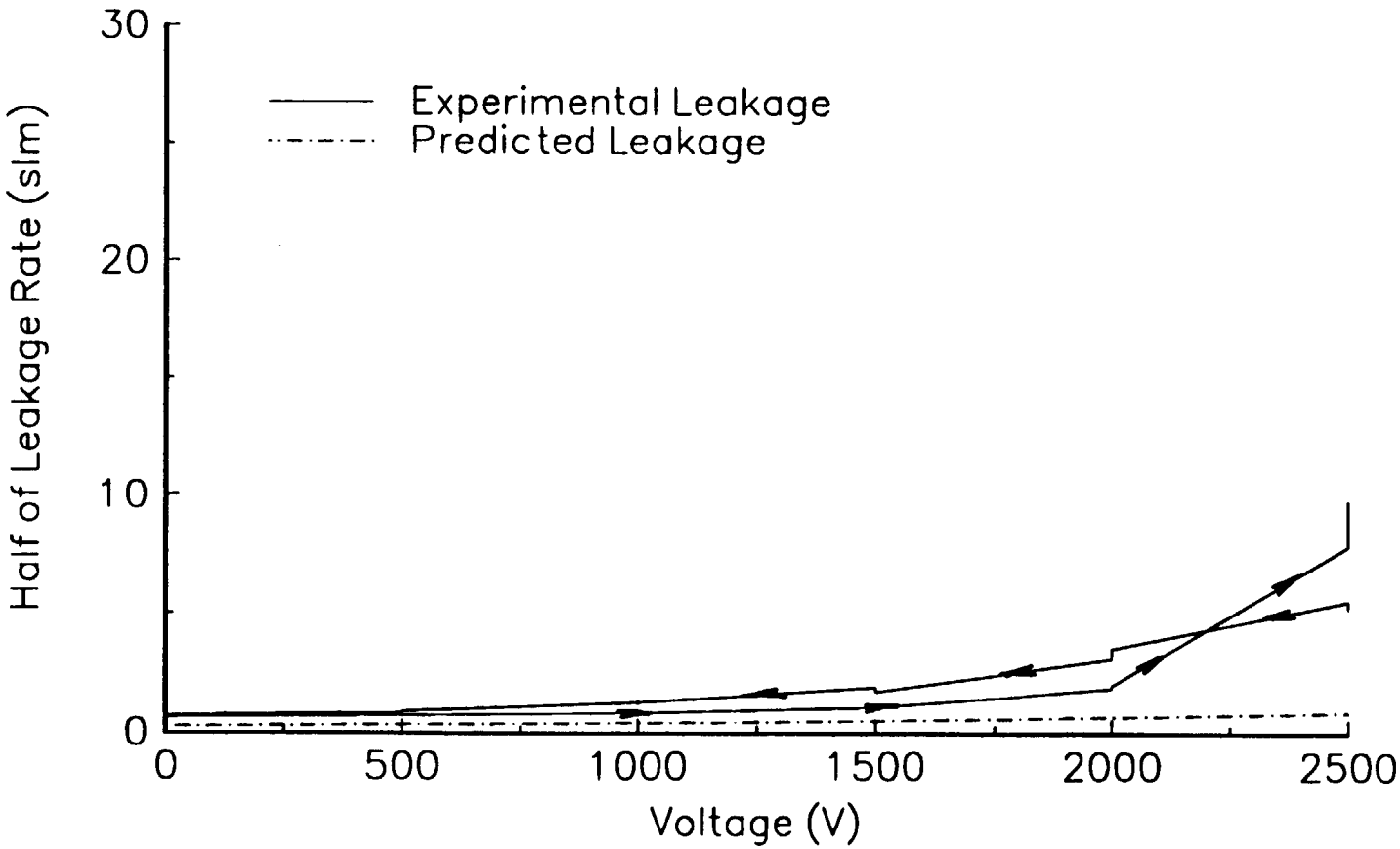

Figure 7-13. Predicted versus Measured Leakage Rate - Helium Test ($P = 7.91 \times 10^5$ Pa, $\omega = 3240$ rad/sec)

CHAPTER VIII

CONCLUSIONS AND RECOMMENDATIONS

An actively controlled mechanical seal was designed, fabricated, and tested in a laboratory test rig. The design phase included developing a mathematical model to predict the performance of the seal. The results from these tests and the mathematical model provide valuable design information for the next development stage for actively controlled mechanical seals.

The results from this study demonstrate that an actively controlled mechanical seal operating in a gas environment is feasible. The seal operated successfully with low leakage rates during steady state tests, short term transient tests, and longer term transient tests. Low leakage rates were maintained while preventing excessive face contact as indicated by face temperatures and surface profiles.

The mathematical model developed for this study provided valuable design information for the development of this seal. Design curves were developed that present the controllability, stiffness, and viscous heat generation as a function of the closing force. With these curves, the seal geometry and spring force can be specified to maximize controllability and stiffness, while minimizing viscous heat generation. Once the closing force was specified, finite element models were utilized to determine the leakage rates and temperatures of the seal while operating at various sealed pressures and rotational speeds. The model proved successful in predicting trends that occurred with the leakage rate as a function of the voltage applied to the seal, as the sealed pressure was changed, and as the balance ratio was increased. However, the model was less successful in accurately

predicting the magnitude of the leakage rate that occurred during the various operating conditions.

The two main problems encountered during these tests included electrical breakdown while the seal was operated in a helium environment, and dynamic instabilities. There are various means in which the electrical breakdown problem can be addressed. One technique is to isolate the piezoelectric element from the helium. This could be accomplished by fabricating a holder from a material that is electrically insulative, that encloses the piezoelectric element at the outside, and inside radii. The piezoelectric element could then be bonded in this holder with a sealing compound. The sealing compound must be resilient enough such that it does not constrain the coning deformations produced by the piezoelectric element. Another way in which the piezoelectric element could be isolated from the helium is with a nonconductive coating. There are coating materials commercially available, commonly referred to as conformal coatings, that are designed to produce a thin uniform coat. In applying these coatings, great care must be taken to ensure that no part of the piezoelectric element is left uncoated. Small breaks in the coating could promote electrical breakdown. Electrical breakdown could be further prevented by using the aforementioned insulation techniques in conjunction with using a different buffer gas. Helium has a particularly low dielectric strength and is not well suited for use with an actively controlled mechanical seal that requires high operating voltages.

Another design choice that would eliminate electrical breakdown is to use a different type of actuator to produce the coning deformations. One such choice, is to use a hydraulic actuator to produce the coning deformations. A challenge in developing different types of actuators is to design them such that they can produce a large enough

range of coning while limiting their size such that they can fit in the seal envelope. In addition, the associated hardware that drives the actuator must not be too cumbersome.

An additional problem that occurred during the seal tests was dynamic instability at the higher rotational speeds. To address this problem, one must consider the entire dynamical system comprised by the seal, the rotor, the shaft, and the bearings. Each of these components could have manufacturing or assembly tolerances that could produce excessive runout between the seal faces. Great care must therefore be taken to minimize these runouts.

One of the means in which the runout in the seal of the present study could be reduced is to bond the deformable face assembly in the holder. The carbon face should then be remachined such that the back side of the holder, and the seal face are as near parallel as possible. In the current design, these components were fabricated separately, and the runouts in both assemblies could combine to produce excessive runout.

Once these problems are solved, there is a significant amount of work that must be performed before the actively controlled seal can be utilized in a liquid oxygen turbopump. The seal must be redesigned to withstand the extreme temperatures that occur in a liquid oxygen turbopump. For example, elastomeric O-rings were used during this study and these must be replaced with a different type of secondary seal before this seal can be operated at higher (and lower) temperatures. Metal bellows seals might be a design choice.

A basic, P.I.D. controller was used for the closed-loop control system in this study. Other control algorithms should be investigated to determine which method is best suited for the actual operating conditions.

The components of the control system that are exterior to the liquid oxygen turbopump must be made much more compact and hardened to withstand a harsher

operating environment. These components include the high voltage power supply, the data acquisition system, and the computer.

Additional sealing areas should also be identified in which the cost of an actively controlled gas seal would be justifiable. In light of stricter environmental regulations, where the allowed leakage rates are becoming smaller, actively controlled mechanical seals could be a promising technology due to their low leakage rate, and high reliability.

APPENDIX A

DETAILED DESIGN DRAWINGS

The detailed design drawings of the seal components and the seal housing are presented in this appendix. All dimensions shown are in millimeters.

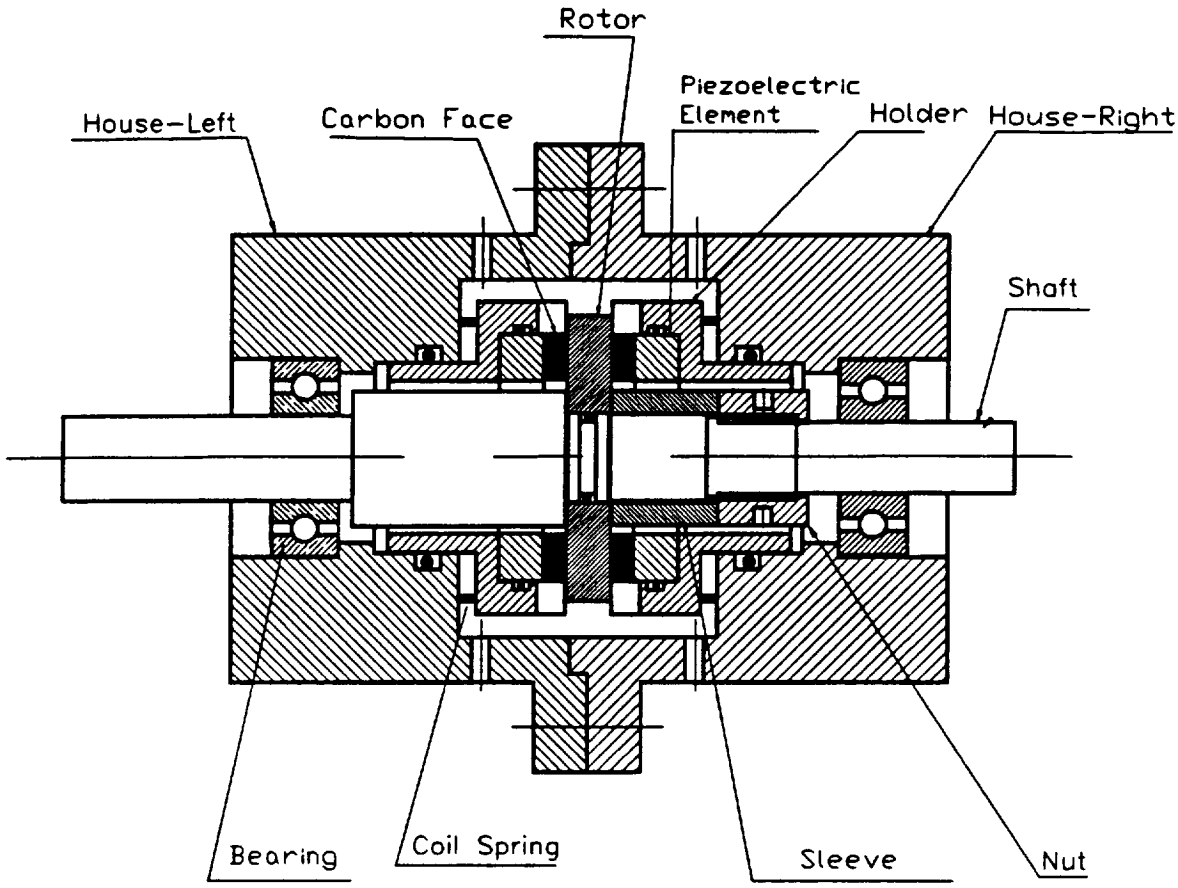

Figure A-1. Assembly Drawing

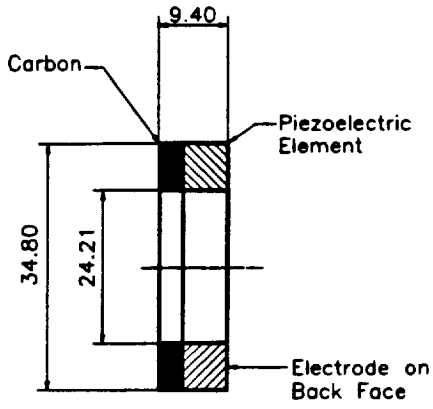

Section A–A

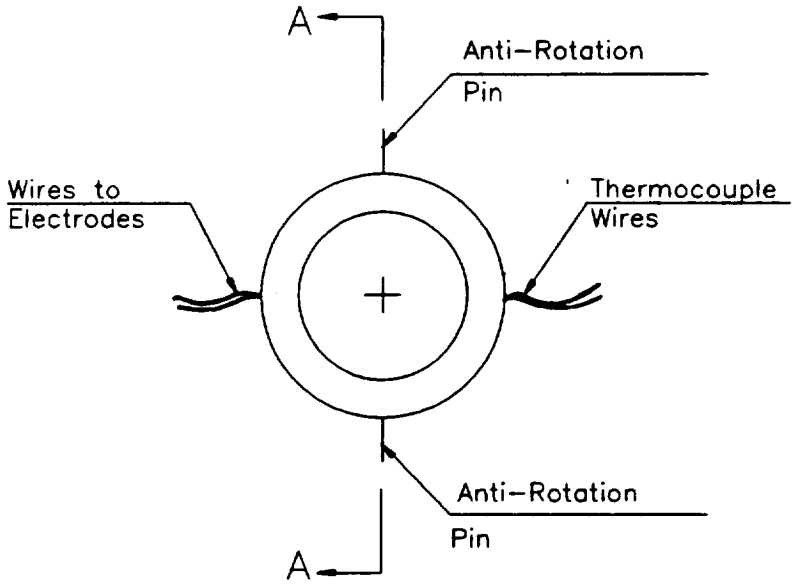

Figure A-2. Deformable Face Assembly

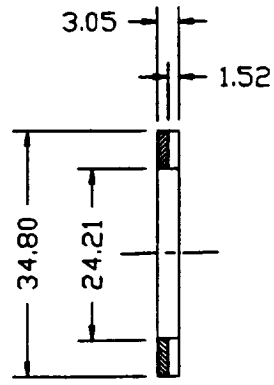

Section A-A

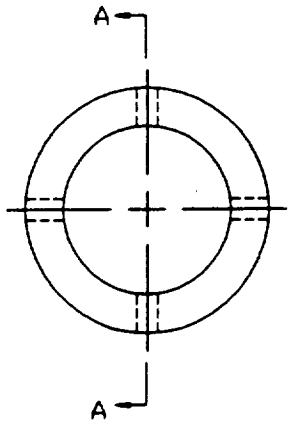

Figure A-3. Carbon Face

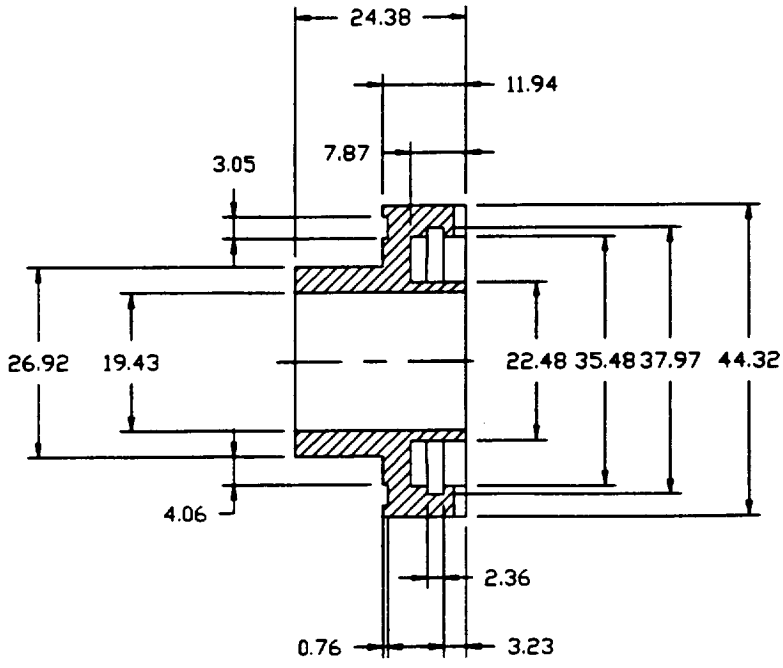

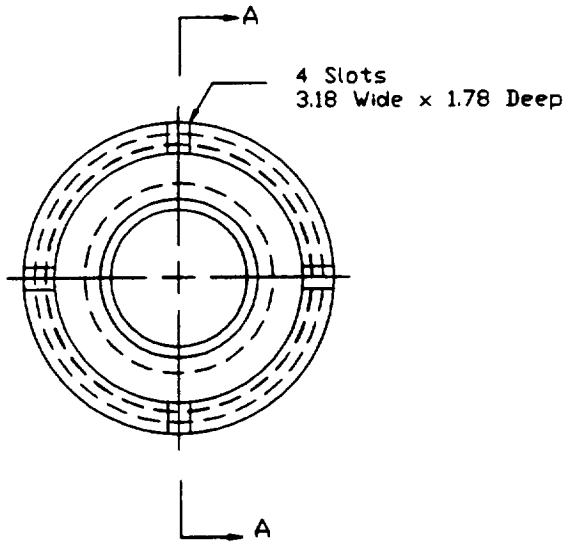

Figure A-4. Holder

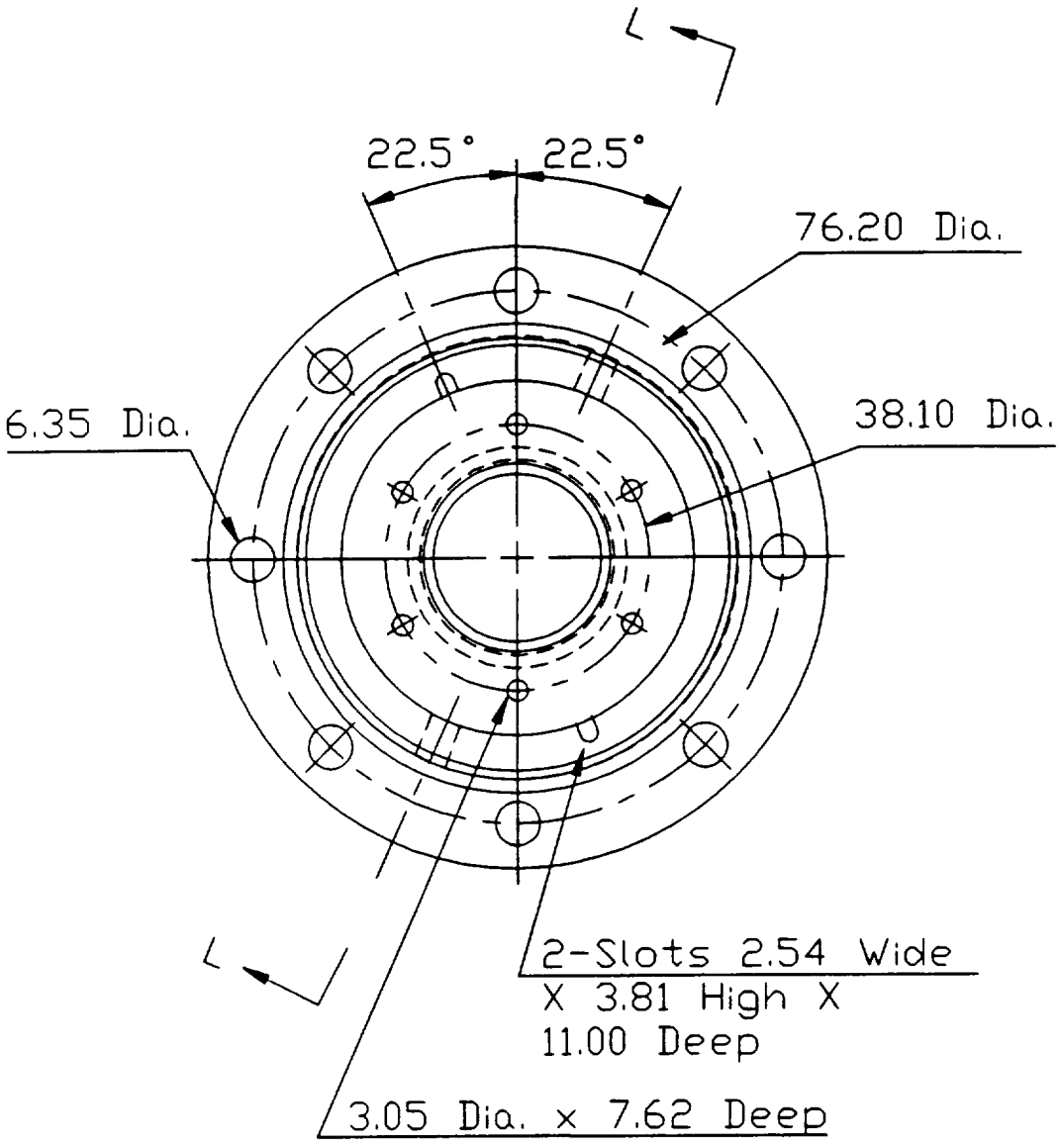

Figure A-5. Left Housing - Front View

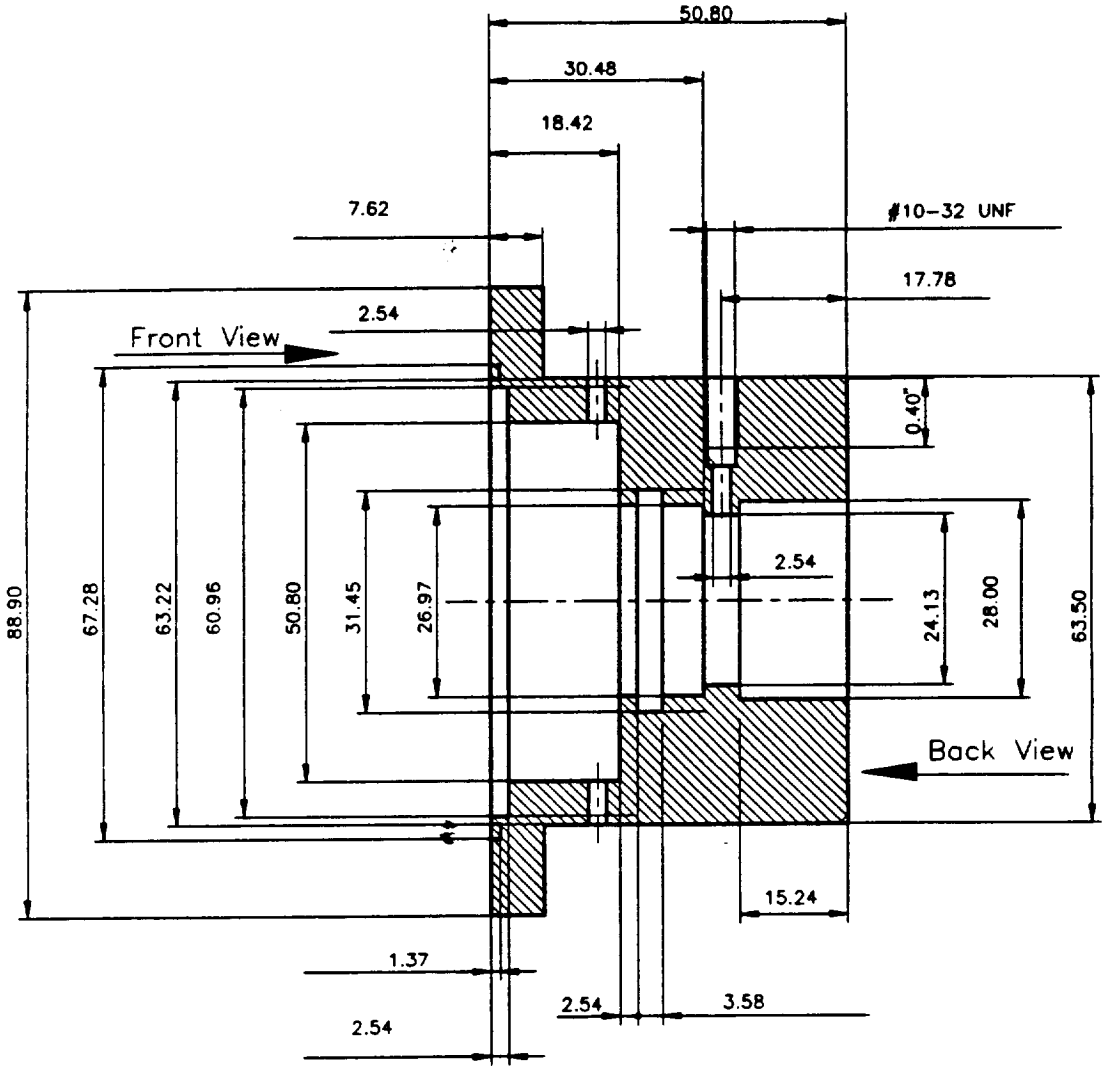

Figure A-6. Left Housing - Cross Section

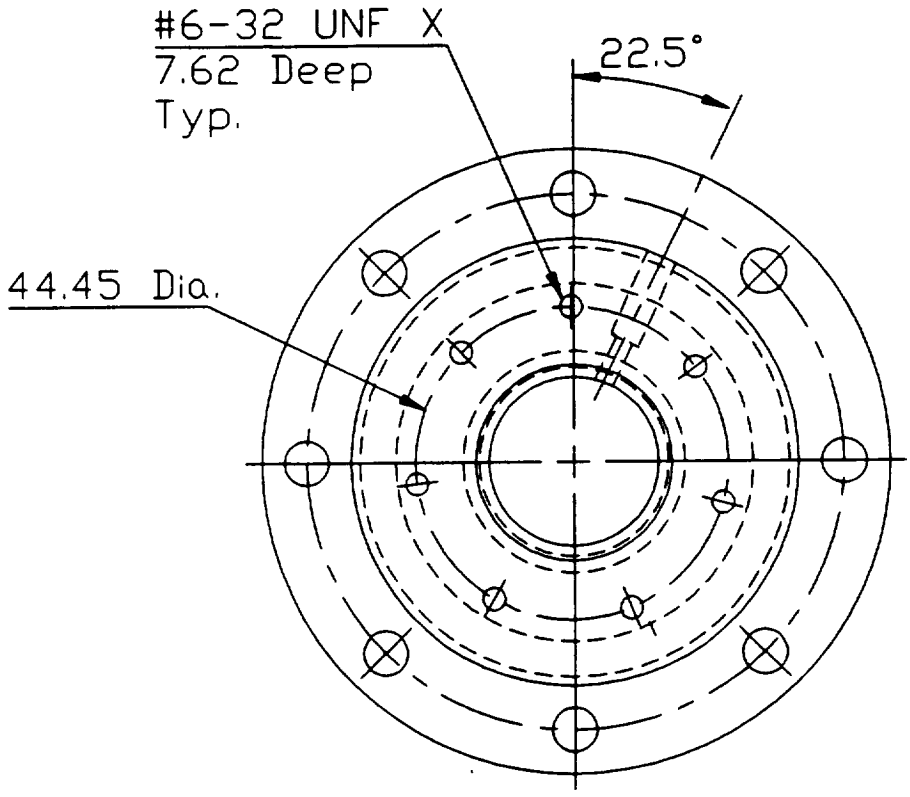

Figure A-7. Left Housing - Back View

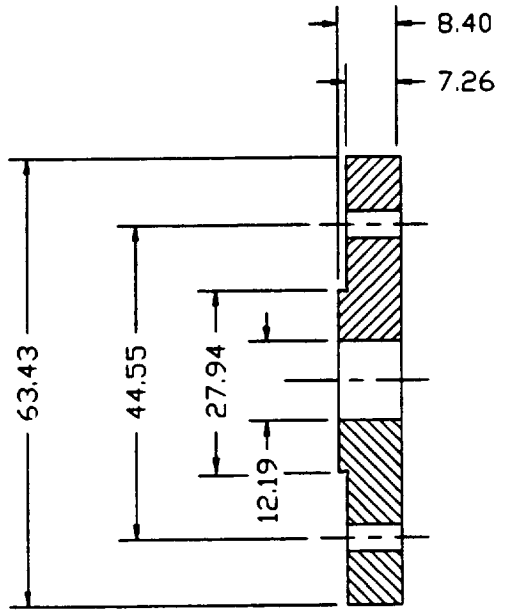

Section A-A

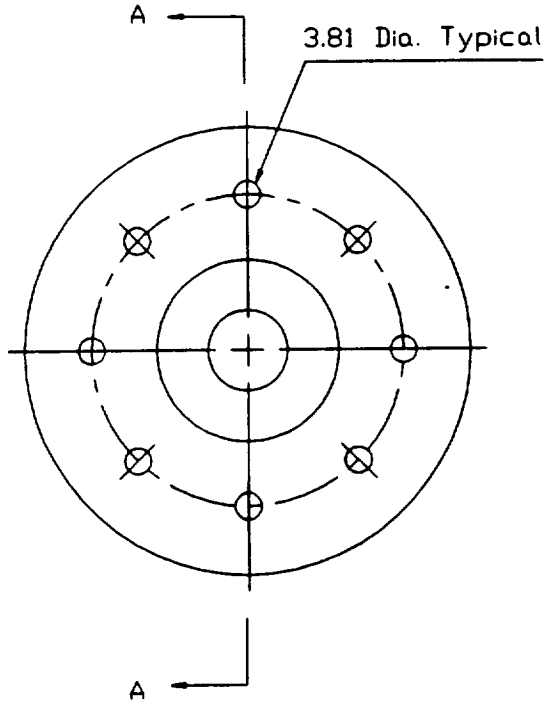

Figure A-8. Left Housing - Back Cover

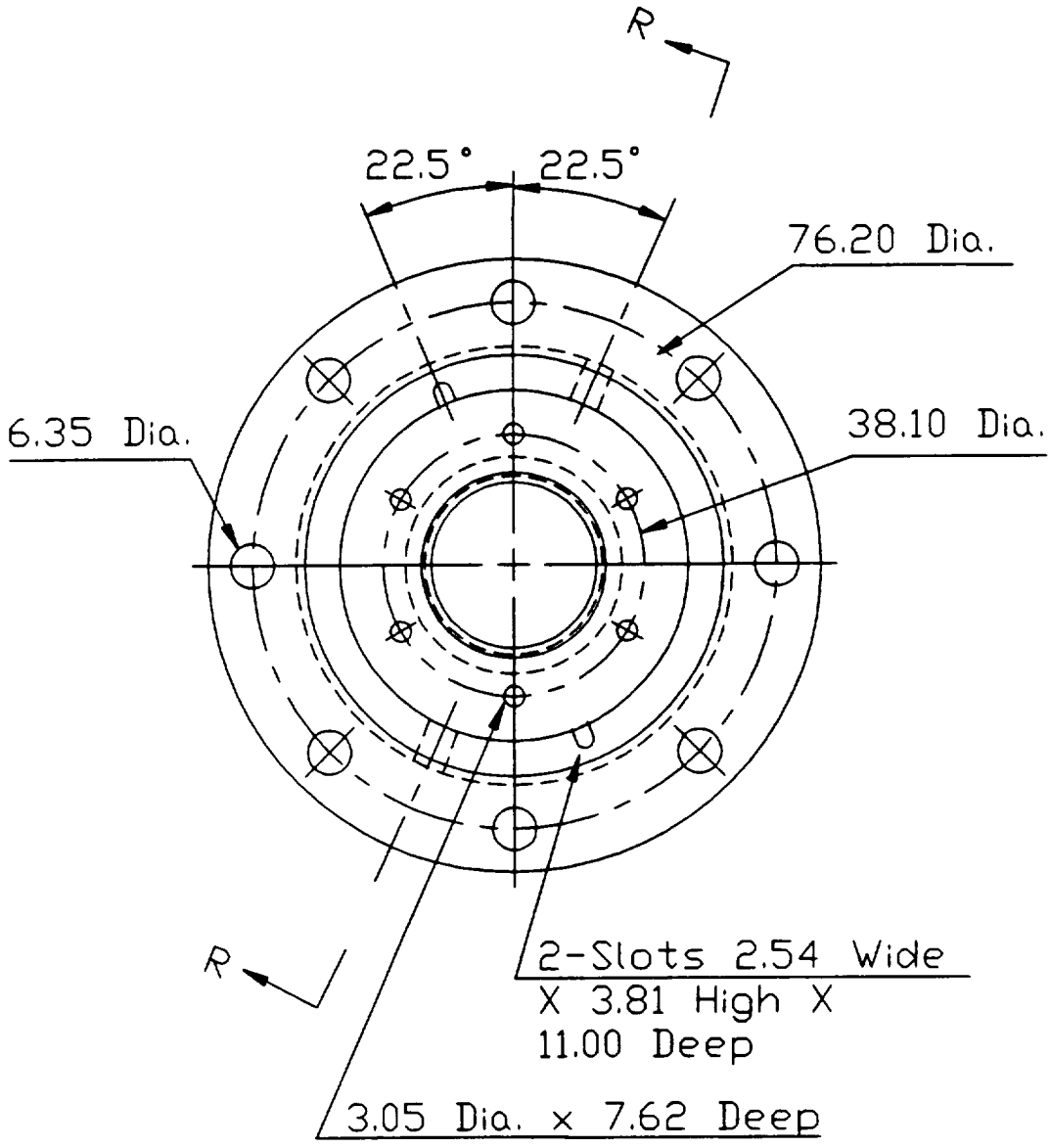

Figure A-9. Right Housing - Front View

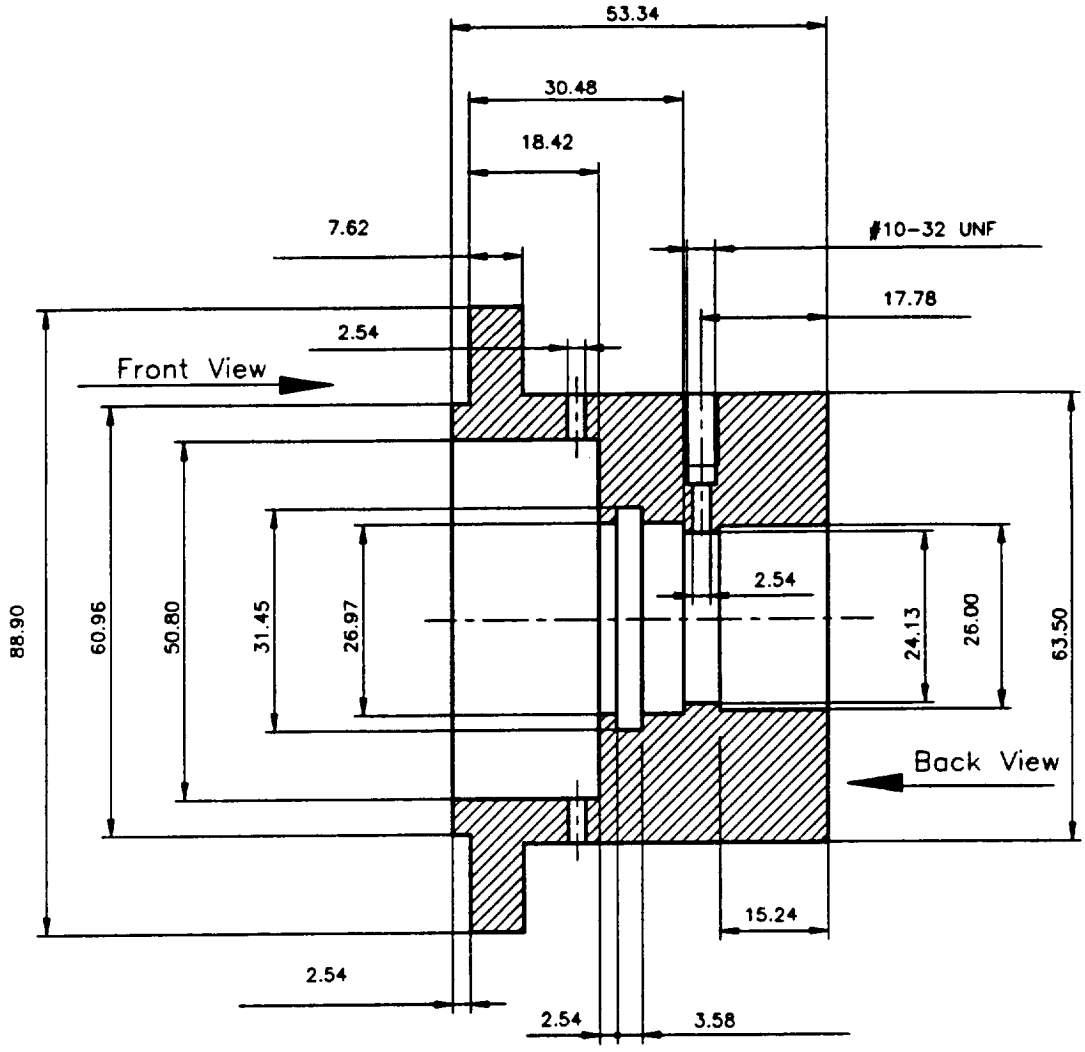

Figure A-10. Right Housing - Cross Section

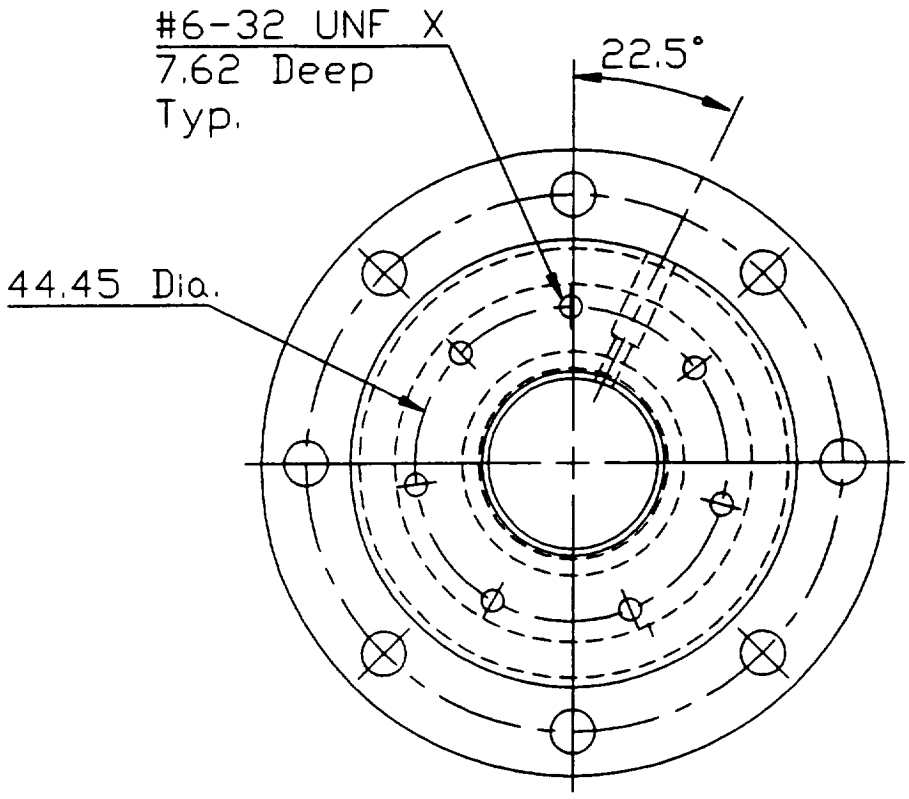

Figure A-11. Right Housing - Back View

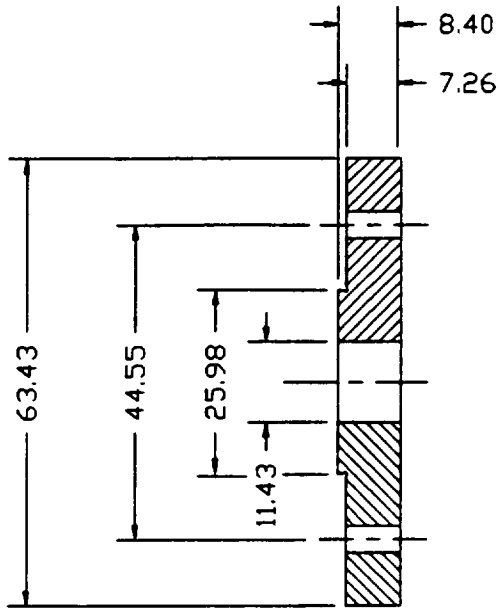

Section A-A

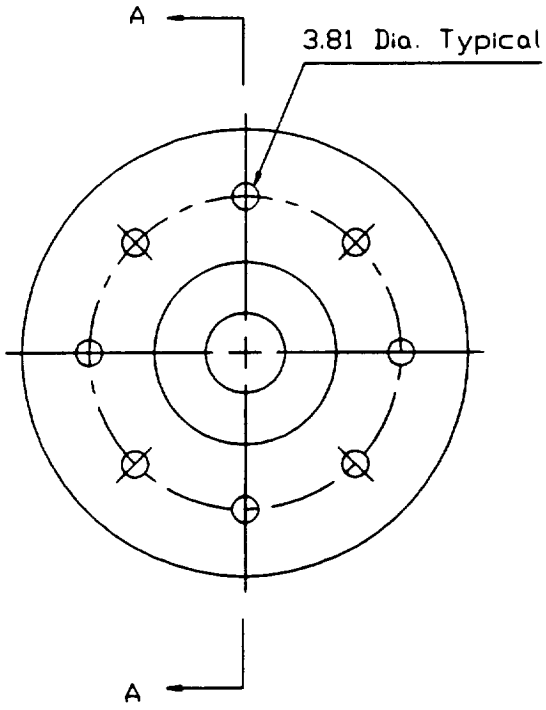

Figure A-12. Right Housing - Back Cover

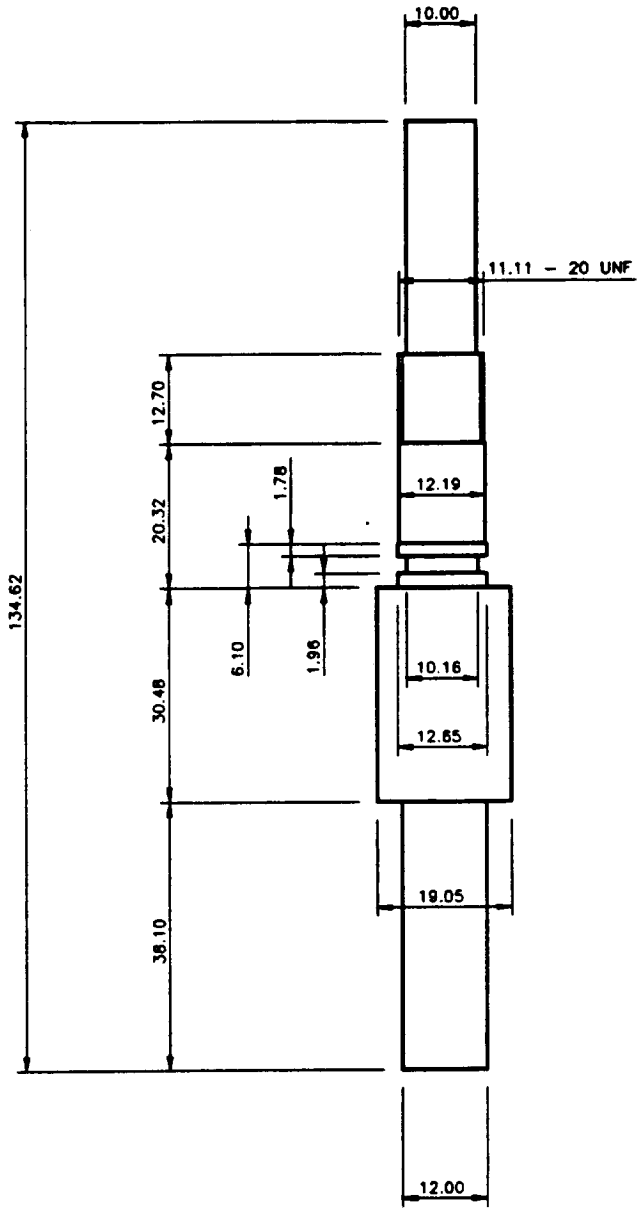

Figure A-13. Shaft

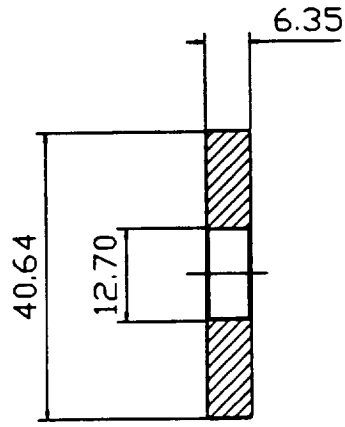

Section A–A

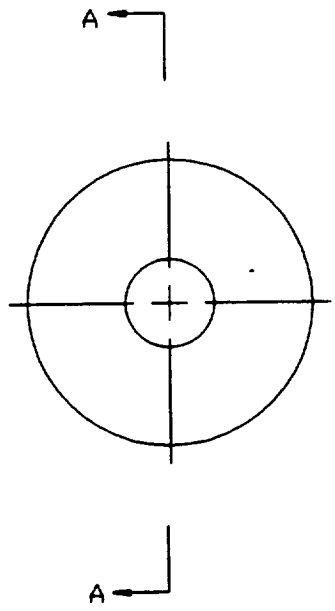

Figure A-14. Rotor

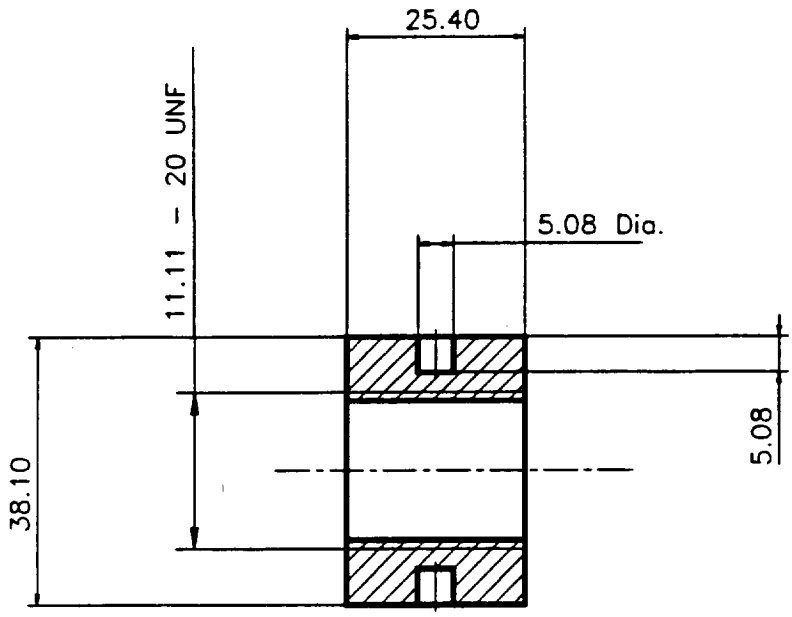

Nut

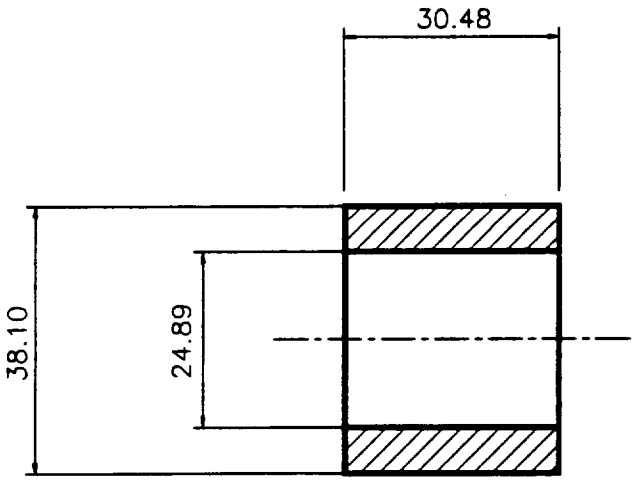

Sleeve

Figure A-15. Nut and Sleeve for Shaft

APPENDIX B

MATERIAL PROPERTIES

The following tables present the material properties for the seal faces, piezoelectric actuator, and holder that were used in the finite element analyses. The materials used for the seal faces were carbon for the nonrotating face and tungsten carbide for the rotating face. The piezoelectric actuator was PZT-5H lead zirconate titanate, and the holder was made from a machinable ceramic, boron nitride. A detailed description of the material coefficients for the piezoelectric actuator is presented elsewhere [Wolff, 1991].

Table 1. Material Properties of Seal Faces and Holder

Property	Carbon	Tungsten Carbide	Boron Nitride
Elastic Modulus (GPa)	2.4	63.0	E_r 73.5 E_θ 73.5 E_z 46.9
Poisson's Ratio	0.25	0.20	0.20
Coeff. of Thermal Expansion (10^{-6}/°C)	4.9	5.1	α_r 0.45 α_θ 0.45 α_z 7.20
Thermal Conductivity (W/m°C)	9.0	80.0	k_r 33.91 k_θ 33.91 k_z 30.15
Density (kg/m^3)	1830	14,700	1903

Table 2. Elastic and Electrical Material Properties for PZT-5H	
Material Property	Value
e_{31}	-6.62 N/Vm
e_{33}	23.24 N/Vm
e_{15}	17.03 N/Vm
c_{11}	127.2 GPa
c_{33}	117.4 GPa
c_{12}	80.2 GPa
c_{13}	84.7 GPa
c_{44}	23.0 GPa
c_{66}	23.5 GPa
ε_{11}^{r}	1.50×10^{-8} f/m
ε_{11}^{i}	-3.01×10^{-10} f/m
ε_{22}^{r}	1.50×10^{-8} f/m
ε_{22}^{i}	-3.01×10^{-10} f/m
ε_{33}^{r}	1.30×10^{-8} f/m
ε_{33}^{i}	-2.60×10^{-10} f/m

Table 3. Thermal Expansion Coefficients of PZT-5H		
Temperature (°C)	α_r, α_θ (10^{-6}/°C)	α_z (10^{-6}/°C)
0	1.0	4.0
50	1.4	4.0
100	2.0	3.0
150	2.7	1.0
200	3.3	-1.6
250	3.9	-4.2

APPENDIX C

MOTOR CONTROLLER

Appendix C presents the detailed drawing of the motor controller that was used to control the speed of the motor that drove the test rig. Also included is a list of the motor controller components.

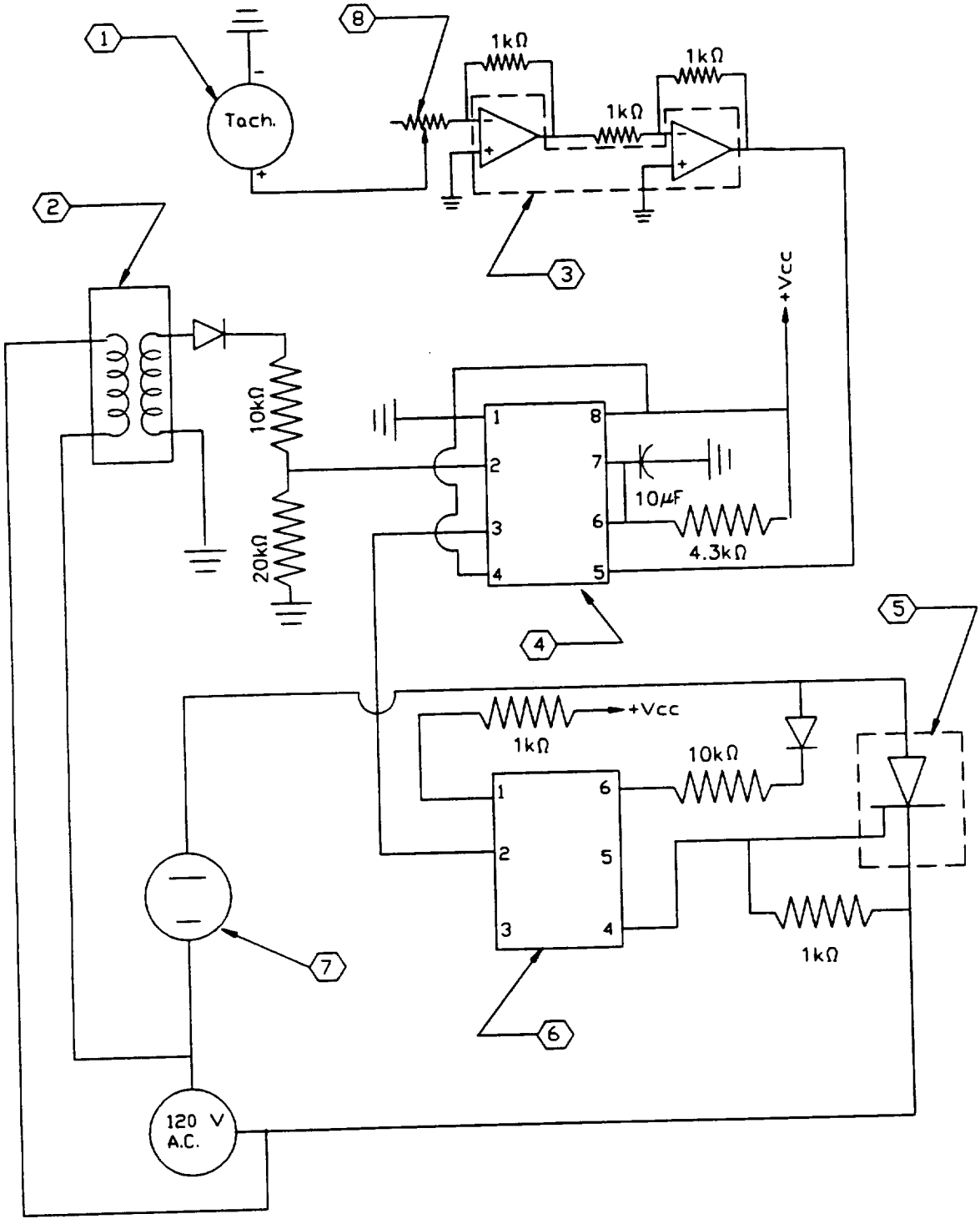

Figure C-1. Motor Controller

Parts List for Motor Controller

(1) 1.5 - 4.5 Archer D.C. Motor (Radio Shack Part No. 273-237).

(2) Transformer, primary 120 V at 60 HZ, secondary 12 V at 150 milliamps.

(3) Dual op-amp (Radio Shack Part No. 276-038). Powered with 2 - 9 V batteries.

(4) 555 Timer (Radio Shack Part No. 276-1723).

(5) Silicon controlled rectifier (SCR), 25 amp, 600 V peak.

(6) Triac output optocoupler (Radio Shack Part No. 276-134).

(7) Electrical connection for motor - standard outlet.

(8) Speed controller - 0-10 kΩ potentiometer.

5 - 1 kΩ, 1/4 W resistors.

2 - 10 kΩ, 1/4 W resistors.

1 - 20 kΩ, 1/4 W resistor.

1 - 4.3 kΩ, 1/4 W resistor.

1 - 10 μF capacitor.

2 - diodes.

Vcc is +9 V.

BIBLIOGRAPHY

1. Alik, N. and Hughes, J.R., "Finite Element for Piezoelectric Vibration," International Journal of Numerical Methods for Engineering, No. 2, pp. 151-157, 1970.

2. Bathe, K. J., Finite Element Procedures in Engineering Analysis, Prentice-Hall, Inc., Englewood Cliffs, N.J., 1982.

3. Budynas, R.G., Advanced Strength and Applied Stress Analysis, McGraw-Hill, New York, New York, 1977.

4. Cleaver, T.N., "Materials of Construction - Chapter 2", in Mechanical Seal Practice for Improved Performance, Editor Summer-Smith, J.D., Mechanical Engineering Publications Ltd. for The Institution of Mechanical Engineers, London, England, 1988.

5. Cook, R. D., Concepts and Applications of Finite Element Analysis, 2nd Ed., John Wiley and Sons, New York, New York, 1981.

6. DeSalvo, G.J. and Gorman, R.W., ANSYS - Engineering Analysis System - User's Manual, Houston, Pa., 1989.

7. Doust, T.G. and Parmar, A., "An Experimental and Theoretical Study of Pressure and Thermal Distortions in a Mechanical Seal," ASLE Transactions, 7ol. 29, 2, pp. 151-159, 1985.

8. Etsion, I., Feasibility Study of a Controlled Mechanical Seal," STLE Preprint No. 90-TC-2D-1, 1990.

9. Gazley, Jr., C., "Heat-Transfer Characteristics of the Rotational and Axial Flow Between Concentric Cylinders," Transactions ASME, Vol. 80, pt. 1, 1958, pp. 79-90.

10. Heilala, A.J. and Kangasneimi, A., "Adjustment and Control of a Mechanical Seal Against Dry Running and Severe Wear", Proc. BHRA 11th International Conference on Fluid Sealing, Cannes, France, April 8-10, Paper H-2, 1987.

11. Hughes, W.F., Basu, P., Beatty, P.A., Beeler, R.M. and Lau, S., "Dynamics of Face and Annular Seals with Two-Phase Flow," NASA Contractor Report 4256, Prepared under Lewis Research Center Grant NAG3-166, 1989.

12. Lebeck, A. O., Principles and Design of Mechanical Face Seals, John Wiley and Sons, Inc., New York, N.Y., 1991.

13. Mayer, E., Mechanical Seals, 3rd Ed., Newnes-Butterworth, London, England, 1977.

14. Metcalfe, R., "A Fluid Mechanical Analysis of Axisymmetric Face Seals on the Basis of Constant Viscosity Laminar Flow," Report AECL-4073, Chalk River, Ontario, Atomic Energy of Canada Limited, December, 1971.

15. Metcalfe, R., "End-Face Seal Deflection Effects - The Problems of Two-Component Stationary or Rotating Assemblies," ASLE Transactions, Vol. 23, 4, pp. 393-400, 1979.

16. Metcalfe, R., "Effects of Pressure and Temperature Changes on End-Face Seal Performance," ASLE Preprint No. 81-LC-1A-2, 1981.

17. Nau, B. S., "Hydrodynamic Lubrication in Face Seals," Proceedings 3rd International Conference on Fluid Sealing, Paper E5, BHRA Fluid Engineering, Cranfield, 1967.

18. Paul, F. W. and Burrowbridge, D., The Prevention of Electrical Breakdown in Spacecraft, NASA SP-208, 1969.

19. Phillips, L. and Harbor, R. D., Feedback Control Systems, Prentice Hall, Inc., Englewood Cliffs, N.J., 1988.

20. Salant, R.F., Miller, A.L., Kay, P.L., Kozlowski, J., Key, W.E. and Algrain, M.L., "Development of an Electronically Controlled Mechanical Seal," Proceedings 11th International Conference on Fluid Sealing, Paper H3, BHRA Fluid Engineering, Cranfield, 1987.

21. Salant, R.F. and Key, W.E., "Development of an Analytical Model for use in Mechanical Seal Design," Proceedings 10th International Conference on Fluid Sealing, Paper G3, BHRA Fluid Engineering, Cranfield, 1984.

22. Salant, R.F., Giles, O. and Key, W.E., "Design of Controllable Mechanical Seals," Tribological Design of Machine Elements, Elsevier Science Publishers B.V., Amsterdam, 1989.

23. Sobin, A.J. and Bissell, W.R., Turbopump Systems for Liquid Rocket Engines, NASA SP-8107, 1974.

24. Vernitron Piezoelectric Division, "Piezoelectric Technology Data for Designers," Bedford, Ohio.

25. Wolff, P. J., "Development of an Actively Controlled Mechanical Seal," Georgia Institute of Technology, Atlanta, Ga., Master's Thesis, 1991.